Electronic, Thermoelectric and Vibrational Properties of Silicon Nanowires and Copper Chalcogenides

A Thesis
Presented to
The Academic Faculty

by

Keenan Zhuo

In Partial Fulfillment
of the Requirements for the Degree
Doctor of Philosophy
School of Physics

Georgia Institute of Technology
May 2015

Electronic, Thermoelectric and Vibrational Properties of Silicon Nanowires and Copper Chalcogenides

Approved by:

Dr. Mei-Yin Chou, Advisor
School of Physics
Georgia Institute of Technology

Dr. Zhigang Jiang
School of Physics
Georgia Institute of Technology

Dr. Andrew Zangwill
School of Physics
Georgia Institute of Technology

Dr. Xiao-Qian Wang
Department of Physics
Clark Atlanta University

Dr. Uzi Landman
School of Physics
Georgia Institute of Technology

Date Approved: March 25, 2015

[13] *Happy is the man that findeth wisdom, and the man that getteth understanding.* [14] *For the merchandise of it is better than the merchandise of silver, and the gain therof than fine gold.*
- Proverbs 3:13-14, KJV

HOW ARE YOU GENTLEMEN!!
ALL YOUR BASE ARE BELONG TO US.
- Zero Wing

ACKNOWLEDGEMENTS

First and foremost, I wish to thank my advisor Dr. Mei-Yin Chou for sharing her knowledge, wisdom and guidance which have been truly inspirational and instrumental in the direction and completion of this work. Throughout, I have also come to appreciate her exceptional humility, patience and willingness to let me pursue my own ideas. Furthermore, I am grateful for the arrangements she made for me to spend a total of six semesters at Academia Sinica, Taiwan which has been a major highlight and particularly enjoyable part of my graduate school life.

Along the way, I have received much help from many others. Dr. Pei Lin, Dr. Salvadore Barraza-Lopez, Dr. Wen-Ying Ruan, Dr. Lede Xian and Dr. Feng Zhang were the original members of the group at Georgia Tech who were around to welcome me when I first joined. They introduced me to the actual rigours and fundamentals of performing materials research. I appreciate their guidance, encouragement and approachability in those early years of my graduate career. I also thank the people who have joined our research group over the years for their help and friendship. These include Dr. Yongmao Cai, Yijun Chen, Dr. Chih-Piao Chuu, Po-Tung Fang, Dr. Tao He, Justin Hou, Dr. Yang-Hao Chan, Dr. Sheng-Fang Lin and Kuang-Hong Liu from Academia Sinica as well as Chih-Ruei Pan and Jing Wang from Georgia Tech.

My collaborators contributed a great deal of input and critical ideas towards this work for which I am also very thankful. At Academia Sinica, I thank Dr. Cheng-Rong Hsing and Dr. Ching-Ming Wei for proposing the random structure search method, which we used in our study of disordered copper sulphide and copper selenide, as well as helping us to perform some of the structural optimizations. At Georgia Tech, I am also grateful to Dr. Uzi Landman and Dr. Jianping Gao for sharing their expert and extensive knowledge of molecular dynamics simulations which constitute a large part of this work.

This work heavily involves computer simulations on high-performance computing clusters. Most of the computational resources were provided by Academia Sinica and I am indebted to Dr. Jen-Chang Chen and Ching-Tao Lee for doing a great job at ensuring the smooth operation of those clusters as well as being exceptionally prompt to assist me with any software and hardware related problems.

I am grateful for the many friendships I have been able to share over the years with people from both Georgia Tech and Academia Sinica. At Georgia Tech, I thank Xunchi Chen, Yen-Jun Chen, Jacob Daughtree, Scott Douglas, Dr. Cesar Flores, Dr. Zelei Guo, Wenchao Jiang, Dr. Adam Kamor, Doga Murat Kurckuoglo, Samson Lai, Alex Lesov, Yuntao Li, Dr. James Palmer, Fei-Fei Qian, Dipanjan Sengupta, Balachandra Suri, Meredith Swegan, Bradford Taylor, Anshuman Vinit, Feng Wang, and Dr. Tsz-Chun Wong. At Academia Sinica, I thank Dr. Yun-Wen Chen, Dr. Yaojun Du and Dr. Lian-Ming Lyu. Annie Lin in particular has been a great help in organising my accomodation and handling various local matters during my visits to Taiwan.

I would also like to extend my thanks to Nong Shim Ltd. for manufacturing the many, many packets of delicious instant noodles which have kept me fairly well nourished at an affordable rate throughout graduate school. This is something which Georgia Tech Dining Services were never able to accomplish.

Finally, I thank my parents Susam Tam and Kok Swee Toh who have always encouraged me to become a doctor, even though they specifically meant the type of doctor who cures sick people.

TABLE OF CONTENTS

LIST OF TABLES

LIST OF FIGURES

SUMMARY

Dwindling fossil fuel reserves and severe pollution necessitate the innovation of new technologies to harvest energy from clean and renewable sources. This effort depends crucially on the development of advanced new materials. In this work, we perform first-principles simulations based on Density Functional Theory (DFT) to evaluate the properties of Copper Sulfide (Cu_2S) and Copper Selenide (Cu_2Se) as well as Silicon Nanowires (SiNWs) which make them of interest in the areas of thermoelectricity and photovoltaics.

SiNW solar cells are a vast improvement over conventional bulk Silicon solar cells in terms of efficiency and cost. Still, challenges remain to enhance SiNW stability and tune their electronic and light absorption properties through different surface passivations. We utilize first-principles calculations on fluorine, methyl and hydrogen passivated [110] and [111] SiNWs to explain how surface passivations fundamentally alter the electronic structure through quantum confinement and strain. Moreover, we demonstrate how SiNWs may be modeled as circular quantum wells and elaborate on why [110] SiNWs are more strongly affected by their surface passivation than [111] SiNWs.

Thermoelectric materials open new avenues for waste heat recovery by converting temperature differences into potential differences. Cu_2S and Cu_2Se have recently been demonstrated to have remarkably high thermoelectric efficiencies by virtue of a unique solid-liquid hybrid phase which disrupts thermal transport while maintaining good electrical characteristics. Using first-principles molecular dynamics, we report very high Cu diffusion rates and obtain phonon power spectra in Cu_2S and Cu_2Se, which we use to explain their low thermal conductivities. Furthermore, we combine first-principles electronic structure calculations with Boltzmann Transport Theory to evaluate the Seebeck coefficient and obtain the hole concentration corresponding to the optimum power factor in p-type Cu_2S and Cu_2Se.

CHAPTER I

INTRODUCTION

The world's heavy reliance on fossil fuels for its energy needs has led to myriad environmental and social problems. For example, fossil fuel combustion releases various toxic fumes including oxides of carbon, nitrogen and sulphur which damage human health and also lead to environmental degradation and unfavourable climate change via smog, acid rain and the greenhouse effect. The limited supply of fossil fuels also conveys immense political leverage upon certain unsavoury regimes which just so happen to be the major suppliers. Reducing the world's unhealthy dependence on fossil fuels demands the development of various clean energy technologies. These include high capacity lithium ion battery for energy storage, efficient photovoltaic cells for harvesting plentiful solar energy and more recently, utilizing the thermoelectric effect to recycle waste heat. Success in developing each of these highly advanced technologies hinges critically upon the discovery or engineering of new materials which have the right combination of properties to drive performance. Silicon nanowires and copper chalcogenides are examples of such advanced energy materials which each have applications in a surprisingly diverse array of clean energy technologies.

1.1 Silicon Nanowires

The utility of silicon nanowires (SiNWs) as a class of advanced energy materials stems primarily from their inherent one-dimensional (1D) quantum confinement and boundary scattering mechanisms which are responsible for making their electronic and thermal properties almost completely different from the bulk.[1, 2, 3] Moreover, the latest advancements in SiNW growth technology have also enabled large and highly ordered arrays of SiNWs to be grown cost effectively.[4, 5, 6]

Arguably the most well known use of SiNWs is in the creation of photovoltaic arrays. The 1D geometry of SiNWs allows for the creation of radial p-n junctions, where the core is

p doped and the shell is n doped or vice versa. This design ingeniously orthogonalizes the light absorption and carrier collection directions. The long length of each SiNW optimizes the surface area available for light absorption while the short radius provides little room for excited electrons and holes to recombine, thereby enhancing carrier collection.[7] Already, SiNW photovoltaic arrays utilizing the radial p-n junction geometry have demonstrated very promising results.[8, 9, 10]. Kelzenberg *et al.* in particular proved that SiNW photovoltaic arrays could absorb up to 85% of day-integrated sunlight with a peak external quantum efficiency of 89%. This was most impressively achieved using only a hundredth of the amount of material in a traditional wafer based silicon photovoltaic cell. The main draw of SiNW photovoltaic cells is not so much that they will one day exceed traditional limits on efficiency but more so that they can radically lower the cost of silicon photovoltaic technology as they require drastically less raw material for construction.[10]

SiNWs are also of great interest as thermoelectric materials. Thermoelectric materials effectively convert temperature differences into voltage differences. This process allows us recover waste heat as useful electrical energy. Hochbaum *et al.* [11] and Boukai *et al.* [12] measured the experimental thermoelectric efficiency of silicon nanowires to be about a hundred times greater than in the bulk. Using molecular dynamics simulations, Donadio and Galli concluded that this was due to a huge reduction in thermal conductivity which in amorphous SiNWs, was typically a hundred times lower than the thermal conductivity in bulk silicon ($\sim 150 \mathrm{Wm}^{-1}\mathrm{K}^{-1}$).[13] Donadio and Galli further showed that this low thermal conductivity even remains consistent over a wide range of temperatures from 200K to 600K.[14] The primary mechanism behind the exceptionally low thermal conductivity in SiNWs is the enhanced scattering of phonons at the SiNW surfaces.[15]. While SiNWs may not be as efficient as the current state-of-the-art thermoelectric materials, cheap and ubiquitous silicon, coupled with low material requirements, non-toxicity and manufacturing ease nonetheless provide SiNWs with a competitive edge.

Raw SiNWs have highly unstable dangling bonds on their surfaces which lead to low ambient stability and undesirable surface states within the band gap. Therefore, it is common practice to have such bonds passivated prior to further use or study. This is

usually achieved via hydrogen (H) surface passivation. Yet, even H terminated silicon nanowire surfaces are susceptible to surface oxidation and are not stable when exposed to air for more than a few days.[16] As such, different chemical surface passivations have been studied for the purpose of improving the ambient stability of SiNWs. Most notably, methyl (CH_3) passivated SiNWs have been demonstrated to be far more stable than H-passivated without experiencing severe degradation of their critical electrical characteristics.[16, 17, 18] In fact, experiments by Haick *et al.*. have indicated that CH_3-passivated SiNWs were even able to maintain superior transport characteristics over H-passivated SiNWs for more than 40 days.[17] The enhanced stability of CH_3-passivated SiNWs is attributable to the strong Si-C bonds and high surface coverage (over 85%) of CH_3.[16, 19] Moreover, Shen *et al.*. demonstrated that CH_3-passivated SiNW arrays were even stable enough against oxidation and corrosion when in contact with electrolytes, thereby making SiNW arrays viable as photoelectrochemical cells.[18]

The process of passivating SiNW surfaces typically involves multiple steps. The intermediate steps often involve passivation with some halogen or hydroxyl (OH) group, all of which we note are highly electronegative.[16, 17, 18, 19, 20, 21] For example, passivating a SiNW with CH_3 first involves passivating it with H which are subsequently replaced by chlorine (Cl) and finally the Cl are substituted by the CH_3 groups.[18] Naturally, steric effects and other imperfections prevent the complete substitution of intermediate passivants. Haick *et al.* found that no more than 85% of their SiNW surfaces could be covered by the desired CH_3 groups which is one of the smaller types of surface passivants.[16]

The presence of organic or electronegative atoms or groups on an SiNW surface can be expected to change the electronic structure of the SiNWs. This will affect band gaps and carrier group velocities which can alter performance in applications dependent on optical absorption and electrical conductivity among other properties. The effects of surface passivation on SiNWs should not be viewed in a negative light though. In fact, surface passivation may be considered as a form of electronic band engineering. This affords us the ability to tune the electronic and optical properties of SiNWs which is especially important in the area photovoltaics and even sensor development. It is therefore imperative that we

gain a full understanding of how various surface passivants affect the electronic structure of SiNWs. As SiNWs have various possible growth orientations, it is also interesting to analyze how strongly surface passivants affect the electronic structures of SiNWs grown in different directions.

1.2 Copper Chalcogenides

Like SiNWs, the copper chalcogenides[1] namely copper sulfide (Cu_2S) and copper selenide (Cu_2Se) also have with a wide variety of energy applications. Their near ideal band gaps of around 1.2eV make them excellent choices as photovoltaic materials. In this area, they are known to interface especially well with the cadmium (Cd) chalcogenides CdS and CdSe to form high efficiency core-shell nanowire photovoltaic arrays.[22, 23, 24, 25, 26, 27, 28, 29] Furthermore, they are prime candidates as cathode materials in rechargeable ion batteries, where they have demonstrated better performance than the more well-known but expensive platinum.[28, 30, 31, 32, 33, 34] However, it is in the field of thermoelectricity that the properties of Cu_2S and Cu_2Se really shine.[35, 36, 37, 38] Thermoelectric efficiency is most often measured by the dimensionless thermoelectric figure of merit (ZT).

$$ZT = \frac{S^2 \sigma T}{\kappa} \tag{1}$$

measures how high the thermoelectric efficiency is for a particular material. In the formula for ZT, S is the Seebeck coefficient, σ is the electrical conductivity, T is the thermodynamic temperature and $\kappa = \kappa_e + \kappa_l$ is the sum of the thermal conductivities due to electrons (κ_e) and phonons (κ_l) respectively. The quantity $S^2\sigma$, otherwise known as the power factor, is a purely electronic contribution. In general, a good thermoelectric material requires high electrical conductivity and low thermal conductivity. So far, ZT values for Cu_2S and Cu_2Se have been measured to be as high as 1.7 and 1.5 respectively, at temperatures of around 1000K.[36, 38] The high ZT values of Cu_2S and Cu_2Se puts them on par with some of the best known thermoelectric materials to date such as PbTe [39] and SiGe [40, 41, 42] alloys.

[1] Chalcogenides are compounds formed from a group 16 element (oxygen (O), sulphur (S), selenium (Se), tellurium (Te) and polonium (Po)) and a more electropositive element. The group 16 elements are collectively known as chalcogens.

Moreover, many of their thermoelectric competitors tend to contain rare, expensive or toxic heavy elements such as Pb, Co and Te, while Cu_2S and Cu_2Se do not suffer such severe disadvantages. Cu_2S in particular is a highly abundant and inexpensive copper ore that is completely non-toxic.

As in the case of the SiNWs, what makes Cu_2S and Cu_2Se such outstanding thermoelectric materials is their unexpectedly low thermal conductivities. He *et al.* [36] and Liu *et al.* [38] found the thermal conductivities of Cu_2S and Cu_2Se to both be under $1 Wm^{-1}K^{-1}$ at temperatures of about 1000K. Both Cu_2S and Cu_2Se owe their exceptionally low thermal conductivities to their unique solid-liquid hybrid nature. At around 1000K, the S (Se) atoms of Cu_2S (Cu_2Se) form a crystalline face centered cubic (FCC) sublattice with the Cu atoms randomly distributed in between. However, the Cu atoms are not frozen into position. Contrariwise, the diffusion rates of the Cu atoms are so high that the Cu atoms may be considered liquid-like.[43] It is precisely this liquid-like nature of Cu that enables them to strongly scatter phonons in order for Cu_2S and Cu_2Se to maintain low thermal conductivities. In regular materials, electron and phonon pathways are typically more strongly coupled to each other, where for example, disrupting thermal conductivity almost always results in similarly reduced electrical conductivity and hence insignificant or no overall gain in ZT. However, the solid-liquid nature of Cu_2S and Cu_2Se is conducive for allowing κ and $S^2\sigma$ to be optimized independently of each other to an extent, such that a high ZT can be achieved.[36, 38]. Materials such as Cu_2S and Cu_2Se which have special properties that result in the decoupling of electron and phonon interactions are jointly referred to as phonon-liquid electron crystals or phonon-glass electron crystals depending on how mobile their constituent atoms are.[36, 38, 44]

Being solid-liquid hybrids, Cu_2S and Cu_2Se are naturally related to class of materials known as superionic conductors. The difference between Cu_2S and Cu_2Se and the superionics is subtle. As we shall see from Bader charge analysis in Chapters 4 and 5, the Cu-S (Cu-Se) bonds in Cu_2S (Cu_2Se) are more covalent in nature and hence we simply refer to Cu_2S and Cu_2Se as solid-liquid hybrids. Superionic conductors themselves are very interesting materials for they allow the relatively fast hopping of ions throughout their rigid crystal

structure. Superionic conductors also qualify as solid state electrolytes and are popularly studied for use in the development of solid state batteries and fuel cells.[45, 46] Well known superionic conductors include the metal halides CuX and AgX (X=Cl, Br and I). In these metal halides, the metal cations exhibit high diffusion rates within a crystalline anion sublattice. The diffusion coefficients of the metal cations in CuX and AgX have been recorded to be over $10^{-5}\text{cm}^2\text{s}^{-1}$ although they are usually only achieved at very high temperatures of 700K.[47, 48, 49, 50, 51] However, Wang was able show, from first-principles molecular dynamics simulations, that the Cu atoms in Cu_2S become liquid-like with diffusion coefficients of about $10^{-6}\text{cm}^2\text{s}^{-1}$ at a much lower 450K.[43] Since melting can be expected to begin on surfaces before occurring in the bulk, this finding suggests the intriguing possibility of observing solid-liquid hybrid behaviour in Cu_2S and Cu_2Se at even lower temperatures than previously recorded.

Due to the disordered liquid behaviour of Cu, the structural properties of Cu_2S and Cu_2Se are still not well understood. Experimental attempts at obtaining their structural details via X-ray diffraction [52, 53, 54, 55] are often inconsistent with each other. Theoretical and computational studies [29, 56, 57] which specifically include Cu disorder have also been few. Developing good structural models for these materials will allow us to learn much more about their electronic and vibrational properties which are important for understanding their thermoelectric properties. In addition, Cu diffusion rates have only been measured at low temperatures experimentally to the best of our knowledge. As high temperature thermoelectric materials designed to operate around 1000K, it is insightful to know how high the Cu diffusion rates can be in Cu_2S and Cu_2Se and how they compare to diffusion in the related superionics. This should furthermore shed light on the lithiation and delithiation mechanism in CuS Li ion batteries where $Cu_{2-x}S$ forms an intermediate phase.[30, 33]

1.3 Thesis Outline

In the next Chapter, we outline the main theoretical and computational methods which we use in this work. These mainly pertain to first-principles density functional theory (DFT), molecular dynamics simulations and Boltzmann transport theory.

Following on in Chapter III, we detail our investigation of the electronic structures of [110] and [111] SiNWs using DFT. Using their H passivated forms as a basis for comparison, we will see how surface passivation with highly electronegative fluorine (F) and the inert but larger CH_3 groups alter the electronic structures of [110] and [111] SiNWs, through basic mechanisms such as quantum confinement and mechanical strain. In addition, we show how the infinite circular potential well can effectively model the electronic charge density states in these H, F and CH_3 passivated [110] and [111] SiNWs.

In Chapter IV, we discuss a first-principles random structure search method to find stable structures of the disordered phases of Cu_2S and Cu_2Se. We then proceed to analyse the electronic structures of these materials based on the structural models developed also from first-principles calculations. Using their electronic band structures, we calculate their corresponding thermoelectric properties, namely their Seebeck coefficients, electrical conductivities and power factors, via Boltzmann transport theory.

Finally, we continue our analyses of the disordered phases of Cu_2S and Cu_2Se in Chapter V by performing first-principles molecular dynamics. These simulations provide atomic trajectory data as output, from which we calculate Cu diffusion coefficients, pair correlation functions and phonon power spectra.

CHAPTER II

THEORETICAL AND COMPUTATIONAL BACKGROUND

In this chapter, we review the theoretical and computational methods employed in this work.

2.1 The Quantum Many-body Problem

The starting point for describing the properties of matter is the Hamiltonian for a system of nuclei and electrons

$$H = -\sum_i \frac{1}{2}\nabla_i^2 - \sum_I \frac{1}{2M_I}\nabla_I^2 + \sum_i \sum_{j>i} \frac{1}{|r_i - r_j|} + \sum_I \sum_{J>I} \frac{Z_I Z_J}{|r_I - r_J|} + \sum_{i,I} \frac{Z_I}{|r_i - R_I|}. \quad (2)$$

In the above equation, we adopt Hartree atomic units where $\hbar = m_e = e = \frac{1}{4\pi\epsilon_0} = 1$. Lower case subscripts label electron quantities while upper case subscripts label nuclear quantities. Z and M denote the proton numbers and masses of the nuclei respectively. The first two terms are the kinetic energies of electrons and nuclei and the last three terms are the electron-electron, proton-proton and electron-proton Coulomb interaction energies.

Considering the fact that electrons are far lighter than the nuclei, the electrons must also be moving that much faster than the nuclei which in effect are very nearly stationary in comparison to electron motion. Therefore, the second term of Equation 2 for the kinetic energy of nuclei is often neglected when considering electronic motion. This is commonly known as the Born-Oppenheimer approximation.

In the picture given by the Born-Oppenheimer approximation, electrons are able to almost instantaneously adapt to any changes in arrangement of nuclei. As such, it is also customary to treat the Coulomb potential of the nuclei as part of the external system. In other words, we define an external potential energy $V_{ext}(\vec{r})$ of the electric field due to all the nuclei and also with other electric fields external to the material system of nuclei and

electrons. All in all, the many-body Hamiltonian simplifies to

$$H = T + V_{int} + V_{ext} + E_{II}, \tag{3}$$

where

$$T = -\sum_{I} \frac{1}{2M_I} \nabla_I^2 \tag{4}$$

$$V_{int} = \sum_{i} \sum_{j>i} \frac{1}{|r_i - r_j|} \tag{5}$$

$$E_{II} = \sum_{I} \sum_{J>I} \frac{Z_I Z_J}{|r_I - r_J|}. \tag{6}$$

In particular, the Coulomb interaction energy between nuclei E_{II} may be viewed simply as a constant contribution to the total energy of the system. Thus, the Hamiltonian in Equation 3 is a fundamental description of the electronic structure of matter.

The normalised many-body wave function Ψ which satisfies the time-independent Schrödinger equation

$$H\Psi(\vec{r}_1, \vec{r}_2, ..., \vec{r}_N) = E\Psi(\vec{r}_1, \vec{r}_2, ..., \vec{r}_N), \tag{7}$$

allows us to determine the various physical properties of a system having N electrons. Here, the $\vec{r}_i$ are the positions of the electrons within the system. The total electron density of the system is then given by

$$\rho(\vec{r}) = N \frac{\int |\Psi(\vec{r}, \vec{r}_2, ..., \vec{r}_N)|^2 d\vec{r}_2 ... d\vec{r}_N}{\int |\Psi(\vec{r}_1, \vec{r}_2, ..., \vec{r}_N)|^2 d\vec{r}_1 d\vec{r}_2 ... d\vec{r}_N}. \tag{8}$$

Unfortunately, solving the many-body Schrödinger equation is an $3N$ coordinate problem which is made intractable largely due to the coupling term V_{int} in the Hamiltonian. Density functional theory (DFT) offers a way out of this predicament.[58]

2.2 Density Functional Theory

The central principle of DFT is that for a system of interacting particles, any of its properties may be expressed as a functional of its ground state electron density. Dealing with electron densities instead of wave functions effectively simplifies a $3N$ coordinate problem to one associated with the usual 3 spatial coordinates. Several versions of density functional theory have been proposed over the years but we focus here on the formulation by Hohenberg and Kohn which is currently the most useful and widely adopted approach.[59]

2.2.1 Hohenberg-Kohn Theorems

The two theorems of Hohenberg and Kohn lay the foundation for modern density functional theory. However, they stop short of providing any guidance for setting up the form of the density functionals.

2.2.1.1 Hohenberg-Kohn Theorem I

Consider a system of electrons with the Hamiltonian again given by Equation 3

$$H = T + V_{int} + V_{ext} + E_{II}. \tag{9}$$

The first Hohenberg-Kohn theorem states that $V_{ext}(\vec{r})$ is completely determined by the ground state electronic density $\rho_0(\vec{r})$, except for a trivial constant. The proof of this theorem is surprisingly simple. For the sake of argument, let us assume that there exists two external potential energies $V'_{ext}(\vec{r})$ and $V''_{ext}(\vec{r})$ which are determined by common ground state density $\rho_0(\vec{r})$. This leads to two separate Hamiltonians H' and H'' with their respective ground state wave functions Ψ' and Ψ'' as well as ground state energies E' and E''. Since Ψ'' is not the ground state of H', we have by definition that

$$\langle \Psi' | H' | \Psi' \rangle < \langle \Psi'' | H' | \Psi'' \rangle \tag{10}$$

$$\langle \Psi' | H' | \Psi' \rangle < \langle \Psi'' | H'' | \Psi'' \rangle + \langle \Psi'' | H' - H'' | \Psi'' \rangle \tag{11}$$

$$E' < E'' + \langle \Psi'' | H' - H'' | \Psi'' \rangle. \tag{12}$$

However, if we repeat the above analysis by beginning with $\langle \Psi'' | H'' | \Psi'' \rangle < \langle \Psi' | H'' | \Psi' \rangle$ instead, we end up with

$$E'' < E' + \langle \Psi' | H'' - H' | \Psi' \rangle. \tag{13}$$

Separately summing up the left and right hand sides of Eqs. 12 and 13 leads to the obviously contradictory statement

$$E' + E'' < E'' + E'. \tag{14}$$

Therefore, we are forced to conclude that $\rho_0(\vec{r})$ uniquely determines $V_{ext}(\vec{r})$. From this it follows that H and consequently E are also uniquely determined by $\rho_0(\vec{r})$.[58]

2.2.1.2 Hohenberg-Kohn Theorem II

The second Hohenberg-Kohn theorem states that the total energy of a system may always be expressed as a functional of electronic density $\rho(\vec{r})$ for any external potential $V_{ext}(\vec{r})$. The ground state energy of the system is then determined by minimising this energy functional with respect to $\rho(\vec{r})$. Furthermore, the $\rho(\vec{r})$ which minimises the energy functional corresponds exactly to the ground state electronic density $\rho_0(\vec{r})$.

From the first Hohenberg-Kohn theorem, we know that various properties of a system such as the total energy E_{HK}, kinetic energy T and internal energy U are uniquely determined by $\rho(\vec{r})$, we have

$$E_{HK}[\rho(\vec{r})] = T[\rho(\vec{r})] + V_{int}[(\rho(\vec{r})] + \int d\vec{r} V_{ext}(\vec{r})\rho(\vec{r}) + E_{II}. \tag{15}$$

Suppose we have a Hamiltonian H with ground state wave function Ψ. The ground state energy E_0 will always be less than the energy calculated using any other wave function Ψ'.

$$E_0 = \langle \Psi | H | \Psi \rangle < \langle \Psi' | H | \Psi' \rangle. \tag{16}$$

Therefore, it must be the case that by minimising the functional $E_{HK}(\rho(\vec{r}))$ with respect to $\rho(\vec{r})$, the ground state energy E_0 will be obtained along with the corresponding ground state electronic density $\rho_0(\vec{r})$.[58]

2.2.2 The Kohn-Sham *Ansatz*

In the modern formulation of density functional theory, practical application of the Hohenberg-Kohn theorems is made possible through the Kohn-Sham *ansatz*.[58, 60] In the Kohn-Sham *ansatz*, we first consider an auxiliary independent electron system. The Hamiltonian for this auxiliary system with N non-interacting electrons

$$H_{aux} = \sum_i h_i^{aux} = \sum_i \left(-\frac{1}{2}\nabla_i^2 + V_{eff}(\vec{r}_i) \right) \tag{17}$$

consists of the usual kinetic energy operator and an effective local potential operator. The eigenvalues ϵ_i which satisfy

$$h_i^{aux}\phi_i(\vec{r}) = \epsilon_i \phi_i(\vec{r}), \tag{18}$$

while important in the mathematical formulation of the theory, have no physical meaning of their own. The eigenfunctions $\phi_i(\vec{r})$ of h_i^{aux} are referred to as the Kohn-Sham orbitals. The electron density for this auxiliary system is given by the sum of the squares of these individual electron Kohn-Sham orbitals

$$\rho(\vec{r}) = \sum_i |\phi_i(\vec{r})|^2. \tag{19}$$

$\rho(\vec{r})$ is also assumed to be identical to electron density of original interacting system. The wavefunction $\Phi(\vec{r}1, \vec{r}2, ..., \vec{r}_N)$ of the entire system of non-interacting electrons is constructed using a Slater determinant of the individual Kohn-Sham orbitals $\phi_i(\vec{r}_i)$

$$\Phi(\vec{r}_1, \vec{r}_2, ...\vec{r}_N) = \frac{1}{\sqrt{N!}} \begin{vmatrix} \phi_1(\vec{r}_1) & \phi_2(\vec{r}_1) & \dots & \phi_N(\vec{r}_1) \\ \phi_1(\vec{r}_2) & \phi_2(\vec{r}_2) & \dots & \phi_N(\vec{r}_2) \\ \vdots & \vdots & \ddots & \vdots \\ \phi_1(\vec{r}_N) & \phi_2(\vec{r}_N) & \dots & \phi_N(\vec{r}_N) \end{vmatrix}. \tag{20}$$

This Slater determinant construction guarantees that exchange anti-symmetry is satisfied.

The form of $V_{eff}(\vec{r})$ in H_{aux}, unmentioned as yet, becomes apparent by considering the total energy of the system

$$E[\rho(\vec{r})] = T_{KS}[\rho(\vec{r})] + \int d\vec{r} V_{ext}\rho(\vec{r}) + \frac{1}{2}\int d\vec{r}d\vec{r}' \frac{\rho(\vec{r})\rho(\vec{r}')}{|\vec{r} - \vec{r}'|} + E_{xc}[\rho(\vec{r})]. \tag{21}$$

In the above equation for $E[\rho(\vec{r})]$, the first term $T_{KS}[\rho(\vec{r})]$ is the kinetic energy of the non-interacting electrons

$$T_{KS}[\rho(\vec{r})] = -\frac{1}{2}\sum_i^N \left\langle \phi_i(\vec{r}) \left| \nabla^2 \right| \phi_i(\vec{r}) \right\rangle = \frac{1}{2}\sum_i^N \left|\nabla\phi_i(\vec{r})\right|^2. \tag{22}$$

The second and third term of $E[\rho(\vec{r})]$ are the external potential and Hartree energies $E_{Hartree}[\rho(\vec{r})]$ respectively. $E_{xc}[\rho(\vec{r})]$ represents the electron exchange and correlation energies which are missing from the auxiliary independent electron system, together with the error between the actual kinetic energy and the Kohn-Sham kinetic energy T_{KS}. Minimising $E[\rho(\vec{r})]$ with respect to the density $\rho(\vec{r})$

$$\frac{\delta E[\rho(\vec{r})]}{\delta\rho(\vec{r})} = \frac{\delta T_{KS}[\rho(\vec{r})]}{\delta\rho(\vec{r})} + V_{ext} + \int d\vec{r}' \frac{\rho(\vec{r})}{|\vec{r} - \vec{r}'|} + \frac{\delta E_{xc}}{\delta\rho(\vec{r})} = 0 \tag{23}$$

leads to the ground state energy E_0 and electron density $\rho_0(\vec{r})$ of the original interacting system. Furthermore, it is now clear that the effective potential

$$V_{eff}(\vec{r}) = V_{ext} + \int d\vec{r}' \frac{\rho(\vec{r})}{|\vec{r} - \vec{r}'|} + \frac{\delta E_{xc}}{\delta \rho(\vec{r})} \quad (24)$$

$$= V_{ext} + V_{Hartree}[\rho(\vec{r})] + V_{xc}[\rho(\vec{r})] \quad (25)$$

is simply the sum of external, Hartree and exchange-correlation potentials respectively.[58]

2.2.2.1 Iterative Solution to the Kohn-Sham Equations

As can be seen from the description of the Kohn-Sham equations

$$\left\{ -\frac{1}{2}\nabla^2 + V_{eff}(\vec{r}) \right\} \phi_i(\vec{r}) = \epsilon_i \phi_i(\vec{r}) \quad (26)$$

in the previous section, we may solve the Kohn-Sham equations using an iterative self-consistent scheme as follows. We begin with a trial electron density as input. Using this trial electron density, we formulate V_{eff} and hence the auxiliary Hamiltonian. From here, we solve the Kohn-Sham equations for $\phi_i(\vec{r})$ which yields a new electron density. If this new density is not self-consistent with the original input, then the process is repeated using the new electron density as the input. This process is similarly implemented in the Vienna Ab-initio Simulation Package (VASP) and various other first-principles simulation packages. We show in Fig. 1 a summary of this computational workflow.[58, 60]

2.2.3 Exchange-Correlation Functionals

The exact form of the exchange-correlation functional $E_{xc}[\rho(\vec{r})]$ is unknown but there has been much success in simply approximating it as a local or nearly local functional of the electron density.

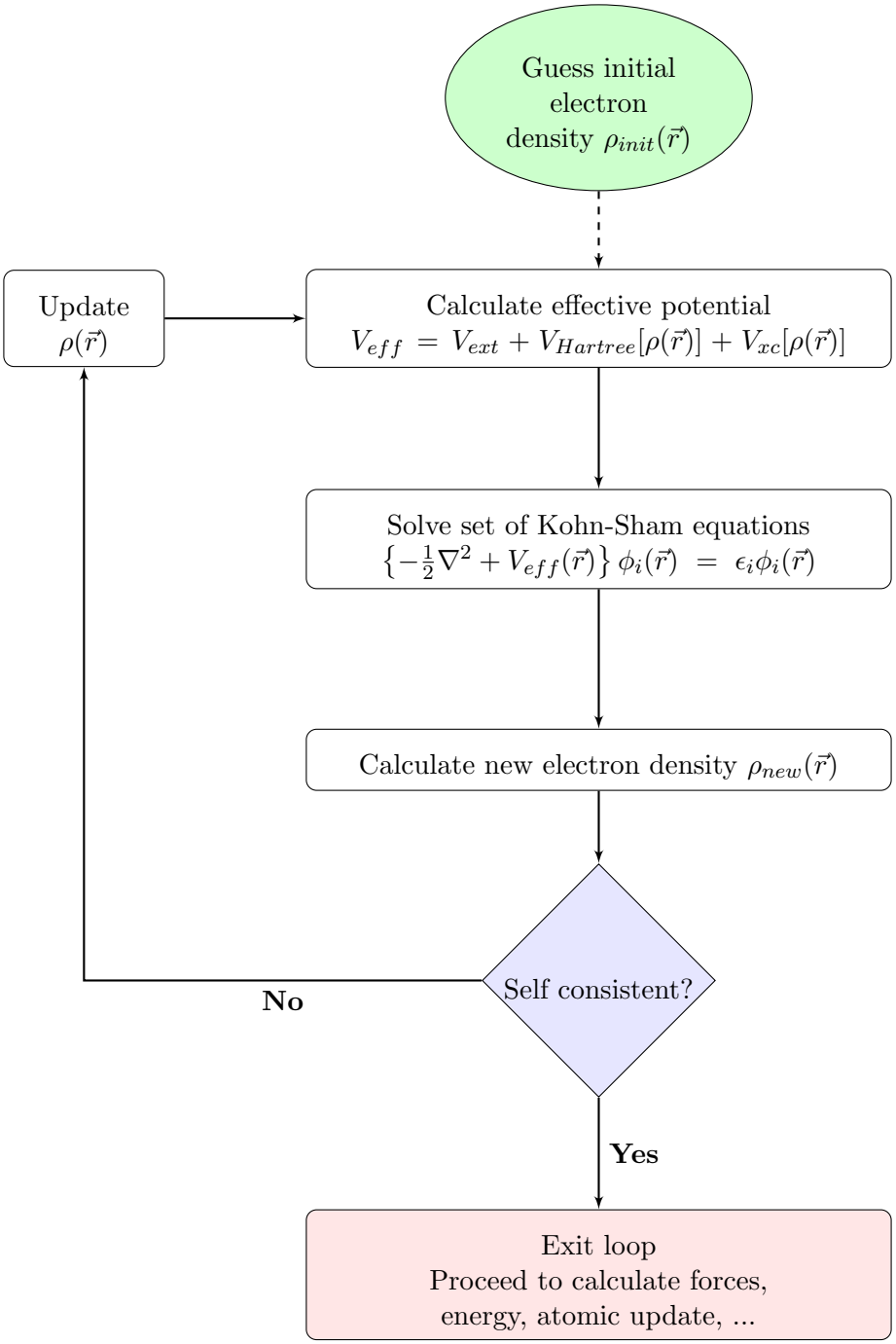

Figure 1: Typical computational workflow for solving the Kohn-Sham equations self-consistently leading to a converged electron charge density

2.2.3.1 Local Density Approximation (LDA)

In the LDA, $E_{xc}[\rho(\vec{r})]$ approximated as the integral of the exchange-correlation energy density ϵ_{xc} of a homogeneous electron gas (HEG).

$$E_{xc}^{HEG}[\rho(\vec{r})] = \int d\vec{r}\epsilon_{xc}^{HEG}[\rho(\vec{r})]\rho(\vec{r}) \tag{27}$$

$$= \int d\vec{r}\left(\epsilon_{x}^{HEG}[\rho(\vec{r})] + \epsilon_{c}^{HEG}[\rho(\vec{r})]\right)\rho(\vec{r}) \tag{28}$$

where $\epsilon_{xc}^{HEG}[\rho(\vec{r})$ itself is a sum of the exchange energy density $\epsilon_{x}^{HEG}[\rho(\vec{r})$ and the correlation energy density $\epsilon_{c}^{HEG}[\rho(\vec{r})$ of the HEG. The HEG is perhaps the simplest model for a condensed matter system. In the HEG model, the nuclei in the actual system are represented by a uniform positively charge background. The LDA was initially proposed by Kohn and Sham since exchange and correlation effects in typical solids are normally short ranged which is the case for the HEG model. Therefore, the LDA works particularly well for systems where the electron density is slowly varying or very highly localized.[58, 60] Yet, it is known that the LDA still yields remarkably good results for systems with highly inhomogeneous electron densities. This is because it preserves a number of constraints on $E_{xc}[\rho(\vec{r})]$, especially the sum rules.

The expression for $\epsilon_{x}^{HEG}[\rho(\vec{r})]$ above is exact and given by

$$\epsilon_x[\rho(\vec{r})] = -\frac{3}{4}\left(\frac{3\rho(\vec{r})}{\pi}\right)^{\frac{1}{3}}. \tag{29}$$

However, $\epsilon_{c}^{HEG}[\rho(\vec{r})]$ has no analytical expression.[58] Consequently, various approximations for $\epsilon_{c}^{HEG}[\rho(\vec{r})]$ have been proposed. The most accurate of these known to date are derived from Quantum Monte Carlo (QMC) calculations, originally proposed by Ceperley and Alder.[61, 62, 63] Other well known approximations for $\epsilon_{c}^{HEG}[\rho(\vec{r})]$ have been developed by Perdew and Zunger (PZ) as well as Vosko, Wilkes and Nusiar (VWN).[64, 65]

2.2.3.2 Generalized Gradient Approximation (GGA)

A second widely used approximation for $E_{xc}[\rho(\vec{r})]$ is the generalized gradient approximation (GGA). The modern GGA functional form for the exchange-correlation energy is given as

$$E_{xc}[\rho(\vec{r})] = \int d\vec{r}\epsilon_{xc}[\rho(\vec{r}), \nabla\rho(\vec{r})]\rho(r) \quad (30)$$

$$= \int d\vec{r}\epsilon_x^{HEG}[\rho(\vec{r})]F_{xc}[\rho(\vec{r}), \nabla\rho(\vec{r})] \quad (31)$$

which attempts to account for non-homogeneity in a real system by including information about the charge density gradient $\nabla\rho(\vec{r})$. In the above expression, $F_{xc}[\rho(\vec{r}), \nabla\rho(\vec{r})]$ is a dimensionless factor for which there exists a number of different approximations, with the most popular for solid state applications being those by Perdew and Wang (PW91) [66] as well as Perdew, Burke and Enzerhof.[67]. The exchange contribution to $F_{xc}[\rho(\vec{r}), \nabla\rho(\vec{r})]$ is $F_x[\rho(\vec{r}), \nabla\rho(\vec{r})]$ and in all cases, $F_x \geq 1$. This results in the GGA exchange energy always being lower than that predicted by the LDA. Usually, the GGA predicts lower binding energies than the LDA which normally overestimates the binding energies. In this way, the GGA generally yields results which agree better with experiment.[58]

2.2.4 Pseudopotential Methods

A pseudopotential is intended to be the effective potential acting on valence electrons which accounts for effects due to the ionic nuclei and the tightly bound core electrons. In typical molecules and solids, core electrons are normally highly localized around the nuclei. Therefore, in order for the valence electron wavefunctions to be orthogonal to the core electron wavefunctions, the valence electron wavefunctions need to be highly oscillatory, with many nodes within the core regions of the nuclei. For this to be achieved, the valence electron wavefunctions each require a huge plane wave basis set, which naturally contributes to increased computational costs. With a pseudopotential though, the resulting pseudowavefunction will be consistent with the original valence electron wavefunction outside the core regions of the nuclei and also smooth within those core regions. Therefore, we can afford to use a smaller plane wave basis set to constitute the pseudowavefunctions and this tremendously helps in keeping computational costs low. A good pseudopotential should be possible

of being generated from a simple atomic environment and still be transferable to complex environments such as molecules and solids. This is generally possible since core wavefunctions in molecules and solids are similar to their atomic forms.[58] Norm-conserving, ultrasoft and projector augmented wave pseudopotentials are three important kinds of pseudopotentials which we elaborate upon in this section.

2.2.4.1 Norm-conserving Pseudopotential

The norm-conserving pseudopotential is a popularly used type of pseudopotential originally developed by Hamann, Schlüter and Chiang.[68] Norm-conserving pseudopotentials have five fundamental characteristics. These are listed as follows:[58, 68]

1. Pseudo valence and all-electron eigenvalues agree for a given atomic configuration.

2. Pseudo valence ψ_{PS} and all-electron ψ_{AE} wavefunctions agree beyond the core radius r_c.

   Together, properties 1 and 2 imply that the norm-conserving pseudopotential must equal the atomic potential for $r > r_c$.

3. Charge densities of the pseudo valence and all-electron wavefunctions agree when integrated within the range $0 < r < r_c$.

   This property

   $$\int_0^{r_c} drr^2|\psi_{PS}(r)|^2 = \int_0^{r_c} drr^2|\psi_{AE}(r)|^2 \tag{32}$$

   is known as norm-conservation and it is particularly important for two reasons. Firstly, it guarantees a correct total charge in the core region. Secondly, it ensures that the normalized pseudo-orbital always agrees with the actual all-electron orbital outside of the core region where bonding occurs.

4. Logarithmic derivatives of the pseudo valence and all-electron wavefunctions agree for $r > r_c$.

   In other words, we consider the dimensionless quantity

   $$r\frac{d}{dr}ln\psi = r\frac{\psi'}{\psi} \tag{33}$$

to be continuous across the boundary $r = r_c$ for both pseudo valence and all-electron wavefunctions.

5. The first energy derivatives of the logarithmic derivatives of the pseudo valence and all-electron wavefunctions agree for $r > r_c$.

   It is because of property 5 that the norm-conserving pseudopotential is transferable between various simple and complex environments, as required for a good pseudopotential.[58, 68]

2.2.4.2 Ultrasoft Pseudopotentials

Ultrasoft pseudopotentials [58, 69, 70] are also commonly used in modern density functional theory. The main idea here is to radically reduce the required cutoff energy in the expansion of the pseudo wavefunctions for a given target accuracy. This has the effect of improving the smoothness (or "softness") of the pseudo wavefunctions. However, the norm-conserving condition as described above is relaxed in order for this to be achieved. The valence electron wavefunctions are also split into a smooth part $\tilde{\psi}$ and an auxiliary part which varies rapidly within the core region. The smooth wavefunctions are orthogonoalized according to

$$\langle\tilde{\psi}_i|S|\tilde{\psi}_j\rangle = \delta_{ij} \tag{34}$$

where

$$S = 1 + \sum_{ij} \Delta q_{ij} |\beta_i\rangle\langle\beta_j| \tag{35}$$

is known as the overlap operator which only differs from unity inside the core region. The $|\beta_i\rangle$ are projectors and

$$\Delta q_{ij} = \int_0^{r_c} d\vec{r}[\psi_i(\vec{r})^*\psi_j(\vec{r}) - (\psi_i(\vec{r}))^*\tilde{\psi}_j(\vec{r})] \tag{36}$$

represents the charge difference between the current choice of $\tilde{\psi}$ and the norm-conserving ψ. $\Delta q_{ij} \neq 0$ is the reason for the loss of the norm-conserving condition. The valence electron charge density is given by

$$\rho(\vec{r}) = \sum_n |\tilde{\psi}_n(\vec{r})|^2 + \sum_n \sum_{ij} [\psi_i(\vec{r})^*\psi_j(\vec{r}) - (\psi_i(\vec{r}))^*\tilde{\psi}_j(\vec{r})]\langle\tilde{\psi}_n|\beta_i\rangle\langle\beta_j|\tilde{\psi}_n\rangle. \tag{37}$$

2.2.4.3 Projector Augmented Wave (PAW) Pseudopotential

Another well known pseudopotential is the projector augmented wave pseudopotential (PAW). Like in the case of the ultrasoft pseudopotentials, PAW valence electron wavefunctions are split into a smooth part and a localized part. The smooth part of the wavefunction, which we refer to as $|\tilde{\Psi}\rangle$ is related to the full all-electron wavefunction by the transformation

$$|\Psi\rangle = T|\tilde{\Psi}\rangle. \tag{38}$$

In the above equation, T is known as the transformation operator. It is desired that T be unity only outside a sphere centered around an atomic nucleus such that $|\Psi\rangle$ and $|\tilde{\Psi}\rangle$ agree outside the atomic nucleus. Therefore, we may write

$$T = 1 + \sum_i \tau_i \tag{39}$$

where the τ_i are non-zero only within the sphere around the atomic nucleus. This region is known as the augmentation region.

Within the spherical augmentation region around an atomic nucleus, we may expand the smooth wavefunction as

$$|\tilde{\Psi}\rangle = \sum_i c_i |\tilde{\psi_i}\rangle. \tag{40}$$

For a linear transformation operator T, the c_i correspond to projections within the augmented spherical region [58, 71, 72]

$$c_i = p_i|\tilde{\Psi}\rangle \tag{41}$$

where the p_i are the required set of projection operators p_i with the property

$$\langle p_i|\tilde{\psi_j}\rangle = \delta_{ij}. \tag{42}$$

Since the full all-electron wavefunction may be written as

$$|\Psi\rangle = |\tilde{\Psi}\rangle + \sum_i c_i \left(\psi_i - \tilde{\psi_i}\right), \tag{43}$$

we see that

$$T = 1 + \sum_i \left(\psi_i - \tilde{\psi_i}\right) p_i. \tag{44}$$

In this work, we use PAW pseudopotentials for all our DFT based calculations.

2.2.5 Hellmann-Feynman Forces

Once the ground state charge density has been determined for a given configuration of ionic nuclei, the forces on the ionic nuclei are typically evaluated using the Hellmann-Feynman theorem. These forces may then be used to perform further calculations such as ionic optimisations and molecular dynamics. The Hellman-Feynman theorem states that for a system with a Hamiltonian H_λ depending on some parameter λ, then the derivative of its total energy with respect to λ is equal to the expectation value of the derivative of the Hamiltonian also with respect to λ. Simply put,

$$\frac{dE}{d\lambda} = \langle \Psi_\lambda | \frac{\partial H}{\partial \lambda} \psi_\lambda \rangle. \tag{45}$$

Proof of the Hellman-Feynman theorem is simple. We begin with the Schrödinger equation for the system

$$H_\lambda \psi_\lambda = E_\lambda \psi_\lambda \tag{46}$$

and see that the total energy is as usual given by

$$E_\lambda = \langle \psi_\lambda | H_\lambda | \psi_\lambda \rangle. \tag{47}$$

Taking the derivative with respect to λ on both sides, we have

$$\begin{aligned} \frac{dE\Psi_\lambda}{d\lambda} &= \langle \frac{d\psi_\lambda}{d\lambda} | H_\lambda | \psi_\lambda \rangle + \langle \psi_\lambda | \frac{dH_\lambda}{d\lambda} | \psi_\lambda \rangle + \langle \psi_\lambda | H_\lambda | \frac{\psi_\lambda}{d\lambda} \rangle & (48) \\ &= E_\lambda \langle \frac{d\psi_\lambda}{d\lambda} | \psi_\lambda \rangle + \langle \psi_\lambda | \frac{dH_\lambda}{d\lambda} | \psi_\lambda \rangle + E_\lambda \langle \psi_\lambda | \frac{\psi_\lambda}{d\lambda} \rangle & (49) \end{aligned}$$

Now assuming that Ψ_λ is already a normalised wavefunction of H_λ and likewise taking derivatives with respect to λ, we have

$$\begin{aligned} \langle \psi_\lambda | \psi_\lambda \rangle &= 1 & (50) \\ \langle \frac{d\psi_\lambda}{d\lambda} | \psi_\lambda \rangle + \langle \psi_\lambda | \frac{d\Psi_\lambda}{d\lambda} \rangle &= 0. & (51) \end{aligned}$$

Therefore, we see that the first and second terms of equation 49 add up to 0 and we are left with

$$\frac{dE}{d\lambda} = \langle \Psi_\lambda | \frac{\partial H}{\partial \lambda} \psi_\lambda \rangle. \tag{52}$$

which is the Hellmann-Feynman theorem.[58, 73, 74]

2.3 Statistical Mechanics

2.3.1 Statistical Mechanical Ensembles

A physical system may be thought of as having a large collection of imaginary systems which are all characterized by the exact same set of macroscopic parameters as the physical system. This collection of imaginary systems is referred to as a statistical mechanical ensemble. The systems of the ensemble are each unique according to the coordinates and momenta of their constituent particles. There are three main ensembles in statistical mechanics, namely the microcanonical, canonical and grand canonical ensembles which we describe briefly below.[75, 76]

2.3.1.1 The Microcanonical Ensemble

The microcanonical ensemble is a statistical ensemble where its members have the same number of particles (N), volume (V) and total energy (E). For this reason, it is also referred to simply as the NVE ensemble. The microcanonical ensemble can only describe a completely isolated system which does not exchange heat or matter with its surroundings.[75]

2.3.1.2 The Canonical Ensemble

In actual experiments, it is usually temperature rather than energy which is kept constant in a system. The canonical ensemble describes such a system with a fixed number of particles (N), volume (V) and temperature (T) so it is commonly known as the NVT ensemble. A system in the canonical ensemble is closed to prevent particle exchange with its surroundings as is the case with the microcanonical ensemble. However, it is thermally coupled with its surroundings, referred to as the heat bath or reservoir, with which it exchanges energy so as to maintain its temperature.

In the canonical ensemble, the probability of the system being in a particular microstate i with total energy E_i is

$$P(i) = \frac{1}{Z} e^{-\beta E_i}. \tag{53}$$

In the above equation, we introduce the commonly occurring quantity

$$\beta = \frac{1}{k_B T} \tag{54}$$

where k_B is the Boltzmann constant. The quantity Z is known as the canonical partition function

$$Z = \sum_i e^{-\beta E_i}. \tag{55}$$

Z, also known as the "sum-over-states", may be viewed as a normalization constant which guarantees that the sum of all $P(i)$ is unity.[75]

Using the canonical partition function, the expectation value for energy $\langle E \rangle E$ may be expressed rather elegantly as [75]

$$\begin{aligned} \langle E \rangle &= \sum_i E_i P_i & (56) \\ &= \frac{1}{Z} \sum_i E_i e^{-\beta E_i} & (57) \\ &= -\frac{\partial ln Z}{\partial \beta}. & (58) \end{aligned}$$

2.3.1.3 The Grand Canonical Ensemble

The grand canonical ensemble or μVT ensemble best describes an open system which allows for both particle and energy exchange so as to keep chemical potential (μ), volume (V) and temperature (T) constant.

The grand canonical partition function is

$$\Xi = \sum_i e^{\beta(N_i \mu - E_i)} \tag{59}$$

where N_i is the total number of particles in microstate i. Similar in form to its canonical ensemble counterpart, the probability of the system being in a particular microstate i within the grand canonical ensemble is [75]

$$P(i) = \frac{1}{\Xi} e^{\beta(N_i \mu - E_i)}. \tag{60}$$

2.3.2 Maxwell-Boltzmann Distribution

Consider a classical ideal gas system with N particles at equilibrium temperature T. We seek to find the probability distribution f_v for the particles at various speeds v. The probability of finding N_i particles with energy E_i is

$$N_i = \frac{N}{Z} e^{-\beta E_i}. \tag{61}$$

Here, Z is the partition function for a single particle which is the same for all particles. First assuming this to be a 1D system, we may rewrite the above probability in terms of momentum

$$N_i = \frac{N}{Z} e^{-\beta \frac{p_i^2}{2m}}. \tag{62}$$

which is proportional to the momentum probability distribution f_p. Of course, momentum is a continuous variable so we write

$$\int f_p dp = C \int \frac{1}{Z} e^{-\beta \frac{p^2}{2m}} dp = 1. \tag{63}$$

where C is the normalization constant. Evaluating the gaussian integral, we find that

$$C = Z \sqrt{\frac{\beta}{2\pi m}} \tag{64}$$

Hence, we see that

$$f_p = \sqrt{\frac{\beta}{2\pi m}} e^{-\beta \frac{p^2}{2m}}. \tag{65}$$

In the 3D case, the momentum probability distribution is easily generalized to

$$f_p = \left(\frac{\beta}{2\pi m} \right)^{\frac{3}{2}} e^{-\beta \frac{p^2}{2m}} \tag{66}$$

Finding the scalar speed probability distribution simply involves a change of variables from the 3D momentum vector representation.

$$\begin{aligned} \int f_p d\vec{p} &= \int \left(\frac{\beta}{2\pi m} \right)^{\frac{3}{2}} e^{-\beta \frac{p^2}{2m}} dp_x dp_y dp_z & (67) \\ &= \int \left(\frac{\beta m}{2\pi} \right)^{\frac{3}{2}} e^{-\beta \frac{mv^2}{2}} dv_x dv_y dv_z & (68) \\ &= \int \left(\frac{\beta m}{2\pi} \right)^{\frac{3}{2}} e^{-\beta \frac{mv^2}{2}} v^2 sin\theta dv d\theta d\phi & (69) \end{aligned}$$

where it is clear that

$$f_v = 4\pi v^2 \left(\frac{\beta m}{2\pi} \right)^{\frac{3}{2}} e^{-\beta \frac{mv^2}{2}} \tag{70}$$

which is the well known Maxwell-Bolztmann velocity distribution.[75, 76]

2.3.3 Pair Correlation Functions

The partial pair correlation function $g_{\alpha\beta}(r)$ is a measure of the probability of finding an atom of species β at various distances around a reference atom of species α. This reveals the structural details of solid and even liquid systems.

$$g_{\alpha\beta}(r) = \frac{1}{N_\alpha \rho_\beta} \left\langle \sum_{i=1}^{N_\alpha} \sum_{j=1}^{N_\beta} \delta(\vec{r} + \vec{r}_i - \vec{r}_j) \right\rangle . \tag{71}$$

The angular brackets refer to an average over various configurations of the system over time in a regular molecular dynamics simulation. In practice, we deal with the 3D Dirac Delta function $\delta(\vec{r})$ by defining very thin spherical shells around each reference particle and counting the number of neighbours it has within each shell. $g_{\alpha\beta}(r)$ vanishes at small r due to short range repulsion. For large r in the case of liquids which lack long range structure, $g_{\alpha\beta}(r) = 1$ typically. This is because $g_{\alpha\beta}(r)$ is normalized by the mean particle number density $\rho_\beta = \frac{N_\beta}{V}$ and so $g_{\alpha\beta}(r) = 1$ indicates a completely random structure. The average number of particles within a range of r to $r + dr$ of a reference particle may be estimated as $4\pi r^2 g_{\alpha\beta}(r)dr$. This further allows us to estimate its coordination number as $N_{\alpha\beta}$

$$N_{\alpha\beta} = \int_0^{R_{min}} 4\pi r^2 g_{\alpha\beta}(r)dr \tag{72}$$

where R_{min} is the first minimum of $g_{\alpha\beta}(r)$.[76, 77]

The total pair correlation function $g(r)$ may be obtained from a weighted sum of the various partial pair correlation functions

$$g(r) = \frac{\sum_\alpha \sum_\beta x_\alpha x_\beta b_\alpha b_\beta g_{\alpha\beta}(r)}{\sum_\alpha \sum_\beta x_\alpha x_\beta b_\alpha b_\beta} \tag{73}$$

where x_α is the molar concentration of atomic species α. $g(r)$ may be obtained experimentally by neutron or x-ray scattering. As such b_α may represent either neutron scattering lengths or atomic form factors as appropriate to the type of scattering experiment being used to calculate $g(r)$.[77]

2.3.4 Static Structure Factors

Static structure factors are obtained by Fourier transforming the pair correlation functions. Since $g(r)$ depends only on the magnitude r, the Fourier transform can be vastly simplified.

Furthermore, $S(k)$ will depend only on the magnitude k in the same spirit.

$$\begin{aligned} S(k) &= \int d\vec{r} e^{i\vec{k}\cdot\vec{r}} \rho g(r) && (74) \\ &= \int r^2 sin(\theta) e^{ikrcos(\theta)} \rho g(r) r^2 dr d\theta d\phi && (75) \\ &= -2\pi\rho \int \left[\frac{e^{ikrcos(\theta)} g(r)}{ikr} \right]_{cos(\theta)=1}^{cos(\theta)=-1} dr && (76) \\ &= 4\pi\rho \int \frac{sin(kr) g(r)}{kr} r^2 dr && (77) \end{aligned}$$

This works equally well for both partial and total static structure factors. Partial static structures also combine using the Faber-Ziman formalism to give the total static structure factor [77]

$$S(k) = \frac{\sum_\alpha \sum_\beta x_\alpha x_\beta b_\alpha b_\beta S_{\alpha\beta}(k)}{\sum_\alpha \sum_\beta x_\alpha x_\beta b_\alpha b_\beta}. \quad (78)$$

2.3.5 Diffusion

Fick's law states that the diffusive flux J of a particular atomic species is directly proportional to the negative of its concentration gradient.

$$J = -D\nabla c(\vec{r}, t) \quad (79)$$

where $c(\vec{r}, t)$ is the concentration and the constant of proportionality D is commonly known as the diffusion coefficient.

Let us consider the case where a particular atomic species is initially concentrated at $\vec{r} = 0$. Simply put, $c(\vec{r}, 0) = \delta(\vec{r}, 0)$ and we also demand that $\int c(\vec{r}, t) d\vec{r} = 1$. The time evolution of $c(\vec{r}, t)$ may then be studied by applying the continuity equation

$$\nabla \cdot J = -\frac{\partial c(\vec{r}, t)}{\partial t}. \quad (80)$$

By multiplying the continuity equation with r^2 and integrating over all space, we have

$$D \int r^2 \nabla^2 c(\vec{r}, t) d\vec{r} = \int r^2 \frac{\partial c(\vec{r}, t)}{\partial t} d\vec{r}. \quad (81)$$

It is reasonable to consider a J that vanishes at infinity so the left hand term may be integrated by parts to yield $2N_{dim}D$ where N_{dim} is the number of spatial dimensions. Using

the boundary condition $\int c(\vec{r},t)d\vec{r} = 1$, we see that the right hand term is simply equivalent to $\frac{\partial\langle\Delta r^2(t)\rangle}{\partial t}$ where $\langle\Delta r^2(t)\rangle = \frac{1}{N}\sum_{i=1}^{N}|r_i(t) - r_i(0)|^2$ is the mean squared displacement (MSD) of N atoms. Therefore, the diffusion coefficient is directly proportional to the gradient of the MSD.[78]

$$D = \frac{1}{2N_{dim}}\frac{\partial\langle\Delta r^2(t)\rangle}{\partial t} \tag{82}$$

This is a very useful relation as it provides a practical method for evaluating the diffusion coefficient in MD simulations using only atomic displacements.[78]

2.3.6 Time Correlation Functions

The time correlation function $C_{AB}(t)$ between two functions A and B is given by

$$C_{AB}(t) = \langle A(t+t_0)B(t_0)\rangle = \lim_{\tau\to\infty}\frac{1}{\tau}\int_0^{\infty} A(t+t_0)B(t_0)dt_0. \tag{83}$$

where the angled brackets refer to the time average. Since equilibrium probability densities are independent of time, $C_{AB}(t)$ is invariant under any translation in time. A special class of time correlation functions is the autocorrelation function where A and B are identical to each other.[76]

2.3.6.1 The Velocity Autocorrelation Function

The velocity autocorrelation function (VACF) in MD simulations yields particularly important information.[76, 77, 78] Firstly, the diffusion coefficient D introduced in the previous subsection may also be calculated using the VACF instead of the MSD.

$$\begin{aligned}
\frac{\partial\langle\Delta r^2(t)\rangle}{\partial t} &= \frac{\partial}{\partial t}\left\langle\int_0^t \vec{v}(t')dt'\cdot\int_0^t \vec{v}(t'')dt''\right\rangle &(84)\\
&= 2\frac{\partial}{\partial t}\int_0^t dt'\int_0^{t'} dt''\langle\vec{v}(t')\cdot\vec{v}(t'')\rangle &(85)\\
&= 2\int_0^t dt''\langle\vec{v}(t)\cdot\vec{v}(t'')\rangle &(86)\\
&= 2\int_0^t dt'\langle\vec{v}(t)\cdot\vec{v}(t+t')\rangle &(87)
\end{aligned}$$

where we perform a simple substitution $t'' = t' + t$ in the final step. Recall that the angled brackets refer to an average over the number of atoms. In practice, this is often and

equally well extended to be the average over both atoms and time. Hence, we recognise $Z(t) = \langle \vec{v}(t) \cdot \vec{v}(t+t') \rangle$ as the VACF.[77] Combining equations 82 and 87, we have

$$D = \frac{1}{N_{dim}} \int_0^\infty Z(t) dt. \tag{88}$$

Evaluating the diffusion coefficient using the distinct VACF and MSD methods provides a good consistency check. Secondly, the power spectrum obtained by Fourier transforming the VACF,

$$\hat{Z}(\omega) = \frac{1}{2\pi} \int Z(\tau) e^{i\omega t} dt \tag{89}$$

is useful for studying the vibrational properties of a system as it is directly proportional to the phonon density of states.[76, 77]

2.4 Molecular Dynamics

Molecular dyanmics (MD) is a technique for computationally simulating particle motion within a system over time. Here we are primarily concerned with first-principles MD. In this scenario, forces on the particles are computed using the Hellmann-Feynman theorem, which is a quantum mechanical principle. However, the particle motion resulting from these Hellman-Feynman forces are determined entirely by the classical Newtonian equations of motion.[58, 76, 77, 78]

2.4.1 Verlet Algorithm

The Verlet algorithm is arguably the most widely used method for solving the Newtonian equations of motion in order to update particle trajectories in MD simulations. This method does not make use of particle velocities. Instead, it requires only particle positions and accelerations. To understand this method, first consider the Taylor expansions of $\vec{r}(t + \Delta t)$ and $\vec{r}(t - \Delta t)$ about $\vec{r}(t)$.

$$\vec{r}(t + \Delta t) = \vec{r}(t) + (\Delta t)\vec{v}(t) + \frac{1}{2}\Delta t^2 \vec{a}(t) + \mathcal{O}(\Delta t^3) \tag{90}$$

$$\vec{r}(t - \Delta t) = \vec{r}(t) - (\Delta t)\vec{v}(t) + \frac{1}{2}\Delta t^2 \vec{a}(t) - \mathcal{O}(\Delta t^3) \tag{91}$$

Adding both equations, we see that the velocity terms $\vec{v}(t)$ cancel out and simple rearrangement gives

$$\vec{r}(t+\Delta t) = 2\vec{r}(t) - \vec{r}(t-\Delta t) + (\Delta t)^2\vec{a}(t) + \mathcal{O}(\Delta t^4) \tag{92}$$

which is accurate to fourth order in Δt. The advantage of not having to make explicit use of the velocities is that velocities are usually accurate to only $(\Delta t)^2$. Also, the Verlet algorithm allows particle coordinates to be updated in a single step which keeps computational costs low.[76]

2.4.2 Temperature Fluctuations

In this section, we shall see that the temperature of a system in the canonical ensemble always experiences finite temperature fluctuations. By the equipartition theorem, each degree of freedom for each of the N particles in a system contributes $\frac{3}{2}k_BT$ of energy to the total energy of the system. Following this, the temperature T of the system is related to the kinetic energy of the system by

$$\frac{3}{2}Nk_BT = \sum_i \frac{1}{2}m_i|v_i|^2 = \sum_i \frac{1}{2}\frac{|p_i|^2}{2m_i}. \tag{93}$$

However, we realise that there are fluctuations in the kinetic energy of the individual particles. This is quantified by the coefficient of variance in the kinetic energy. We have

$$\begin{aligned}
\langle p^2\rangle &= \int f_p p^2 d\vec{p} && (94)\\
&= \int \left(\frac{\beta}{2\pi m}\right)^{\frac{3}{2}} p^4 e^{-\beta\frac{p^2}{2m}} sin\theta dp d\theta d\phi && (95)\\
&= 3\frac{m}{\beta} && (96)
\end{aligned}$$

and

$$\begin{aligned}
\langle p^4\rangle &= \int f_p p^4 d\vec{p} && (97)\\
&= \int \left(\frac{\beta}{2\pi m}\right)^{\frac{3}{2}} p^6 e^{-\beta\frac{p^2}{2m}} sin\theta dp d\theta d\phi && (98)\\
&= 15\left(\frac{m}{\beta}\right)^2. && (99)
\end{aligned}$$

Therefore the coefficient of variance in the kinetic energy is

$$\frac{\sigma_p^2}{\langle p\rangle^2} = \frac{\langle p^4\rangle - \langle p^2\rangle}{\langle p^2\rangle} = \frac{2}{3}. \tag{100}$$

which is finite and manifests itself as temperature fluctuations. Assuming the particles to be non-interacting such that we deal with an uncorrelated system, the expected relative variance or fluctuation in temperature is simply [78]

$$\frac{\sigma_T^2}{\langle T \rangle^2} = \frac{2}{3N}. \tag{101}$$

2.4.3 Nóse-Hoover Thermostat

From the previous subsection, we see that the canonical ensemble has finite temperature fluctuations. In molecular dynamics, the main aim of a thermostat is to simulate these characteristic temperature fluctuations while simultaneously fixing the mean temperature at a specified level. It is in this sense that the temperature is said to be held constant when simulating a system in the canonical ensemble. The Nóse-Hoover thermostat is a popular algorithm for simulating such a constant temperature environment. The basis for this method was first proposed by Nóse [79] and further developed by Hoover [80].

The Nóse-Hoover thermostat is formulated by adding an extra coordinate s to the Nóse Hamiltonian H_N. s functions as an additional degree of freedom for the simulated heat bath.

$$H_N = \sum_i^N \frac{|\vec{p}_i|^2}{2m_i s^2} + \sum_{j>i} U_{ij} + \frac{p_s^2}{2Q} + 3Nk_BT\ ln(s) \tag{102}$$

Q is a fictitious mass which is coupled to s, In the above equation,

$$\vec{p}_i = m_i s^2 \dot{\vec{r}}_i \tag{103}$$

$$p_s = Q\dot{s} \tag{104}$$

U_{ij} refers to the interatomic potential between atomic pairs. It is from this modified Hamiltonian H_N that the equations of motions are then derived. These equations of motion are [78]

$$\dot{\vec{r}}_i = \frac{\vec{p}_i}{m_i s^2} \tag{105}$$

$$\dot{\vec{p}}_i = -\frac{\partial U_{ij}}{\partial \vec{r}_i} \tag{106}$$

$$\dot{s} = \frac{p_s}{Q} \tag{107}$$

$$\dot{p}_s = \frac{1}{s}\left(\sum_i^N \frac{|\vec{p}_i|^2}{m_i s^2} - 3Nk_BT\right) \tag{108}$$

2.5 The Thermoelectric Effect

The thermoelectric effect refers to the conversion of temperature differences into voltage differences. This effect is very useful for converting waste heat into useful electrical energy. We show in Fig. 2 a simple schematic of a thermoelectric generator making use of both p and n doped thermoelectric materials. From it, we see excited carriers from the hot side diffusing over the cold side and establishing the desired electrical current in the process. An actual thermoelectric generator would consist of many more p and n type thermoelectric legs in parallel between the heat source and heat sink. This set up in fact allows the size of a thermoelectric generator to be easily scaled to fit applications of various shapes and sizes. Typical thermoelectric generators do not contain any moving parts which also makes them very silent and easy to maintain. The thermoelectric generator shown in Fig. 2 may of course also be run in reverse as a solid state refrigerator. Unfortunately, despite the immense utility of thermoelectric devices, and the fact that the thermoelectric effect has been known for the past two centuries, there has been little progress in this field until the past two decades. This is simply because the thermoelectric efficiency of most regular materials is far too low. Indeed, good thermoelectric materials often have rather complicated structures which typically have to be artificially engineered or enhanced. These structures typically disrupt phonon transport while having little effect on the electronic transport properties so as to maximize thermoelectric efficiency. For example, skutterudites [81] and clathrates [81, 82] are two classes of materials characterised by their very large and open unit cells. Guest atoms can be incorporated into these cage like cells where they introduce new phonon rattling modes [81, 82] that disrupt the lattice thermal conductivity. Other examples include the use of grain boundaries and alloy scattering to scatter phonons as in the case of silicon-germanium (SiGe) thermoelectrics.[40, 41, 42]

2.5.1 Thermoelectric Efficiency and Figure of Merit

The thermoelectric efficiencies of various materials are compared against each other by their dimensionless figures of merit ZT.[83, 84] The ZT value is related to the Carnot efficiency of the thermoelectric device employing the thermoelectric material such as the one illustrated

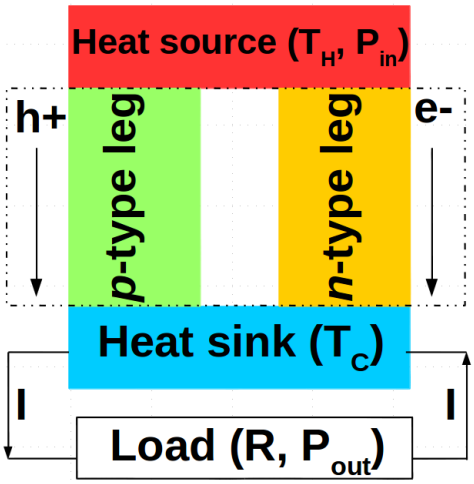

Figure 2: Schematic of a typical thermoelectric generator. The n and p doped legs are made from the actual thermoelectric material, outlined by the dot-dashed border.

in Fig. 2. The definition of ZT is credited to Ioffe.[84] Recall that the Carnot efficiency represents the theoretical maximum efficiency of any heat engine.[75]

Let us refer again to Fig. 2 as we derive the Carnot efficiency η of a thermoelectric generator. In doing so, we assume that the dimensions and all material properties, such as electrical and thermal conductivities, of both p and n type thermoelectric materials are identical. We first consider the input heat energy per unit time (P_{in}) into the device. This is given as

$$P_{in} = \frac{\Delta T}{R_\theta} + ST_H I - \frac{1}{2} I^2 r. \tag{109}$$

The three terms on the right hand side of this equation respectively represent heating due to thermal transfer from the heat source, Peltier heating [85, 86] and heat dissipation due to internal resistance. $\Delta T = T_H - T_C$ is the temperature difference between the hot and cold reservoirs at T_H and T_C respectively. $R_\theta = \frac{l}{\kappa A}$ is the thermal resistance with l and A respectively being length and area of the thermoelectric legs and κ being the thermal conductivity. I is the current flowing through the external load with electrical resistance R. $r = \frac{l}{\sigma A}$ is the internal electrical resistance of the thermoelectric generator where σ is the corresponding electrical conductivity. S represents the most interesting material quantity known as the Seebeck coefficient. The Seebeck coefficient is given as

$$S = -\frac{\Delta V}{\Delta T} \tag{110}$$

from which we see that it qualitatively represents the amount of useful electrical voltage that can be obtained for a given temperature difference. Knowing this, we can write the current through the external load as

$$I = \frac{S\Delta T}{r+R} \tag{111}$$

The output power of the external load is

$$P_{out} = I^2 R = \frac{S^2 \Delta T^2 R}{(r+R)^2}. \tag{112}$$

The Carnot efficiency is related to the input and output powers via

$$\eta = \frac{P_{out}}{P_{in}} = \frac{\Delta T}{T_H} \cdot \frac{S^2 R}{(r+R)^2} \left(\frac{1}{T_H R_\theta} - \frac{S^2 r \Delta T}{2T_H (r+R)^2} + \frac{S^2}{r+R} \right)^{-1}. \tag{113}$$

To find the $R = R_{max}$ corresponding to the maximum η, we solve for

$$\frac{d\eta}{dR} = 0 \tag{114}$$

which leads us to

$$\begin{aligned} R_{max} &= r\sqrt{1 + \frac{S^2\sigma}{\kappa} \cdot \frac{1}{2}(T_H + T_C)} && (115) \\ &= r\sqrt{1+ZT} && (116) \end{aligned}$$

where we define

$$\begin{aligned} ZT &= \frac{S^2\sigma}{\kappa} \cdot \frac{1}{2}(T_H + T_C) && (117) \\ &= \frac{S^2\sigma T}{\kappa}. && (118) \end{aligned}$$

Note that ZT is defined with respect to the average temperature T between the hot and cold reservoirs. The quantity $S^2\sigma$ depends only on electronic transport properties. The thermal conductivity in the numerator $\kappa = \kappa_e + \kappa_l$ is the sum of electronic (k_e) and lattice thermal conductivities (k_l). Substituting $R = R_{max}$ back into Eq. 113, we find that

$$\eta_{max} = \frac{T_H - T_C}{T_H} \cdot \frac{\sqrt{1+ZT} - 1}{\sqrt{1+ZT} + \frac{T_C}{T_H}} \tag{119}$$

represents the maximum possible Carnot efficiency for the thermoelectric generator.[83, 84] ZT very neatly rolls into a single term all the material properties which influence thermoelectric efficiency.

2.6 Boltzmann Transport Theory

Boltzmann transport theory enables us to calculate various thermoelectric quantities of interest, namely the electrical conductivity (σ) and Seebeck (S) coefficient, directly from electronic band structures.[85, 86, 87]

Charge carrier transport is influenced by various factors such as external electromagnetic fields and temperature gradients. We capture the essence of these effects by studying the variation of the non-equilibrium distribution function $f_{n,\vec{k}}(\vec{r},t)$ where n is labels the band index. The behaviour of $f_{\vec{k}}(\vec{r},t)$ is governed by the Boltzmann transport equation [86] which we set up by considering the following mechanisms:

1. External electric field

   An external electric field $\vec{E}$ exerts a force on a carrier with charge q and changes its momentum according to

   $$\frac{\partial(\hbar\vec{k})}{\partial t} = q\vec{E}. \tag{120}$$

   Assuming that the $f_{n,\vec{k}}(\vec{r},t)$ is constant along the trajectory of the system (Liouville's theorem [85, 86]), we can write

   $$f_{n,\vec{k}}(\vec{r},t) = f_{n,\vec{k}-t\partial_t\vec{k}}(\vec{r},0). \tag{121}$$

   Therefore we have

   $$\left.\frac{\partial f_{n,\vec{k}}(\vec{r},t)}{\partial t}\right|_{E-field} = -\frac{\partial\vec{k}}{\partial t}\cdot\frac{\partial f_{n,\vec{k}}(\vec{r},t)}{\partial\vec{k}} \tag{122}$$

   $$= -\frac{q}{\hbar}\vec{E}\cdot\frac{\partial f_{n,\vec{k}}(\vec{r},t)}{\partial\vec{k}} \tag{123}$$

   as a result of external electric field $\vec{E}$.

2. Carrier diffusion

   Carriers with velocity $\vec{c}_{n,\vec{k}}$ will be displaced by $\vec{c}_{n,\vec{k}}t$ in time t. Again assuming Liouville's theorem as with the case for external electric field scattering, we may write

   $$f_{n,\vec{k}}(\vec{r},t) = f_{n,\vec{k}}(\vec{r}-\vec{c}_{n,\vec{k}}t,0) \tag{124}$$

from which it naturally follows that

$$\left.\frac{\partial f_{n,\vec{k}}(\vec{r},t)}{\partial t}\right|_{diffusion} = -\vec{c}_{n,\vec{k}}\frac{\partial f_{n,\vec{k}}(\vec{r},t)}{\partial \vec{r}} \tag{125}$$

due to carrier diffusion.

3. Scattering

   The effect of scattering on $f_{n,\vec{k}}(\vec{r},t)$ is considerably more complicated than the above-mentioned effects. For now, we shall simply refer to it as

$$\left.\frac{\partial f_{n,\vec{k}}(\vec{r},t)}{\partial t}\right|_{scattering}. \tag{126}$$

   We assign its form as we discuss the relaxation time approximation below.

Combining the effects of diffusion, external electric field $\vec{E}$ and scattering, we have the Boltzmann transport equation

$$\left.\frac{\partial f_{n,\vec{k}}(\vec{r},t)}{\partial t}\right|_{diffusion} + \left.\frac{\partial f_{n,\vec{k}}(\vec{r},t)}{\partial t}\right|_{E-field} + \left.\frac{\partial f_{n,\vec{k}}(\vec{r},t)}{\partial t}\right|_{scattering} = 0 \tag{127}$$

for describing the steady state evolution of $f_{n,\vec{k}}(\vec{r},t)$.[86]

2.6.1 Relaxation Time Approximation

In order to make any progress in using Eq. 127, we need to have a form for $f_{n,\vec{k}}(\vec{r},t)$ and $\partial_t f_{n,\vec{k}}(\vec{r},t)|_{scattering}$. For this, we turn to the relaxation time approximation.[85] In the relaxation time approximation, the probability of an electron undergoing a collision within the time interval dt is

$$\frac{dt}{\tau_{n,\vec{k}}(\vec{r})}. \tag{128}$$

Generally. the relaxation time $\tau_{n,\vec{k}}(\vec{r})$ depends on band index as well as position. However, in our approach, we shall treat it as a constant $\tau_{n,\vec{k}}(\vec{r}) = \tau$. Furthermore, we assume that the form of the non-equilibrium distribution function

$$f_{n,\vec{k}}(\vec{r},t) = \frac{1}{e^{(\epsilon_{n,\vec{k}}-\mu(\vec{r}))/(k_B T(\vec{r}))}+1} \tag{129}$$

is essentially the same functional form as that of the Fermi-Dirac distribution although we explicitly label temperature $T(\vec{r})$ and chemical potential $\mu(\vec{r})$ as being position dependent.

In addition, we assume that the functional form of $f_{n,\vec{k}}(\vec{r},t)$ is not altered by collisions. Since collisions actually result in electrons switching bands and momentum, this must mean that

$$df_{n,\vec{k}}(\vec{r},t) = -\frac{dt}{\tau(\vec{r})} f_{n,\vec{k}}(\vec{r},t). \tag{130}$$

Now returning to the scattering effect on $f_{n,\vec{k}}(\vec{r},t)$, we can write

$$\left.\frac{\partial f_{\vec{k}}(\vec{r},t)}{\partial t}\right|_{scattering} = -\frac{f_{n,\vec{k}}(\vec{r},t)}{\tau}. \tag{131}$$

Now we return to Eq. 127 and substitue for the diffusion, external electric field and scattering contributions.[85, 86] This gives us

$$\begin{aligned}
\left.\frac{\partial f_{n,\vec{k}}}{\partial t}\right|_{scattering} &= \left.\frac{\partial f_{n,\vec{k}}}{\partial t}\right|_{E-field} + \left.\frac{\partial f_{n,\vec{k}}}{\partial t}\right|_{diffusion} && (132)\\
\frac{f_{n,\vec{k}}(\vec{r},t)}{\tau} &= -\frac{q}{\hbar}\vec{E}\cdot\frac{\partial f_{n,\vec{k}}}{\partial \vec{k}} - \vec{c}_{n,\vec{k}}\frac{\partial f_{n,\vec{k}}}{\partial \vec{r}} && (133)\\
&= -\frac{q}{\hbar}\vec{E}\cdot\frac{\partial f_{n,\vec{k}}}{\partial \epsilon_{n,\vec{k}}}\frac{\partial \epsilon_{n,\vec{k}}}{\partial \vec{k}} - \vec{c}_{n,\vec{k}}\frac{\partial f_{n,\vec{k}}}{\partial \mu}\frac{\partial \mu}{\partial \vec{r}} - \vec{c}_{n,\vec{k}}\frac{\partial f_{n,\vec{k}}}{\partial T}\frac{\partial T}{\partial \vec{r}} && (134)\\
&= -\frac{\partial f_{n,\vec{k}}}{\partial \epsilon_{n,\vec{k}}}\vec{c}_{n,\vec{k}}\cdot\left(q\vec{E} - \frac{\partial \mu}{\partial \vec{r}} - \frac{\epsilon_{n,\vec{k}}-\mu}{T}\frac{\partial T}{\partial \vec{r}}\right) && (135)\\
&\equiv -\frac{\partial f_{n,\vec{k}}}{\partial \epsilon_{n,\vec{k}}}\vec{c}_{n,\vec{k}}\cdot\left(q\vec{E} - \frac{\epsilon_{n,\vec{k}}-\mu}{T}\frac{\partial T}{\partial \vec{r}}\right). && (136)
\end{aligned}$$

Above, we use the relations $\partial_{\vec{k}}\epsilon = c$, $\partial_\mu f = -\partial_\epsilon f$ and $\partial_T f = -\frac{\epsilon-\mu}{T}\partial_\epsilon f$. In the last step, we also drop the $\partial_{\vec{r}}\mu$ term as the electric field due to the gradients in the chemical potential may be jointly described with the external electric field $\vec{E}$. Finally, we see that

$$f_{n,\vec{k}} = -\frac{\partial f_{n,\vec{k}}}{\partial \epsilon_{n,\vec{k}}}\tau c_{n,\vec{k}}\cdot\left(q\vec{E} - \frac{\epsilon_{n,\vec{k}}-\mu}{T}\frac{\partial T}{\partial \vec{r}}\right). \tag{137}$$

2.6.2 Current Density

The most well known form of the current density [86] is

$$\vec{J} = \sigma(\vec{E} + S\nabla T). \tag{138}$$

However, the current density can also be calculated from $f_{n,\vec{k}}$ as

$$\begin{aligned}
\vec{J} &= \frac{1}{4\pi^3}\int q\vec{c}_{n,\vec{k}} f_{n,\vec{k}} d\vec{k} && (139)\\
&= -\frac{1}{4\pi^3}\int \frac{\partial f_{n,\vec{k}}(\vec{r},t)}{\partial \epsilon_{n,\vec{k}}}\tau c_{n,\vec{k}} c_{n,\vec{k}}\left(q^2\vec{E} - \frac{q}{T}(\epsilon_{n,\vec{k}}-\mu)\frac{\partial T}{\partial \vec{r}}\right)d\vec{k} && (140)
\end{aligned}$$

Comparing Eqs. 138 and 140, we deduce that

$$\sigma_{\alpha\beta}(\mu,T) = -q^2\sum_n\int\frac{d\vec{k}}{4\pi^3}\frac{\partial f_{n,\vec{k}}(\mu,T)}{\partial\epsilon_{n,\vec{k}}}\tau c^{\alpha}_{n,\vec{k}}c^{\beta}_{n,\vec{k}} \quad (141)$$

$$\sigma_{\alpha\gamma}S_{\gamma\beta}(\mu,T) = -\frac{q}{T}\sum_n\int\frac{d\vec{k}}{4\pi^3}(\epsilon_{n,\vec{k}}-\mu)\frac{\partial f_{n,\vec{k}}(\mu,T)}{\partial\epsilon_{n,\vec{k}}}\tau c^{\alpha}_{n,\vec{k}}c^{\beta}_{n,\vec{k}} \quad (142)$$

in the appropriate tensor notation.[85, 86] We are primarily interested in how σ and S behave as functions of chemical potential μ and temperature T. The electrical conductivity σ given by Eq. 141 is a function of the constant relaxation time τ. On the other hand, we see from Eq. 142 that the Seebeck coefficient is calculated by multiplying $\sigma_{\alpha\gamma}S_{\gamma\beta}(\mu,T)$ with the inverse of $\sigma_{\alpha\beta}(\mu,T)$. This cancels out the unknown constant relaxation time in Eq. 142 such that the Seebeck coefficient in our approach is evaluated without knowledge of the relaxation time. We make use of the BoltzTraP package [87] to perform the above Boltzmann transport calculations. The only required input for BoltzTraP is the electronic band structure which provides information about $c_{n,\vec{k}}$ and $\epsilon_{n,\vec{k}}$. The electronic band structures are evaluated from first-principles using the VASP. However, the calculation of the electronic relaxation time is beyond the scope of this work and so we treat it simply as an unknown constant. As mentioned, this is not an issue when evaluating the Seebeck coefficient but in the work that follows, we report the calculated electrical conductivity as σ/τ.[87]

CHAPTER III

SURFACE PASSIVATION AND ORIENTATION DEPENDENCE IN THE ELECTRONIC PROPERTIES OF SILICON NANOWIRES

3.1 Introduction

The electronic properties of one-dimensional (1D) silicon nanowires (SiNWs) are vastly different from the electronic properties of bulk silicon. This is particularly due to the increased quantum confinement of electrons within SiNWs. Most notably, this leads to a direct band gap in SiNWs which is a huge advantage over bulk silicon as it leads increased optical sensitivity, thereby making way for various new technological applications. It is also known that the size of the direct band gap in SiNWs may be tuned simply by adjusting their diameters. Recent advances in engineering have also led to the low cost and manufacturing ease of high quality SiNW arrays.[4, 5, 6] As such, SiNWs have garnered much attention for applications as diverse as solar cells,[7, 8, 9, 10] sensors [20, 88, 89] and thermoelectric devices.[11, 12, 13, 14, 15] Unfortunately, SiNWs are prone to degradation when exposed to the environment over long periods of time. Therefore, much effort has been devoted towards improving their ambient stability, in order to enhance their utility. Chemical surface passivation is one particular method for improving the ambient stability of SiNWs. In particular, CH_3 passivation has shown to dramatically increase the stability of SiNWs, even to the point of making them resistant electrolytic oxidation and corrosion such that they are viable in photoelectrochemical water splitting cells.[16, 17, 18]

Surface passivation obviously alters the SiNW band structure. However, this is not always negative since surface passivation may be considered a mechanism for electronic band engineering. Passivants which have been considered for the purpose of band engineering in SiNWs include the halogens,[90, 91, 92, 93] hydroxyls (OH)[93, 94, 95] and long-chained

organic functional groups.[20, 21, 88, 89] These atoms and chemical groups are typically electronegative. Moreover, surface passivation with organic functionalities such as CH_3 is often performed by substitution reactions on halogen or OH passivated SiNWs.[16, 17, 18, 19, 20, 21] In this process, it is common for steric effects and imperfections to prevent all surface halogens and OH groups from being substituted. Therefore, the end result is a SiNW which may have multiple surface passivants. Hence, it is crucial to be able to predict the effects which various such passivants may have.

Previously, first-principles calculations have indicated that electronegative surface passivants have a tendency to reduce the band gap of SiNWs by a few electronvolts in comparison to H-passivated SiNWs.[92, 93, 94, 95] According to Leu *et al.*., highly electronegative passivants such as iodine, bromine and chlorine cause the electronic state corresponding to the valence band maximum to acquire surface-like characteristics, which in turn prevents it from being drawn out of the band gap. The amount of surface-like character acquired depends on the strength of the Si-passivant bond, with weaker bonding resulting in a more a surface-like character and a smaller band gap.[92] Ng *et al.*. was also able to demonstrate that SiNW growth orientation plays a pivotal role in determining the amount of influence which an electronegative passivant may have. Ng *et al.* compared [100], [110], [111] and [112] SiNWs passivated separately with H, OH and F. They discovered that [110] SiNWs always experienced the largest band gap reduction upon switching from H to either OH or F passivation. On the other hand, [111] SiNWs were the least affected.[93] Nevertheless, there is a lack of a thorough explanation of the fundamental mechanisms behind how electronegative passivants affect states near the band edge. In this chapter, we tackle this issue by comparing and contrasting the electronic structure of hydrogen (H), fluorine (F) and methyl (CH_3) passivated [110] and [111] oriented SiNWs based on first-principles calculations. We will also show how electronic states in these SiNWs may be modelled by the strikingly simple infinite circular potential well.

3.2 Computational Details

All calculations are performed using the local density approximation (LDA) [64] within density functional theory (DFT) with projector augmented wave (PAW) pseudopotentials. These DFT calculations are performed using the Vienna *Ab-Initio* Simulation Package (VASP) [96, 97, 98, 99].[71, 72]

Periodic boundary conditions are used in all directions. The SiNWs continuously extend to infinity along the z direction. Within the xy plane though, we ensure that the simulation cells contain enough of a vacuum region such that there is a minimum separation of 7 Å between neighbouring SiNW images. This is sufficient to ensure that the interaction between images is insignificant.[100] The plane-wave energy cutoff is set to 400eV and we sample the Brillouin zone using a $1 \times 1 \times 8$ Monkhorst-Pack k-point mesh.

Electronic structure calculations are only performed on the SiNWs after they have been structurally optimised. We find the optimal lattice constant along the z direction for each SiNW by structurally relaxing it at various trial lattice constants and then plotting the total energy of the system against the corresponding trial lattice constants. We then fit each of these curves according to a quadratic relation in order to locate the optimal lattice constant which corresponds to the minimum point of the quadratic curve.

3.3 Silicon Nanowire Models

We use the bulk silicon model with a lattice constant of 5.431Å as the basis for constructing simulation models for our SiNWs. Silicon atoms from this bulk model having coordinates falling within predefined cross sections along the [110] and [111] directions are then extracted from the bulk model to form SiNW models of various sizes. This ensures that the Si atoms within each SiNW have the expected tetragonal geometry and a good initial guess for Si-Si bond length in order to speed up the geometric optimization process using DFT in VASP. Si atoms on the surface of each bare SiNW which lack either one or two nearest neighbours are then passivated with the appropriate number of H, F or CH_3 passivants. Si atoms lacking three nearest neighbours are themselves replaced by the desired passivant. The passivants are attached to the Si atoms so as to maintain the tetragonal geometry except on the

Table 1: Structural data and band gaps for [110] wire configurations. p refers to the passivant. d and a are the wire diameters and lattice constants along the SiNW axis respectively. All band gaps are direct.

[110] SiNWs				
p	Si:p ratio	d (nm)	a (Å)	Band gap (eV)
H	16:12	1.07	3.86	1.72
	24:16	1.25	3.87	1.60
	42:20	1.70	3.85	1.15
	54:24	1.87	3.86	1.11
	80:28	2.31	3.85	0.91
	110:32	2.76	3.85	0.81
	130:36	2.95	3.85	0.78
	168:40	3.36	3.85	0.73
F	16:12	1.08	3.89	1.03
	24:16	1.27	3.89	1.04
	42:20	1.72	3.87	0.80
	54:24	1.89	3.87	0.78
	80:28	2.33	3.86	0.71
	110:32	2.78	3.85	0.66
	130:36	2.97	3.86	0.64
	168:40	3.39	3.86	0.61
CH_3	16:12	1.20	4.17	0.89
	42:20	1.82	4.04	0.55
	80:28	2.44	4.00	0.22
	130:36	3.06	3.97	0.30

{100} facets of the [110] SiNWs, where Si atoms are bonded to two passivants. In order to prevent these passivants from being unphysically close, they are canted at 90° to each other. This starting 90° angle is allowed to change during geometric optimization which generally results in it increasing, as will be discussed in detail later. Our choice of initial structure is validated as the final energies of structures optimized using purely tetragonal bonding are significantly higher than the final energies resulting from our proposed initial structures. We show the typical [110] and [111] SiNWs before relaxation in Fig. 3. A summary of the structural data for SiNWs after geometric optimization is displayed in Tables 1 and 2.

3.3.1 The infinite circular potential well

Previous studies have shown that the electronic states of SiNWs may be modelled using simple potential well models.[102, 103] Here, we aim to demonstrate how the infinite circular

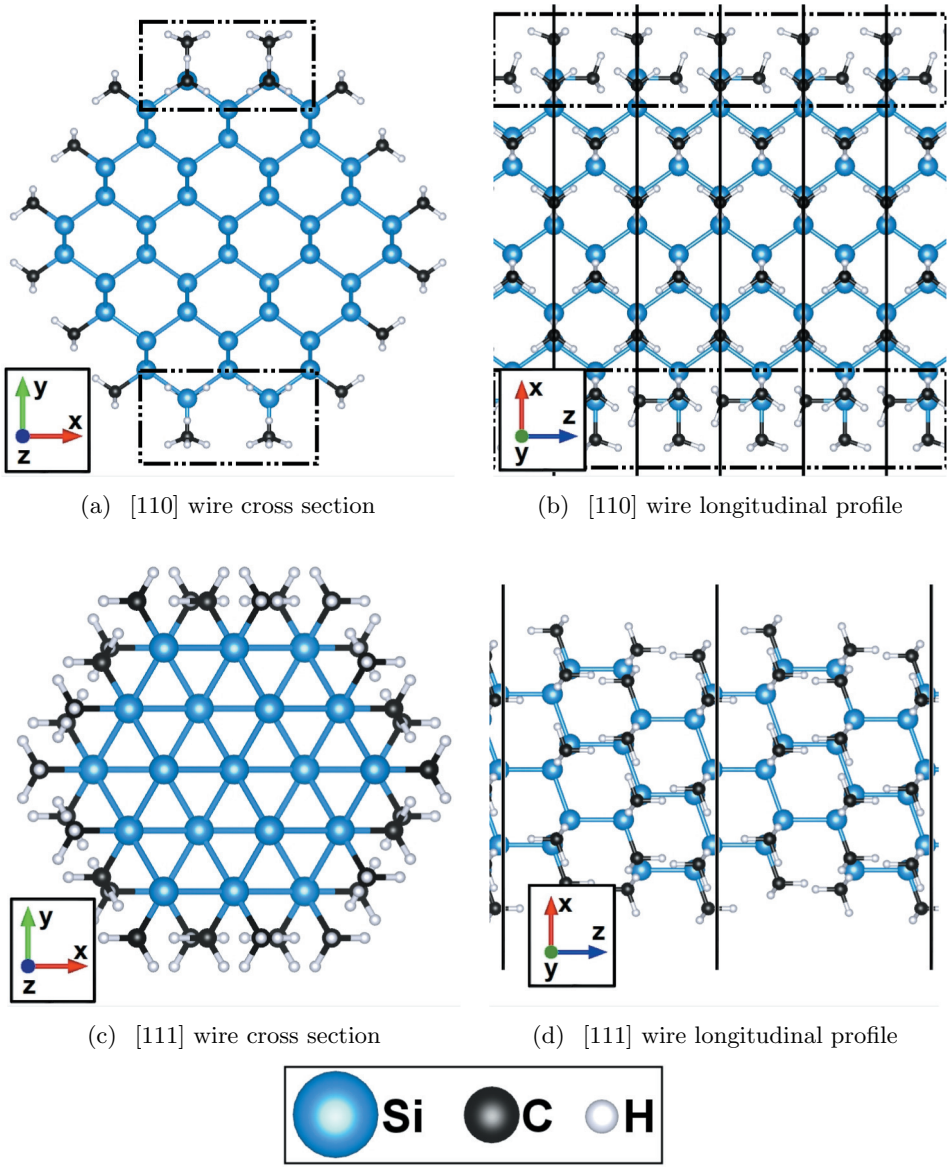

(a) [110] wire cross section

(b) [110] wire longitudinal profile

(c) [111] wire cross section

(d) [111] wire longitudinal profile

Figure 3: Cross sectional and longitudinal views of [110] and [111] oriented silicon nanowires passivated with CH_3 groups. Dotted lines show where canted Si-passivant bonds specifically occur on [110] wire surfaces. Solid lines demarcate unit cells along the axial direction in both cases. This figure along with 12 and 13 were illustrated using VESTA.[101]

Table 2: Structural data and band gaps for [111] wire configurations. p refers to the passivant. d and a are the wire diameters and lattice constants along the SiNW axis respectively. Indirect band gaps are indicated by *.

[111] SiNWs				
p	Si:p ratio	d (nm)	a (Å)	Band gap (eV)
H	38:30	1.06	9.36	2.11
	74:42	1.46	9.37	1.54
	122:54	1.86	9.37	1.21
	182:66	2.27	9.37	1.01*
F	38:30	1.07	9.36	1.61*
	74:42	1.47	9.37	1.50*
	122:54	1.87	9.37	1.23*
	182:66	2.27	9.37	1.08*
CH_3	38:30	1.23	9.75	2.03
	74:42	1.64	9.65	1.54
	122:54	2.04	9.58	1.21

potential well modified with a ring shaped potential dip can model the effect of electronegative surface passivants on the electronic states in SiNWs. The infinite circular potential well models which we consider for this purpose are depicted in Fig. 4. For a regular flat bottom infinite circular potential well, the analytic solution to Schrödinger's equation are Bessel functions. [104] However, only numerical solutions exist for the well modified with the ring-shaped potential dip. For the sake of consistency, we solve both Schrödinger's equation numerically in both systems. We do this using the fourth order Runge-Kutta method (RK4) [105, 106] as detailed in Appendix D. Our solutions give us the wavefunctions for the first few eigenstates from which we calculate their corresponding charge densities. In Fig. 5, we show the charge density profiles of these states. In the sections that follow, we will compare these charge density profiles with those from our SiNWs.

3.4 Effective Electronic Potential Under H, F and CH_3 Passivations

In this section, we consider how F and CH_3 surface passivations alter the effective electronic potential V_{eff} of SiNWs in comparison to H passivated SiNWs. V_{eff} here is defined as the sum of the ionic, Hartree and exchange-correlation potentials. Fig 6 shows the V_{eff} for typical H, F and CH_3 passivated [110] SiNWs. These are in the form of contour plots

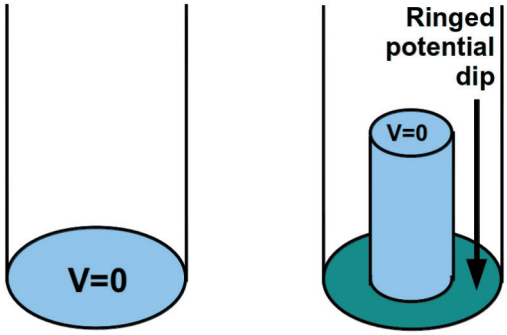

Figure 4: (a) Infinite circular potential well and (b) infinite circular potential well with a ring-shaped potential dip. Note that the core potentials in both wells have the same zero of energy.

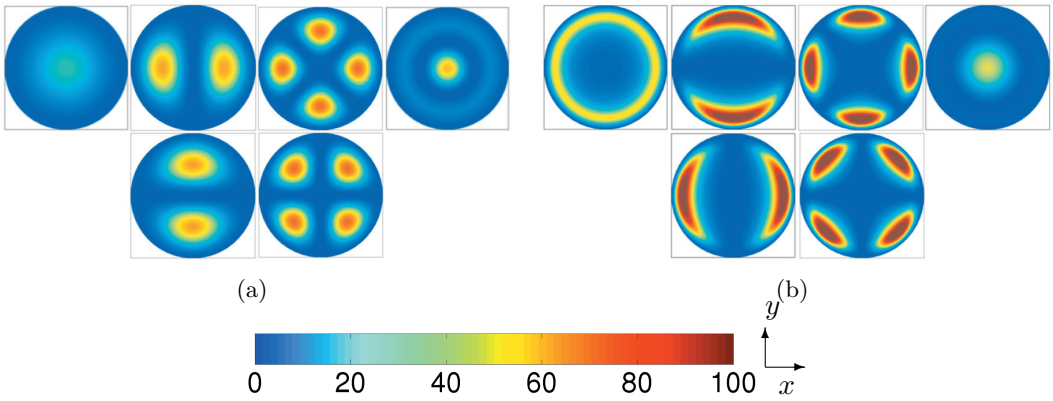

Figure 5: Normalized charge density profiles of the first six eigenstates in each of two types of infinite circular wells. (a) Flat bottom well. (b) Well with a ring-shaped potential dip.

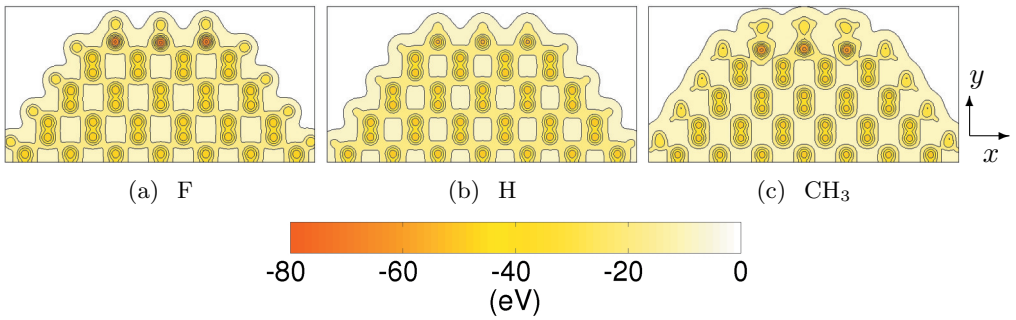

Figure 6: Contour plots of the effective potential over [110] SiNW cross sections. The effective potentials were averaged along the z direction of each unit cell. Each half is symmetric.

of V_{eff} averaged over the z direction within the unit cell. Throughout the cross sections of these [110] SiNWs, we notice a series of peaks and troughs in V_{eff}, with the troughs centered on the Si sites. Most notably, these troughs are significantly deeper on the Si sites located on the {100} facets for F and CH_3 passivated wires, with F passivation giving the greater increase in depth. From Fig. 3, it may be seen that it is along this {100} facet that Si atoms alternate with the surface passivants along the z direction. Thus, the canted structure of surface passivants along the {100} facet of [110] SiNWs brings a secondary layer of passivants closer to the SiNW surface and allows the surface potential to penetrate deeper into the [110] SiNW cross section.

In Fig. 7, we show the V_{eff} for typical H, F and CH_3 passivated [111] SiNWs. As with the [110] SiNWs, we see a series of peaks and troughs throughout each cross section again with the troughs located at Si sites. In contrast with the [110] SiNWs though, the average V_{eff} trough in [111] SiNWs is not as deep and there are none which are significantly deeper than average. Referring back to the nanowire configurations shown in Fig. 3, this is likely due to the more even spread of surface passivants along the [111] SiNW facets which allows for a more regular V_{eff}.

3.4.1 Surface dipole corrections

H, F and CH_3 are all more electronegative than Si. Therefore these surface passivations result in surface dipoles all around the [110] and [111] SiNW surfaces. This effect may be modelled with a cylindrical capacitor having oppositely charged inner and outer shells. In

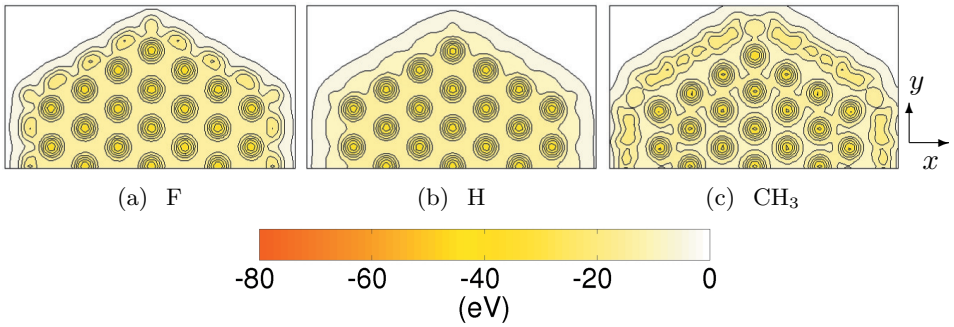

Figure 7: Contour plots of the effective potential over [111] SiNW cross sections. The effective potentials were averaged along the z direction of each unit cell. Each half is symmetric.

the case of the cylindrical capacitor, the potential of the outer shell is equal to the vacuum potential. However, there will be a potential offset between the inner and outer shells which is constant in the volume between them. This may be proven using basic principles of electrostatics. As such, we expect there to also be a potential offset between the inner core of the SiNW and the vacuum potential which depends on the electronegativity of the surface passivant. This must be taken into account when aligning the electronic band structure of differently passivated SiNWs. For this purpose, we choose the H passivated SiNW in each growth direction as the basis for comparison. Of course, the hexagonal geometry of the SiNWs may not result in a constant potential offset as in the case of the perfectly cylindrical capacitor model. Hence, we estimate an average potential offset Δ_{dipole} with respect to H-passivated wires using

$$\Delta_{dipole} = (\phi_{vac} - V_c)_{\{F/CH_3\}} - (\phi_{vac} - V_c)_{\{H\}}. \tag{143}$$

The quantity $(\phi_{vac} - V_c)_{\{passivant\}}$ provides an estimate of the strength of the surface dipole for a SiNW with a particular surface passivant. ϕ_{vac} is the vacuum potential and V_c is the mean of the average electrostatic potential of Si near to the center of the SiNW.[107, 108] The average electrostatic potential $\overline{V}$ of each Si at location $\vec{R}_{Si}$ is calculated using

$$\overline{V} = \int d\vec{r} \rho_{test} V_{eff}(\vec{r}) \rho(|\vec{r} - \vec{R}_{Si}|) \tag{144}$$

where ρ_{test} is the charge density of a test charge. For [110] and [111] SiNWs, we calculate the mean of $\overline{V}$ from Si atoms located within 5 Å and 4 Å radii of the respective SiNW cores

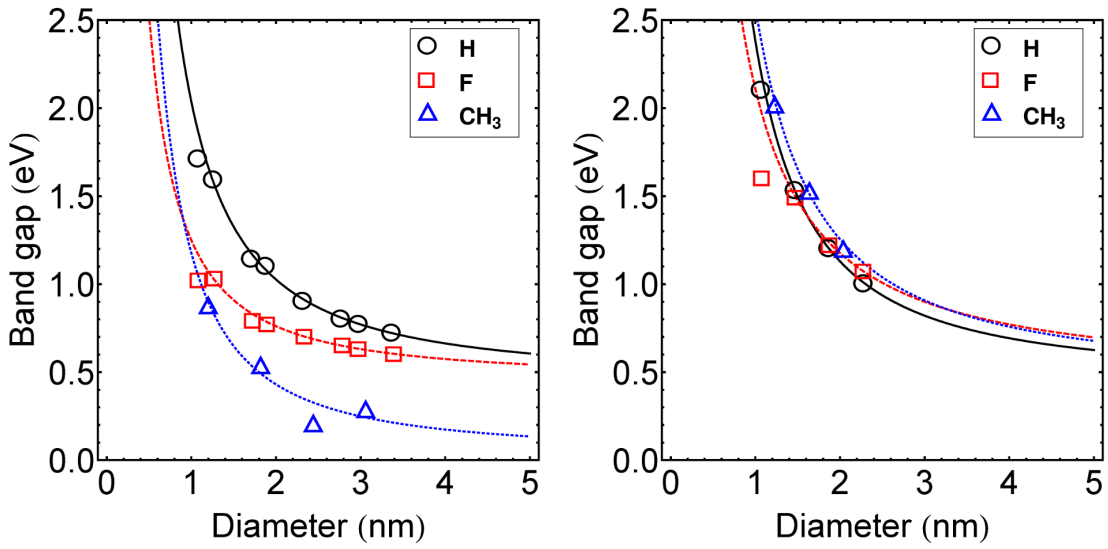

(a) [110] SiNWs (b) [111] SiNWs

Figure 8: Band gaps of H (◯), F (□) and CH_3 (△) passivated wires at various [111] and [110] wire diameters.

where the values of $\overline{V}$ are found to relatively similar to each other.

The procedure which we use for aligning the various electronic band structures is as follows. Initially, all band structures are aligned using the vacuum potential ϕ_{vac} as the reference zero of energy. In the next step, the electronic bands of F and CH_3-passivated SiNWs are further shifted by their respective Δ_{dipole} in order to negate the difference in dipole potential which they have relative to H-passivated SiNWs. With differences in dipole potentials accounted for in the electronic bands, we can then proceed to study how quantum confinement effects alter the band alignment.

3.4.2 Dependence of band gap on wire size, surface passivation and growth orientation

In Fig. 8, we show the diameter dependence of the band gaps of H, F and CH_3-passivated [110] and [111] SiNWs.

The data points shown in Fig. 8 are fitted using the relation

$$E_g = E_{g,bulk} + \frac{C}{d^{\alpha}}. \tag{145}$$

In Eq. 145, E_g is the band gap magnitude, d is the wire diameter, and C and α are fitting parameters. $E_{g,bulk}$ is the band gap of bulk Si. For consistency, we use the band gap of bulk

Table 3: Fitting parameters for the band gap versus diameter curves using (145). The first data point is excluded from the fit for each H and F-passivated SiNW.

	[110] SiNWs			[111] SiNWs		
	H	F	CH_3	H	F	CH_3
C	1.6	0.8	1.1	1.9	1.6	2.1
α	1.5	1.4	1.5	1.5	1.2	1.4

Si as calculated from VASP ($E_{g,bulk} = 0.46$ eV) instead of the true experimental band gap. We are able to achieve good fits for all the data using the above model in all cases except for the CH_3-passivated [110] SiNWs. We make use of standard curve fitting packages in *Mathematica* to achieve our fits. For this special case, we achieve a good fit only with an arbitrary value of $E_{g,bulk} = 0.04$ eV. The reason for this anomaly is due to significant strain in the CH_3-passivated [110] SiNWs. We elaborate on this in a later section.

145 is derived from the effective mass approximation for a particle in a box. In general, it relates the band gap reduction to increasing quantum confinement. In an ideal case, $\alpha = 2$.[100, 102] However, the cross sections of our model SiNWs are not perfectly square and so we expect discrepancies between our fitted α and the ideal $\alpha = 2$. This is especially true when considering small SiNWs with very high surface-area-to volume ratios. Therefore, we exclude the first data point ($d < 1.2$ nm) for H and F-passivated SiNWs in the curve fitting process. In Fig. 8, we see that the first data points in the F-passivated [110] and [111] SiNWs are particularly far off the trend. This is due to a combination of high surface-area-to volume ratio and the strong electronegative F surface potential which is consequently able to penetrate closer to the core of the small diameter SiNW.

Fig. 8 highlights two interesting issues. Firstly, it is clear that both F and CH_3 surface passivations strongly reduce the band gaps in [110] SiNWs, while the band gaps of [111] SiNWs are barely affected by the different forms of surface passivations considered in this study. Secondly, in the case of [110] SiNWs, CH_3 surface passivations are able to reduce the band gaps much more effectively than F surface passivations. The reason for this is not obvious considering that F is the more electronegative of the two types of passivants. In the sections that follow, we address these issues by performing detailed electronic structure analysis on the H, F and CH_3 passivated [110] and [111] SiNWs.

Table 4: Dipole potential offsets in F and CH_3 passivated [110] SiNWs measured with respect to H passivated [110] SiNWs. Si:p refers to the Si to passivant ratio.

[110] SiNWs		
	Si:p = 42:20	Si:p = 80:28
$\Delta_{dipole,F-H}$	1.82±0.05	1.77±0.03
Δ_{dipole,CH_3-H}	-0.88±0.05	-0.80±0.03

Table 5: Dipole potential offsets in F and CH_3 passivated [111] SiNWs measured with respect to H passivated [111] SiNWs. Si:p refers to the Si to passivant ratio.

[111] SiNWs		
	Si:p = 74:42	Si:p = 122:54
$\Delta_{dipole,F-H}$	1.9±0.2	2.0±0.2
Δ_{dipole,CH_3-H}	-0.8±0.3	-0.7±0.1

3.4.3 Electronic structure of [110] silicon nanowires

Fig. 9 displays the typical band structures of H, F and CH_3-passivated [110] SiNWs. They have been aligned using the procedure outlined in Section 3.4.1. We list the relevant dipole corrections used for this purpose in Tables 4 and 5.

In bulk Si, there exists six conduction band minima isosurfaces along the k_x, k_y and k_z directions and there is also a valence band minimum isosurface at the center of the Brillouin zone. Since two of the conduction band minima may be projected onto the origin of the axis along the [110] direction, we see that the band gap in the [110] SiNWs is always direct at the Γ point, regardless of surface passivation.[85]

In Fig. 9, we also see that the form and symmetry of F and H-passivated [110] SiNWs are relatively similar. However, F passivation does result in a sizeable upwards shift in the valence bands and this accounts for the band gap reduction observed for F-passivated SiNWs. As for CH_3 passivated SiNWs, we see that it is both conduction and valence bands closing in on each other which results in the much larger band gap reduction. It is clear though, that the shift in the conduction band states is around two times larger than the shift in the valence band states. We turn to an analysis of the charge density profiles of states close to the band gap at the Γ point for an explanation of our observations.

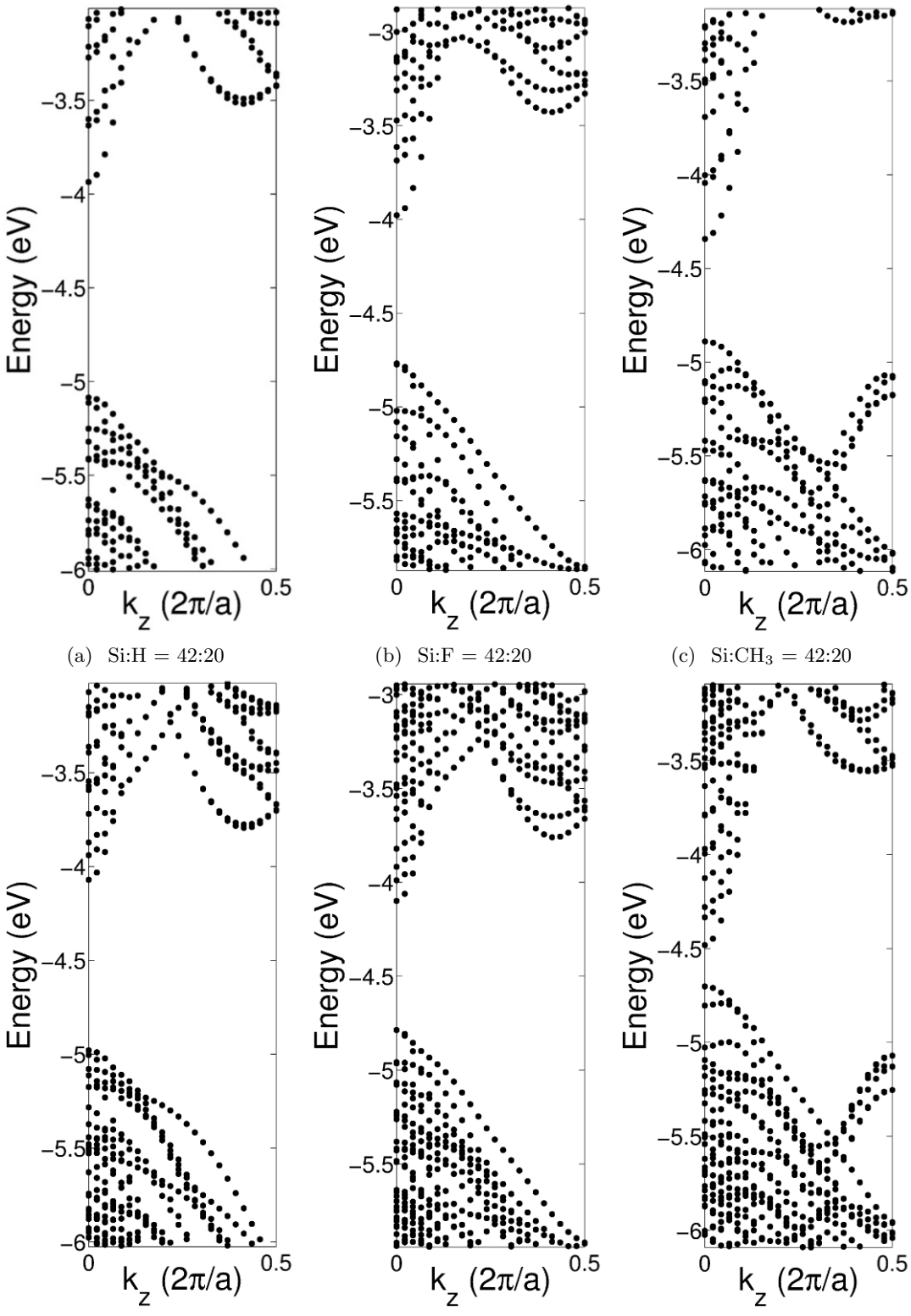

(a) Si:H = 42:20 (b) Si:F = 42:20 (c) Si:CH_3 = 42:20

(d) Si:H = 80:28 (e) Si:F = 80:28 (f) Si:CH_3 = 80:28

Figure 9: Electronic band structures of H, F and CH_3-passivated [110] silicon nanowires. Si to passivant ratios are indicated beneath each plot. The vacuum potential ϕ_{vac} is the zero energy reference point. Dipole corrections Δ_{dipole} in (143) have been applied to F and CH_3 SiNWs.

3.4.3.1 [110] Conduction band

We show in Fig. 10 charge density profiles for the bottom six conduction band states in each of the H, F and CH_3-passivated [110] wires. We find it most useful to analyze them in the form of contour plots averaged along the z direction. They can be seen to be very similar to each other in terms of symmetry and ordering.[1]. In fact, the larger the diameters of the SiNWs, the more similar their charges states become under different surface passivations.

We gain a number of insights when comparing the charge density profiles of these conduction band states in Fig. 10 together with those of the infinite circular potential well shown earlier in Fig. 5(a). In all cases, we see that the lowest energy state is s-like with the charge concentrated at the core of the system. Going up in energy, we see two and then four distinct regions where charge is concentrated. Above these, we see states where there is a primary region of high charge density at the core and a secondary region near the edges. These strong similarities prove that the confining potential for conduction band states is not strongly affected by changes in the potential due to different surface passivations. Fig. 6, show that the different surface passivations do not greatly affect the form of the potential in the interior of [110] SiNWs. Therefore, we conclude that conduction band states of [110] SiNWs are strongly localized close to the core.

Comparing the conduction band profiles in Fig. 10, we also notice that the charge density profiles for CH_3-passivated SiNWs are slightly more elongated along the y axis than those of the F and H-passivated SiNWs. This is unlikely due to the change in surface potential induced by the CH_3 groups since CH_3 is far less electronegative and inert than F. Instead, we may attribute this effect to mechanical strain. We note from Table 1 that CH_3 passivated SiNWs have much larger lattice constants along the z direction than the H and F passivated SiNWs. This results in greater charge spread longitudinally in CH_3 passivated SiNWs which in turn causes the perceived redistribution of charge in xy plane. Moreover, this large amount of charge spread in CH_3 passivated [110] SiNWs due to strain greatly lowers the energy levels of their conduction band states which contributes to the band gap

[1]The energy difference between the fifth and sixth conduction band states of the CH_3-passivated wire is only about 0.01 eV.

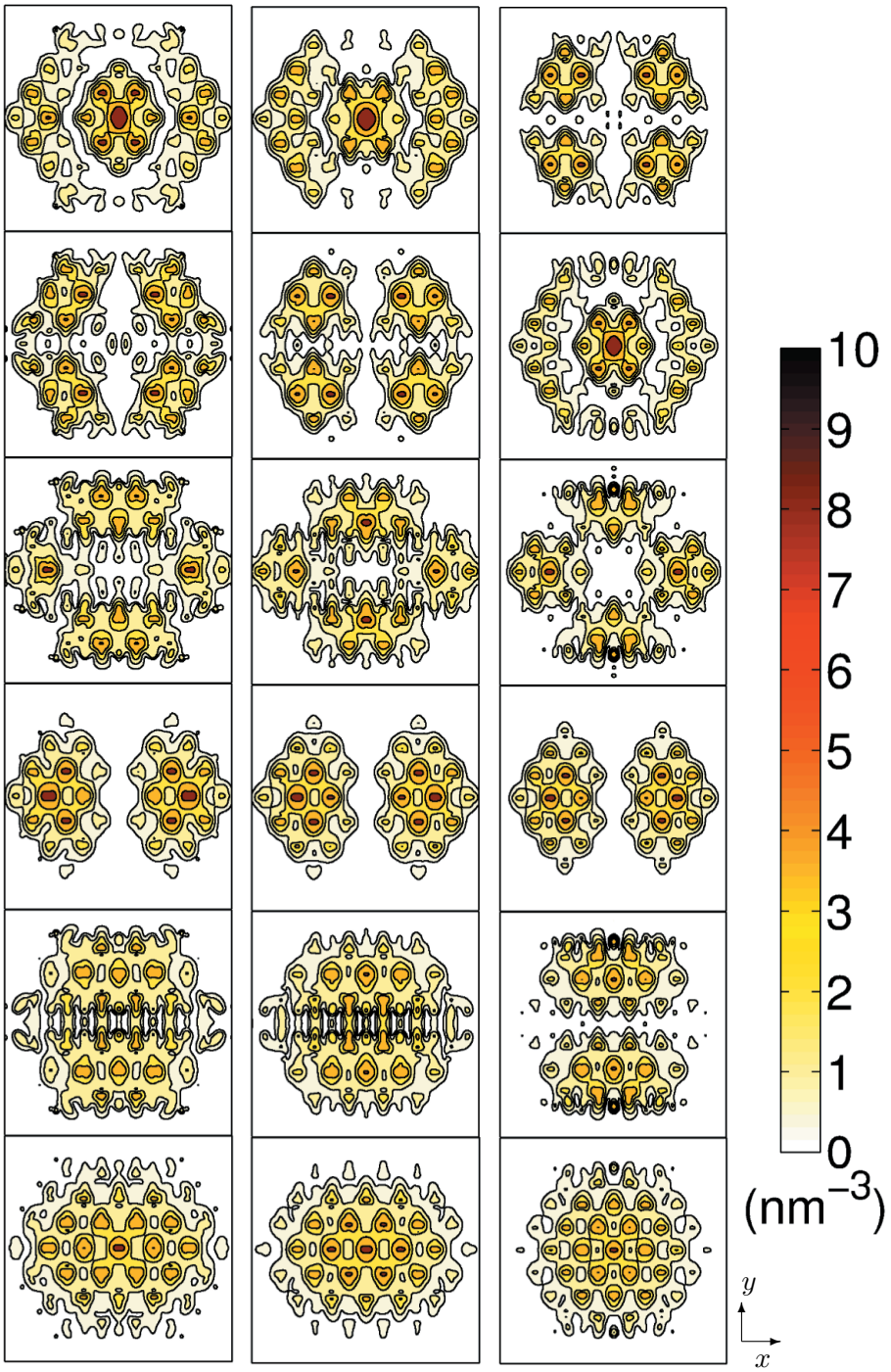

(a) F (b) H (c) CH_3

Figure 10: Contour plots of the cross sectional charge density profiles for the bottom six states of the conduction band in each [110] wire with different passivants. Charge densities are averaged over the z direction. The Si:passivant ratio is 80:28 in each case. The conduction minima are at the bottom.

reduction.

3.4.3.2 [110] Valence band

Fig. 11 shows the valence band charge density profiles of H, F and CH_3 passivated [110] SiNWs. Again, we represent these using contour plots averaged over the z direction. The charge density profiles shown here generally bear less resemblance to those of the infinite circular potential well. Nevertheless, there are still some interesting similarities. Consider first the charge density profile of the valence band maximum state of the H-passivated [110] SiNW. It is clearly s-like and therefore similar in nature to the ground state charge density profile of the infinite circular potential well. Also, the next nodal state (fourth from the top) is similar to the sixth eigenstate of the infinite circular potential well. Both of them have a primary region of high charge density at the core and a secondary region close to the edges.

We turn now to examining how switching from H to F-passivation changes the valence band electronic structure. We specifically compare the valence maxima and next nodal states of these two types of wires. For greater clarity, we show these states in the form of 3D isosurface plots in Fig. 12. With F passivation, the valence maximum state of the original H-passivated [110] SiNW changes from being s-like to having charge concentrated mainly around the {112} facets, leaving a minimum at the core. This is exactly what happens in the case of the infinite circular potential well ground state after the ring shaped potential dip is introduced as seen in Fig. 5. As for the next nodal state, we see that the central charge region in the H-passivated [110] SiNW becomes larger while the side regions decrease in size. Again, this change is similar to what happens to the sixth eigenstate in the infinite circular potential well upon modification with the potential dip. These observations indicate that valence band states of F-passivated [110] SiNWs are experiencing an exceptionally strong potential dip close to the wire edges. Recall that this is indeed the case as seen from the effective potential contour plots of F-passivated [110] SiNWs in Fig. 6. However, the potential drop as seen from Fig. 6 is concentrated only at the {100} facets. As valence band states may be thought of excited hole states, the charge distribution are preferentially

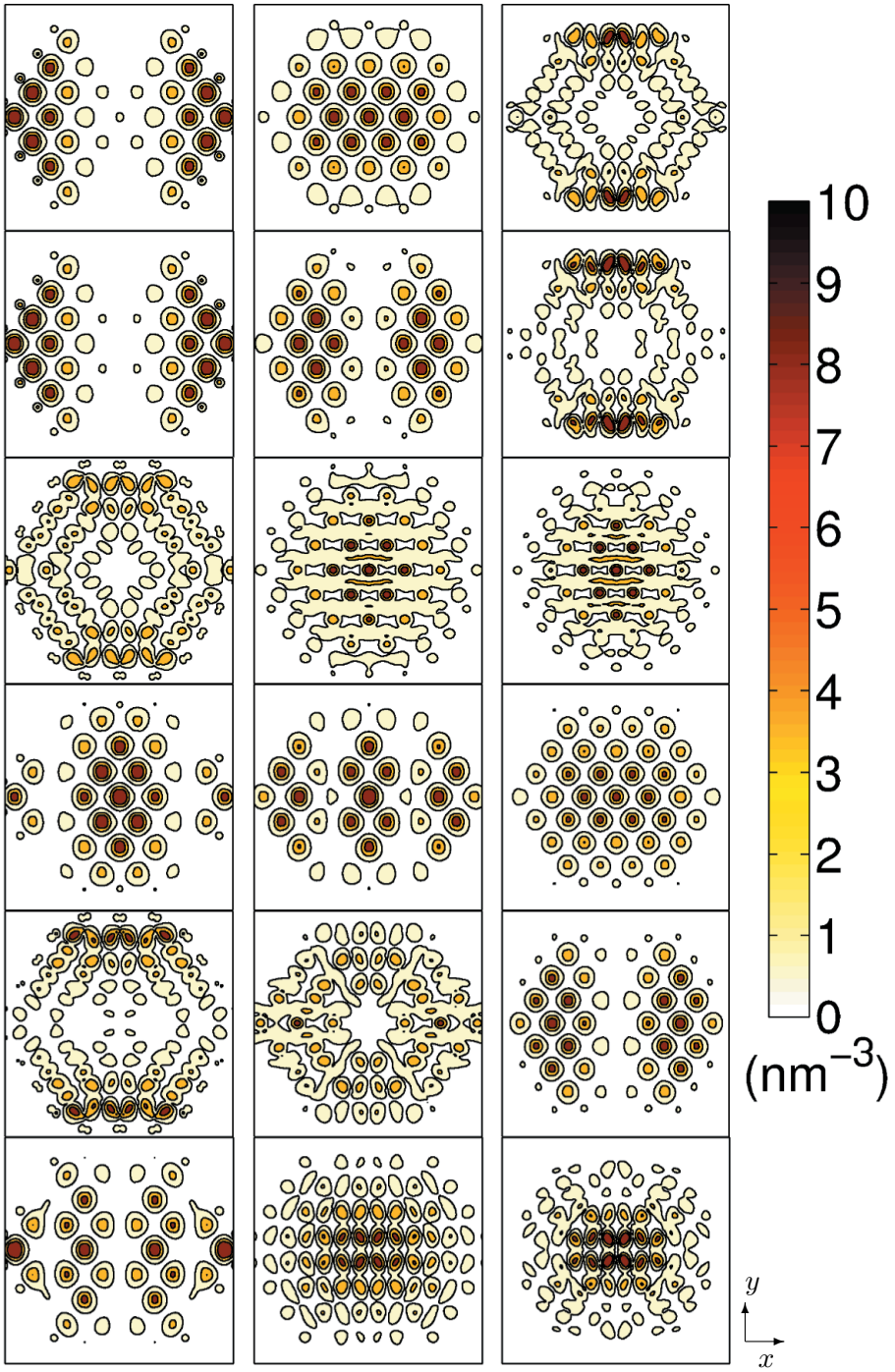

(a) F (b) H (c) CH_3

Figure 11: Contour plots of the cross sectional charge density profiles for the top six states of the valence band in each [110] wire with different passivants. Charge densities are averaged over the z direction. The Si:passivant ratio is 80:28 in each case. The valence maxima are at the top.

pulled closer to the {112} side facets. Moreover, this results in the charge distribution being more spread out or less quantum confined, such that the hole energy states shift upwards in energy and shrink the band gap.

Comparing the charge density profiles of CH_3 and H-passivated [110] SiNWs in Fig. 11, we see that the ordering of the states has been changed. Yet, the form of the charge density profiles remain relatively similar, which indicates that valence band states in CH_3 and H-passivated [110] SiNWs experience a similar surface potential. The top two valence states in CH_3-passivated [110] SiNW are equivalent to the fifth and eighth (not shown) valence states of the H-passivated [110] SiNW. The main difference in form is due to the CH_3-passivated wire having more charge concentrated on the {100} facets. As alluded to earlier, this can be explained by mechanical strain effects, specifically along the z axis and also locally on the {100} facets. Fig. 13 illustrates this concept. Axial strain in the z direction stretches the bond angle between Si1, Si3 and Si2 and other similar groups of Si atoms. However, there is an almost right angle between atoms C1, Si4 and C2 and similar atomic groupings on the {100} facet due to the tight packing of CH_3 groups. This is also true for bond angles between Si4, C1 and any H attached to C1. Thus, the strong distortion of tetrahedral bonding in these cases causes charge to be redistributed to regions similar to that between Si3 and Si4, which are least affected by strain and typically lie within the xy plane of the {100} facets. In comparison, the H-Si-H and F-Si-H bond angles along {100} facets are respectively found to be 105° and 97°. This is why the third and fifth states from the top of the F-passivated valence band have appearances which are intermediate between the top two states in the CH_3-passivated SiNW and the corresponding states in the H-passivated SiNW.

From Table 1, we see that CH_3-passivated SiNWs have lattice constants which are between 3% and 8% longer than the lattice constants of comparable H passivated SiNWs. This is accompanied by a sizeable band gap reduction of between 0.3 eV to 0.48 eV. The strained lattice constant in CH_3-passivated SiNWs explains the predicted 0.04eV band gap of bulk Si from fitting the Eq. 145 using CH_3-passivated SiNW data. Again using LDA calculations in VASP, we calculate the band gap of bulk Si, which has been uniaxially

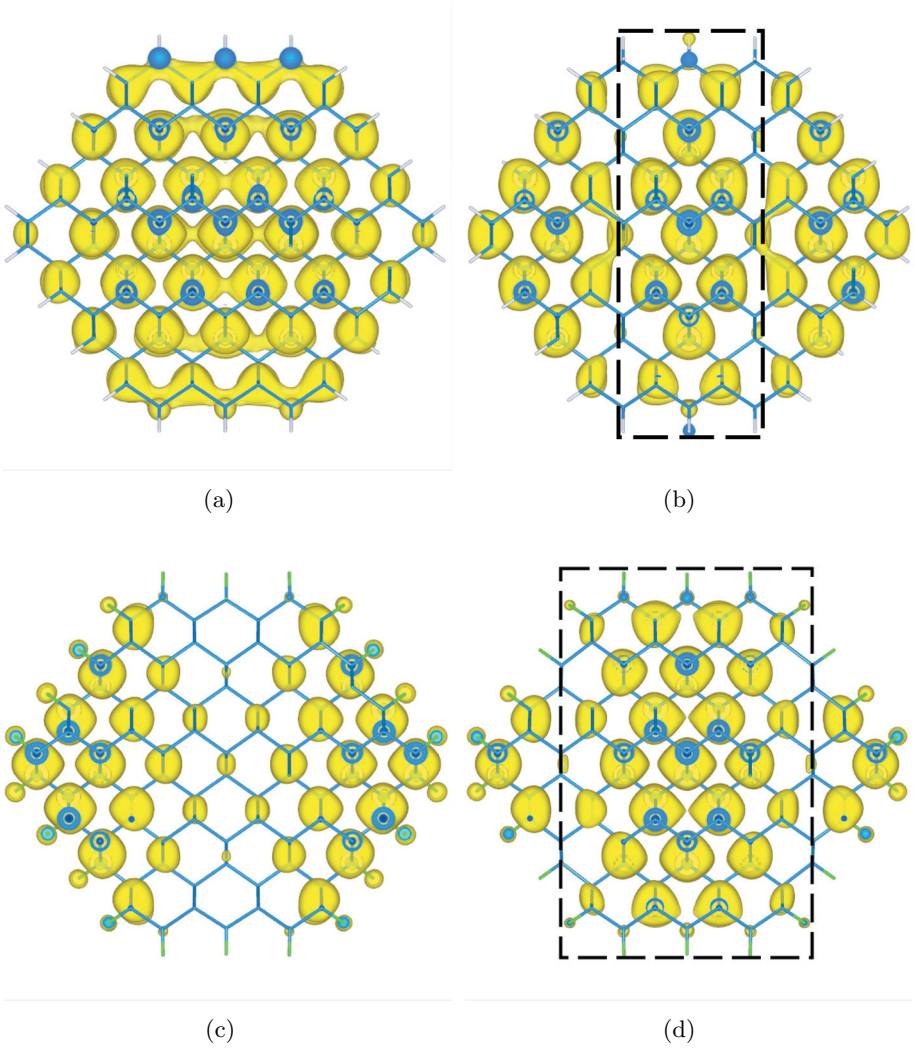

Figure 12: (a) and (b) are the 3D charge density profiles of the valence band maximum and next nodal state of the H-passivated [110] SiNW respectively. (c) and (d) are the charge density profiles of the valence band maximum and next nodal state of the F-passivated [110] SiNW respectively. All profiles here are taken at the same isosurface level. The Si:passivant ratio is 80:28 in each case.

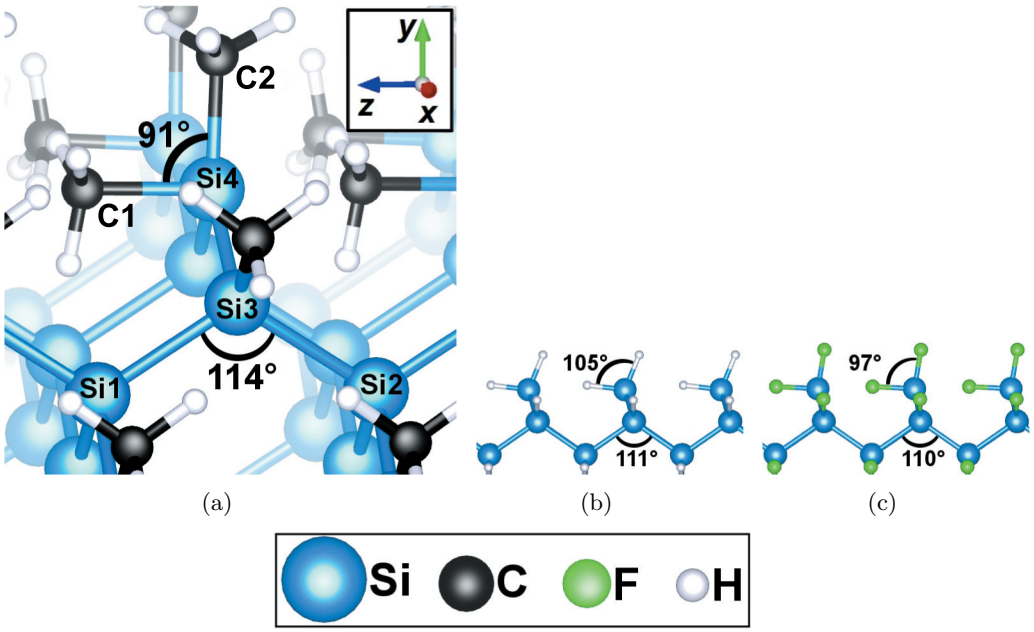

Figure 13: (a) Close up view of a portion of the {100} facet on a CH_3-passivated [110] SiNW. (b) and (c) show canted Si to passivant bonds on the {100} facet of H and F-passivated [110] SiNWs respectively. All structures have been relaxed.

strained by 5%, to be 0.11 eV. This band gap even vanishes at 10% strain. Thus we see that mechanical strain is a mechanism by which band gaps can be reduced in both bulk and low-dimensional systems. This phenomenon has been studied in detail elsewhere by Leu *et al.* [108] and Wu *et al.* [109]. Leu *et al.* reported that in the case of H-passivated [110] SiNWs, every 1% of either tensile or compressive strain corresponds to a band gap reduction of about 0.1 eV. Even though these calculations performed by Leu *et al.* made use of the generalized gradient approximation (GGA) instead of the LDA which we have use so far in this study, we still expect the general conclusions to agree in both cases. To support this point, we perform additional calculations using the GGA on our H-passivated SiNW sample which has 80 Si atoms per unit cell. Our original LDA calculations resulted in an optimized lattice constant of 3.85 Å and a band gap of 0.91 eV for this particular SiNW. The band gap was reduced to 0.38 eV when the lattice constant was increased by 5%. Repeating the same calculational procedures but with the GGA led to a slightly larger lattice constant of 3.89 Å and band gap of 1.09 eV. This band gap was similarly reduced to a value of 0.6 eV with the same 5 % strain. While the GGA predicts a band gap which is larger by about 0.2

eV in comparison to the LDA method, we see the a similar 0.5 eV band gap reduction in both instances when 5 % strain is introduced. From this analysis, we find that our results are comparable with those of Leu *et al.* which lend support to our case that large CH_3 passivants introduce strain as opposed to larger changes in the surface potential, in order to reduce the band gaps in [110] SiNWs. We may attribute differences between our study and that of Leu *et al.* to geometrical differences between CH_3 and H-passivated SiNWs, which results in the CH_3-passivated [110] SiNWs experiencing additional strain localized on their {100} facets.

Along with the band gap reduction due to mechanical strain in H-passivated [110] SiNWs, the works of Leu *et al.* and Wu *grossman* also both predict a direct to indirect gap transition. This occurs as a result of valence bands away from the Γ point shifting above the original valence band maxima. We do not observed this direct to indirect band gap transition in CH_3-passivated SiNWs despite the comparable levels of strain which the CH_3 groups induce. These observations highlight the possibility of using large surface passivants to introduce axial strain in order to adjust the band gap magnitude, while simultaneously causing localized strain on certain SiNW facets to readjust the band curvature so as to maintain a direct band gap. This effect has important technological applications where SiNWs are involved in areas such as photovoltaics and sensors [17, 18, 20, 21, 88, 89], especially where long-chain organic groups are attached to the SiNW and high optical sensitivity is critical.

3.5 Electronic Structure of [111] Silicon Nanowires

The electronic band structures for H , F and CH_3-passivated [111] SiNWs are illustrated in Fig. 14. In general, the band gap of [111] SiNWs is not expected to be direct. This is because the conduction band minima do not project onto the [111] axis. In the conduction bands, we see that the major effect of surface F is to cause the conduction minimum to shift away from the Γ point. Surface CH_3 though causes greater upward curvature in the conduction bands close to the band edge. Overall, the conduction bands are relatively flat and F and CH_3 passivations do not significantly change the position of the conduction

band minimum. In the valence bands, we see that both F and CH_3 passivations cause an upwards shift of bands below the valence maximum but these do not end up shifting above the valence maximum. Since the valence maximum and conduction minimum remain relatively unaffected by F and CH_3 passivations, the band gap magnitude of [111] SiNWs is not affected by these two surface passivations.

Analyzing charge density profiles of [111] SiNWs shown in Figs. 15 and 16, we see that although there are slight ordering differences between the states, F and CH_3 passivations do little to alter the charge distributions in both valence and conduction band states. This implies that conduction and valence band states in [111] SiNWs under H, F and CH_3 passivations experience a similar confining potential.

The reasons why F and CH_3 passivations do not strongly alter the electronic states of [111] SiNWs can be obtained via structural considerations. From Fig. 3, we see that the surface passivants in [111] SiNWs are more evenly spread out than those in [110] SiNWs where the passivants are more neatly aligned in rows along the z direction. Furthermore, there are two rows of passivants on the {100} facet of the [110] SiNWs. Therefore, the surface potential, particularly due to highly electronegative surface passivants like F, is able to penetrate much deeper into the interior of [110] SiNWs and affect the electronic states. In addition, the structure of [111] SiNWs does not allow for the type of tight packing of surface passivants and loss of tetragonal bonding geometry as seen on the {100} facet of [110] SiNWs. This prevents localized strain from building up on certain facets of [111] SiNWs as is the case in the [110] SiNWs. Finally, we see that along the z axis of [111] SiNWs unit cells, there are six Si-Si bond linkages, three of which are parallel to the z axis. In contrast, there are only two Si-Si bond linkages along the length of the unit cell for [110] SiNWs, both of which are not parallel to the z axis. Hence, axial strain is always more effectively distributed over the Si-Si bond linkages in [111] SiNWs than in [110] SiNWs, such that charge states in [111] SiNWs experience less distortion along the z direction.

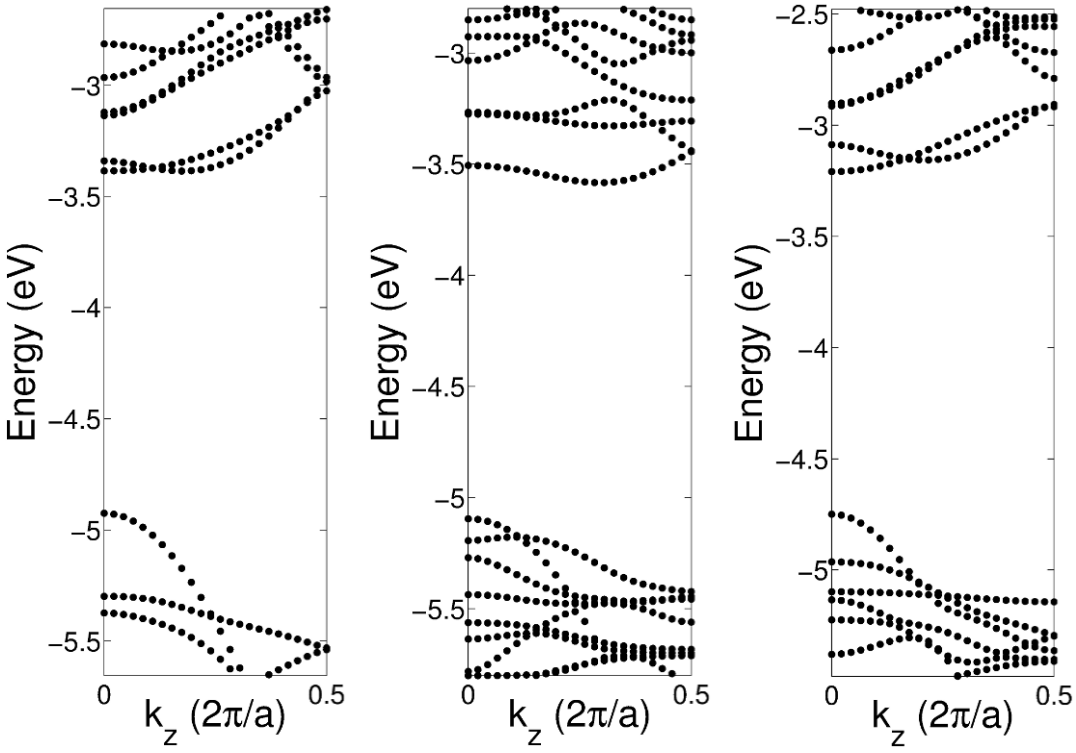

(a) Si:H = 74:42 (b) Si:F = 74:42 (c) Si:CH_3 = 74:42

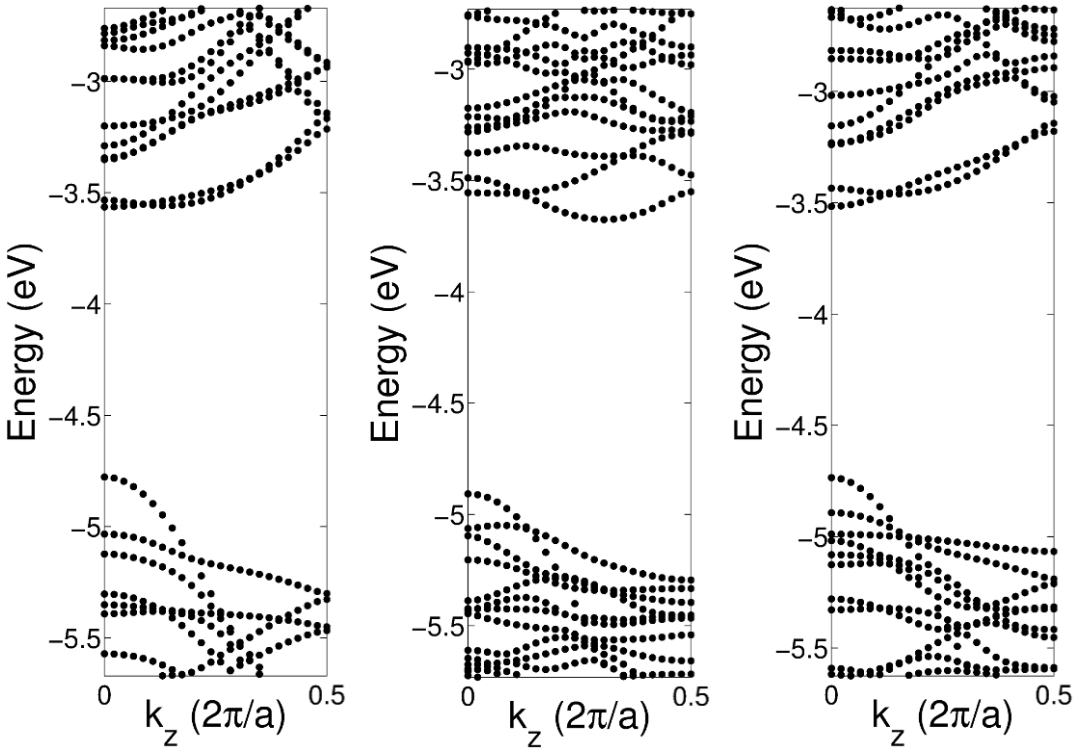

(d) Si:H=122:54 (e) Si:F = 122:54 (f) Si:CH_3=122:54

Figure 14: Electronic band structures of H, F and CH_3-passivated [111] silicon nanowires. Si to passivant ratios are indicated beneath each plot. The vacuum potential ϕ_{vac} is the zero energy reference point. Dipole corrections Δ_{dipole} in (143) have been applied to F and CH_3 SiNWs.

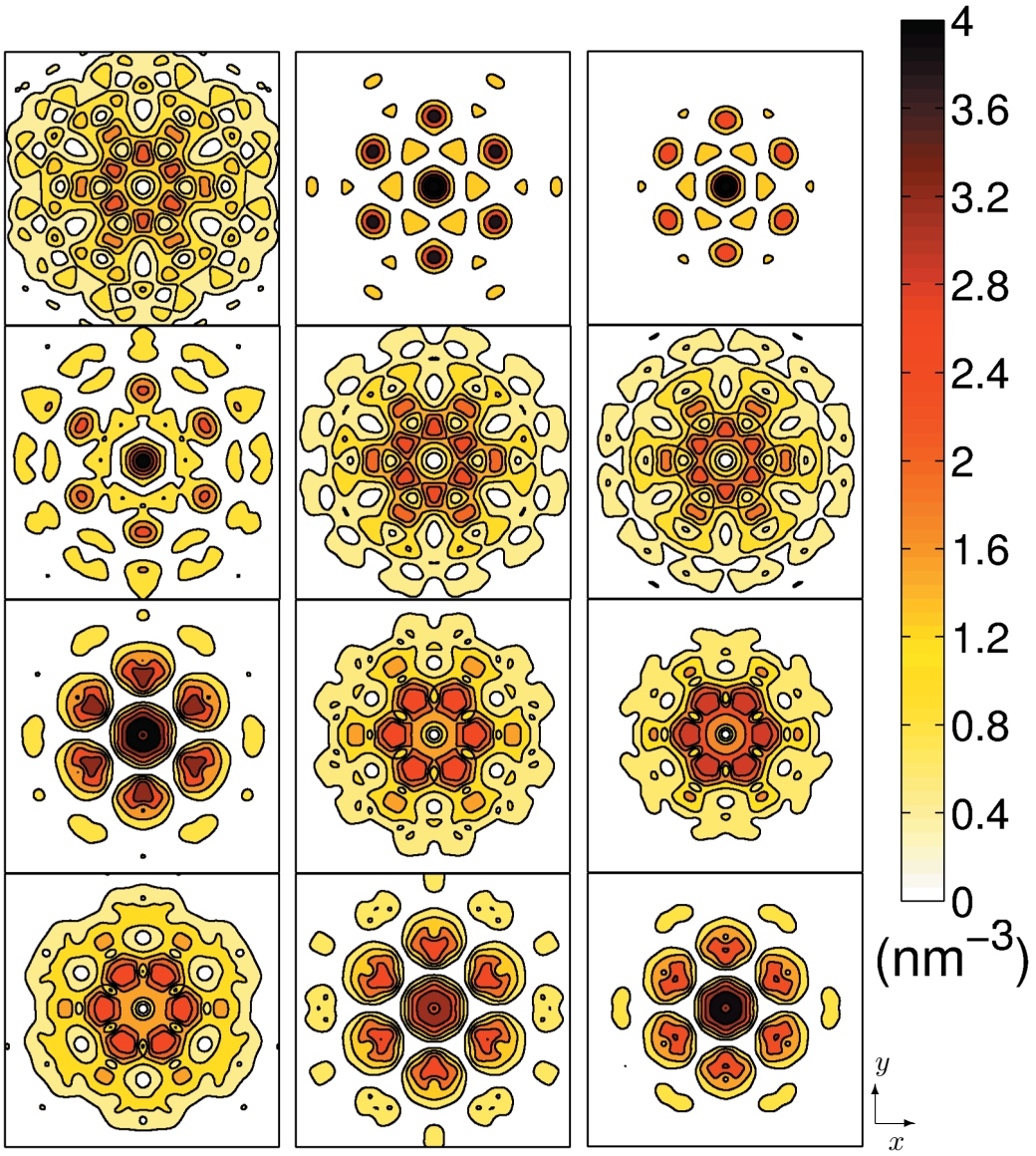

(a) F (b) H (c) CH_3

Figure 15: Contour plots of the cross sectional charge density profiles for the bottom six (degeneracies not shown) states of the conduction band in each [111] wire with different passivants. Charge densities are averaged over the z direction. The Si:passivant ratio is 122:54 in each case. The conduction band minima are at the bottom.

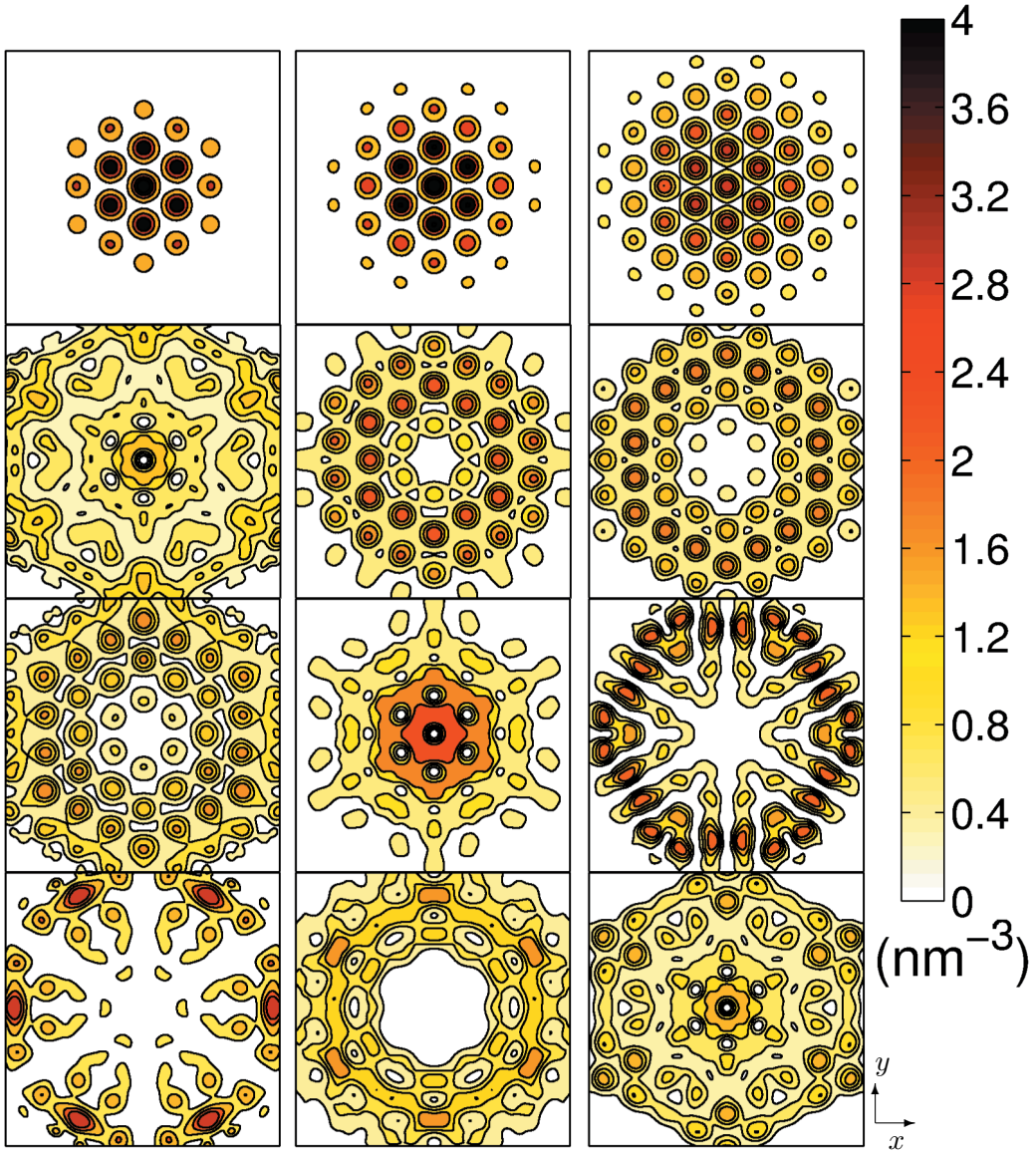

(a) F (b) H (c) CH_3

Figure 16: Contour plots of the cross sectional charge density profiles for the top six (degeneracies not shown) states of the valence band in each [111] wire with different passivants. Charge densities are averaged over the z direction. The Si:passivant ratio is 122:54 in each case. The valence band maxima are at the top.

3.6 Summary

Using first-principles calculations, we have investigated how F and CH_3 surface passivations affect the electronic structure of [110] and [111] oriented SiNWs, using their H passivated counterparts as a basis for comparison. Common to both [110] and [111] oriented SiNWs was that a reduction in diameter always caused a band gap increase, regardless of surface passivation. This effect could be readily explained and modelled by considering how a diameter reduction naturally corresponded to an increase in quantum confinement and vice-versa.

In [110] SiNWs, it was found that F and CH_3 surface passivations always resulted in considerable band gap reductions. However, this effect was achieved by very different fundamental mechanisms in both cases. Surface F, with high electronegativity, caused the band gap reduction by strongly altering the electron potential close to the {100} facets of the [110] SiNWs, which in turn changed the quantum confinement of the electronic states. Specifically, electronic states just under the valence maxima became more distributed closer towards the {100} facets and hence less confined, such that they moved upwards in energy to reduce the band gap in F passivated wires. CH_3 groups were found to be relatively inert as they did little to alter the confining electronic potentials in [110] SiNWs. Instead, their relatively large size caused longitudinal strain of up to almost 10% which resulted in significant charge spread axially. Close packing of the bulky CH_3 groups on the {100} facets also caused additional bond distortion and charge redistribution locally on those facets. All in all, quantum confinement of electronic states is reduced more strongly by strain introduced by large CH_3 groups, than it is by the drop in confining potential near the wire surface due to highly electronegative F passivation

In [111] SiNWs, F and CH_3 surface passivations had little effect on the electronic structure. Electronic band structures, charge densities and band structures were all relatively similar for F, CH_3 and H passivated [111] SiNWs of the same diameter. The reason for this was that the structure of [111] SiNWs permitted surface passivants to be more evenly spread on their facets. This prevented strain from building up locally on the facets and also hindered the surface potential from penetrating too much into the interior of the wires.

Longitudinal strain was also further mitigated by the longer [111] SiNW lattice constants and the fact that there were more Si-Si bonds parallel to the wire axis which allowed for a more effective and even distribution of strain amongst the various Si-Si bonds.

Throughout our study, we also demonstrated that electronic states close to the band edges of F, H and CH_3-passivated [110] and [111] SiNWs could be modelled well by the infinite circular potential well. We also proposed a method for calculating the potential offset between SiNWs having different surface dipole potentials due to surface passivations of varying electronegativity.[110]

CHAPTER IV

ELECTRONIC AND THERMOELECTRIC PROPERTIES OF COPPER SULFIDE AND COPPER SELENIDE

4.1 Introduction

The high temperature phases of *p*-type copper sulfide (Cu_2S) and copper selenide (Cu_2Se) have recently been demonstrated by experiment to possess very high thermoelectric efficiencies. The ZT values of Cu_2S and Cu_2Se are 1.7 and 1.5 respectively. This, combined with their non-toxic nature, makes them highly competitive with other leading thermoelectric materials such as PbTe and SiGe alloys which happen to be far more expensive.[36, 38] On top of this, Cu_2S and Cu_2Se have potential applications as photovoltaic materials [22, 23, 24, 25, 26, 27, 28, 29] and in the development of lithium ion batteries.[28, 30, 31, 32, 33, 34]

The high temperature phases of Cu_2S and Cu_2Se are most interesting. S or Se atoms form an ordered crystalline sublattice but Cu atoms are disordered. Currently, there is still much uncertainty over the structure of these materials arising from the Cu disorder. This presents a problem in calculating their electronic and thermoelectric properties since there are no reliable structural models to begin with. Most first-principles studies rely on the antifluorite structure of Cu_2S and Cu_2Se to make predictions. A major issue with this is the lack of band gap in most of these calculations as a result of using a purely fictitious antifluorite structure.[56, 111, 112]

A number of first-principles electronic structural analyses have previously been performed on Cu_2S [29, 56, 111] and Cu_2Se [111, 112, 113] by various groups. Rasander *et al.*, Lukashev *et al.* and Tyagi *et al.* have analyzed the electronic structure of the unphysical but nevertheless insightful ordered antifluorite structure of cubic Cu_2S and Cu_2Se. In this antifluorite structure, all the Cu atoms are fixed in the $8c$ tetrahedral sites and S or Se atoms occupy FCC sites. This is different from the actual disordered cubic phases of Cu_2S

and Cu_2Se at high temperature where in reality, the Cu atoms are disordered and occupy the 8*c* sites and also other nearby sites according to a certain probability distribution. Typical DFT calculations on the antifluorite form of Cu_2S and Cu_2Se lead to band structures which have no gap unless an on-site Coulomb interaction (+U) [114] is included or hybrid functionals are used.[111, 112] Only the works of Lukashev *et al.* and Xu *et al.* attempt to address the effect of Cu disorder in the high temperature phases of Cu_2S. Most notably, the Cu disorder opens up a band gap.[29, 56]

Based on first-principles electronic structure calculations on antifluorite Cu_2Se, Tyagi *et al.* proceeded to calculate the thermolectric properties of Cu_2Se. Despite not accounting for Cu disorder, good agreement was found between their theoretical predicted Seebeck coefficients and the experimentally observed Seebeck coefficient.[38, 113]

Evidently, there are a number of shortcomings in previous theoretical and computational studies on Cu_2S and Cu_2Se. They either lack a good structural model for Cu_2S or Cu_2Se which incorporates realistic Cu disorder to begin with or they fail to provide sufficient details concerning the electronic structure and thermoelectric properties of these materials. As mentioned, the thermoelectric properties of Cu_2S and Cu_2Se are of immense interest due to recent experimental results which show that Cu_2S and Cu_2Se are currently amongst the most efficient thermoelectric materials in the world. We seek to address these issues in this chapter by providing a comprehensive study on the electronic and thermoelectric properties of Cu_2S and Cu_2Se with the inclusion of realistic Cu disorder. We begin by elaborating on a first-principles random structure search method to find energetically stable structures of high temperature Cu_2S and Cu_2Se which include the vital Cu disorder. We then discuss the electronic structure of the most energetically stable structures found for Cu_2S and Cu_2Se and proceed to evaluate their thermoelectric properties using Boltzmann transport theory. In particular, we calculate their Seebeck coefficients, electrical conductivities and power factors as a function of hole concentration. These three quantities represent purely electronic contributions to ZT.

4.2 Phases of Copper Sulphide and Copper Selenide

Copper sulfide and copper selenide may exist in various phases depending on temperature and percentage composition of Cu. This results in both materials having very complicated phase diagrams which we show in Appendix E. We focus here on Cu_2S and Cu_2Se and give a brief overview of their main phases below.

Cu_2S with small amounts of Cu deficiencies, has three important primary phases which we label below as α, β and γ.

1. α-Cu_2S

   The α phase represents the most stable low temperature phase of Cu_2S and it is also widely known as low chalcocite which is an important ore from which Cu is harvested. α-Cu_2S, which exists at temperatures ranging from room temperature to around 380K, has an ordered monoclinic structure with Cu and S atoms in fixed positions. The primitive unit cell of α-Cu_2S is very big with a complicated arrangement of 96 Cu atoms and 48 S atoms. The most notable feature in the structure of α-Cu_2S is its layered structure. Each layer consists of a roughly hexagonal arrangement of S atoms. Cu atoms both within and between layers are trigonally bonded with 3 other S neighbours.[52, 115]

2. β-Cu_2S

   The β phase of Cu_2S, existing at temperatures between 380K and 700K, is similar to its α phase as it too retains a layered structure. The S atoms are arranged in a distinct hexagonal close-packed lattice but the Cu atoms are completely disordered within and between the hexagonal S layers. As seen from the copper sulphide phase diagram in Appendix E, the phase field of *beta*-Cu_2S is particularly narrow.[43, 52, 54, 56, 116]

3. γ-Cu_2S

   Beyond 700K, the layered structure of Cu_2S disappears as it transitions into the γ phase. The S atoms remain ordered but in a face centered cubic (FCC) lattice while the Cu atoms are disordered between them.[53] This γ phase of Cu_2S is of particular interest as a high temperature thermoelectric material which is designed to function

at temperatures of around 1000K. The γ phase of Cu_2S has a relatively large phase field which makes it easier to access than the the β phase.[36, 38]

$Cu_{2-x}Se$ has only two major phases. Unlike $Cu_{2-x}S$, it does not possess an intermediate phase with a hexagonal arrangement of Se atoms.

1. α-Cu_2Se

   The structure of α-Cu_2Se is widely accepted as being ordered. Yet, the exact details of its structural form are still a subject of much debate. Recently, Nguyen *et al.* [117] and Chi *et al.* [118] used first-principles techniques to show that α-Cu_2Se has a small monoclinic unit cell with few atoms unlike α-Cu_2S. The structure proposed by Chi *et al.* was slightly more energetically stable although both groups agreed that α-Cu_2Se, like α-Cu_2S, has a layered structure.

2. β Cu_2Se

   The β phase of Cu_2Se is similar to the γ phase of Cu_2S only with Se forming the FCC sublattice instead of S. The Cu atoms are likewise disordered. The close structural relation between β-Cu_2Se and γ-Cu_2S makes β-Cu_2Se another interesting high temperature thermoelectric material with high ZT. However, β-Cu_2Se notably begins to form at a much lower 400K.[38]

4.3 Structural Models of Copper Sulfide and Copper Selenide

In this study, we are primarily interested in the high temperature phases of Cu_2S and Cu_2Se since they have been experimentally proven to be high ZT thermoelectric materials. Specifically these are the β and γ phases of Cu_2S as well as β-Cu_2Se mentioned in the previous section. In this section, we elucidate their structures in much greater detail. Since in all cases, S atoms form an ordered crystalline lattice, the main issue which we address is that of Cu disorder.

Before we begin further discussion, it is crucial for the reader to realise that the nomenclature for the various phases of Cu_2S varies between authors and can be very confusing. For

example, high chalcocite can refer to both the hexagonal and cubic phases [53, 56]. Other authors may even label the low temperature monoclinic phase of Cu_2S as the γ phase and the higher temperature hexagonal and cubic phases of Cu_2S as β and α respectively.[36, 119] Similar inconsistencies in nomenclature exist for the different phases of Cu_2Se as well. We wish to avoid confusion over the structural features of the various phases of Cu_2S and Cu_2Se that we are interested in. Therefore, from here on, we will refer to β-Cu_2S simply as hexagonal Cu_2S, γ-Cu_2S as cubic Cu_2S and β-Cu_2Se as cubic Cu_2Se.

4.3.1 Hexagonal Copper Sulphide

In hexagonal Cu_2S, where S atoms are hexagonally close-packed, it is reasonable to expect that the interaction between Cu atoms with the crystalline S sublattice will result in Cu atoms having certain preferred sites. Various groups have attempted to use X-ray diffraction for the purpose of identifying these preferred Cu sites each with an associated occupation probability. They typically agree on Cu preferring the $2b$ and $4f$ Wyckoff[1] sites but disagree on other possible Cu occupation sites.[53, 54, 116, 120] We find the models proposed by Buerger and Wuensch [54, 116] and Will *et al.* [53] to be most agreeable with each other. The Cu occupation data provided by Buerger and Wuensch lists the preferred Cu occupation sites as $2b$, $4f$ and $6g$.[54, 116] Will *et al.* [53] predicted Cu to also favourably occupy the $2b$, $4f$ and $6g$ in addition to $6h$ and $2a$. However, the $2a$ occupation probability for Cu as predicted by Will *et al.* is a measly 0.025 and should be ignored. Moreover, the $6h$ site predicted by Will *et al.* is unphysically close to the FCC S sites.[56] We therefore find it reasonable to develop structural models of hexagonal Cu_2S based on the Cu preferentially occupying the $2b$, $4f$ and $6g$ sites using the occupation probabilities supplied by Buerger and Wuensch.[54, 116] Details of the $2b$, $4f$ and $6g$ sites and their occupation probabilities are shown in Table 6. We choose to use lattice parameters provided by Will *et al.* as they provide more recent and detailed methods. According to Will *et al.*, $a = 4.033$Å and $c = 6.74$Å for hexagonal Cu_2S such that $c/a = 1.67$ at 573K. For comparison, in an ideal

[1] In Wyckoff notation, the number in front of the letter is the total number of equivalent symmetry sites in the unit cell. For example, $2b$ has a total of 2 equivalent symmetry sites and $192l$ has a total of 192 equivalent symmetry sites.

Table 6: S and Cu occupation probabilities for various XRD determined Wyckoff symmetry sites in hexagonal Cu_2S. The lattice parameters are $a = 4.033$Å and $c = 6.74$Å with $c/a = 1.67$ at 573K.[53]

System	Atom	Wyckoff site	Description	Occupation (Refs. [54] and [116])	Occupation (our initial configuration)
Hexagonal Cu_2S	S	$2c$ (1/3, 2/3, 1/4)	Hexagonal close-packed	100%	100%
	Cu (1)	$2b$ (0, 0, 1/4)	Intralayer with 3 S nearest neighbours	43.5%	43.5%
	Cu (2)	$4f$ (1/3, 2/3, 0.578)	Directly above and below each S	35.5%	35.5%
	Cu (3)	$6g$ (0, 1/2, 0)	Midway between 2 interlayer S atoms	21.0%	21.0%

hexagonal close-packed lattice, $c/a = \sqrt{\frac{8}{3}} = 1.63$.

The $2b$, $4f$ and $6g$ Cu symmetry sites in hexagonal Cu_2S are depicted in Fig. 17. The occupation probability for these sites are listed in Table 6. $2b$ sites are in the same plane as the S atoms and are in trigonal planar arrangements with the S atoms. The hexagonal pattern formed by S atoms and all possible $2b$ Cu sites is clearly depicted in Figure 17(b). The $4f$ and $6g$ are all interlayer sites. $4f$ sites are directly above and below each S atom. Individual $6g$ sites at the exact center of each layer diagonally link 2 S atoms from separate layers with both bond angles being 180°.

4.3.2 Cubic Copper Sulfide and Cubic Copper Selenide

As mentioned earlier, the S atoms in the cubic phase of Cu_2S are organized as an FCC lattice while the Cu atoms are completely disordered and mobile within the FCC sublattice of S atoms. Thus far, the structure of cubic Cu_2S has only been investigated experimentally by Will *et al.* [53] using X-ray diffraction (XRD) studies performed at a temperature of 773K. In this study, Will *et al.* found the lattice constant of cubic Cu_2S to be 5.762Å at

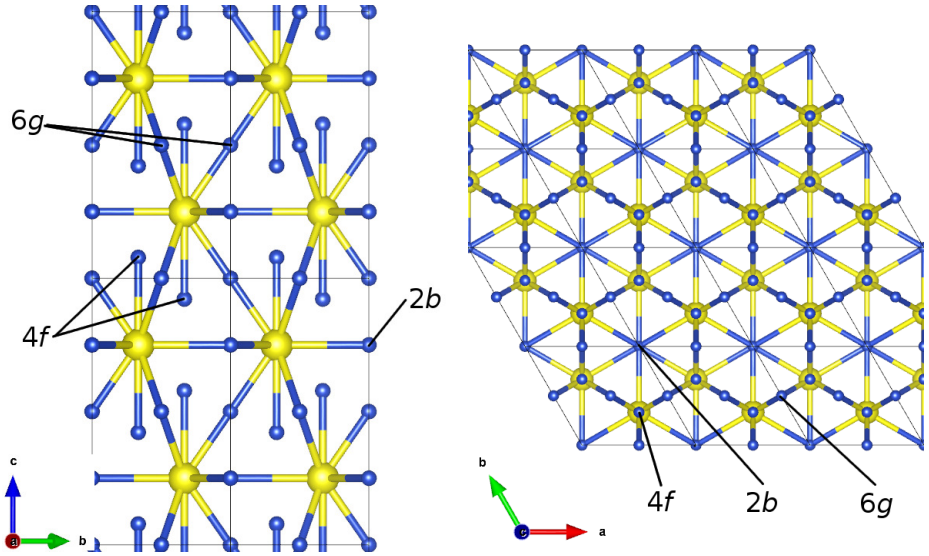

Figure 17: (a) and (b) show the hexagonal arrangement of S atoms (yellow spheres) in hexagonal Cu_2S as well as all equivalent Cu (blue spheres) symmetry sites of $2b$, $4f$ and $6g$. Hexagonal unit cell borders are demarcated by thin black lines. This figure was illustrated with VESTA.[101]

773K. Will *et al.* also determined the occupation probabilities of Cu at various Wyckoff symmetry sites ($8c$, $192l$ and $4b$). As in the case of hexagonal Cu_2S, we interpret these sites as the preferred sites for Cu atoms within the crystalline S sublattice. Results for the structural properties of cubic Cu_2S as determined by Will *et al.* are summarized in Table 7.[53]

The structure of cubic Cu_2Se at 550K was investigated via XRD by Skomorokhov *et al.* [57] and these results are summarized alongside those for Cu_2S in Table 7. Unlike the case of cubic Cu_2S, Cu atoms in Cu_2Se are seen to have a strong preference for the tetragonal $8c$ sites and also the $32f$ sites to a smaller extent. Skomorokhov *et al.* further determined the temperature dependence of the lattice constant of cubic Cu_2Se up to 625 K where the lattice constant reached 5.8455Å. Extrapolating this data, we estimate the lattice constant of Cu_2Se to increase slightly to 5.85Å at 900K.

We illustrate the S and Cu Wyckoff symmetry sites of Cu_2S in Figs. 18(a) and (c). Fig. 18 may be viewed as a conventional FCC S lattice with all possible $8c$ and $192l$ Cu sites shown in between the S sites. For simplicity, we do not show the single $4b$ Cu site which is at the center of the cell. The Cu $8c$ Wyckoff site is the tetragonal site which has four

Table 7: S, Se and Cu occupation probabilities for various XRD determined Wyckoff symmetry sites in cubic Cu_2S at 773K and Cu_2Se at . The lattice constant of Cu_2S is 5.762Å.[53]

System	Atom	Wyckoff site	Description	Occupation (Refs. [53] and [57])	Occupation (our initial configuration)
Cubic Cu_2S	S	4*a* (0, 0, 0)	Face-centered cubic	100%	100%
	Cu (1)	8*c* (1/4, 1/4, 1/4)	Tetrahedral	25.75%	30%
	Cu (2)	192*l* (0.11, 0.17, 0.28)	4 clusters of 6 sites arranged tetrahedrally around each 8c site	69.5%	70%
	Cu (3)	4*b* (1/2, 1/2, 1/2)	Octahedral	4.75%	0%
Cubic Cu_2Se	Se	4*a* (0, 0, 0)	Face-centered cubic	100%	100%
	Cu (1)	8*c* (1/4, 1/4, 1/4)	Tetrahedral	71.87%	70%
	Cu (2)	32*f* (1/3, 1/3, 1/3)	4 sites arranged tetrahedrally around each 8c site	28.13%	30%

nearest S neighbours within each quadrant. The 192l sites form complex polyhedra within each of the eight quadrants and are also located on the faces of the tetrahedra formed by groups of four nearest S neighbours centered around their closest 8c site.

The Se and Cu Wyckoff symmetry sites of Cu_2Se are likewise depicted in Figs. 18(b) and (d). In this case, the Se instead of S atoms fully occupy conventional FCC sites and the Cu 8c site is similarly described as for the case of Cu_2S. The Cu 32f site form tetrahedra around each Cu 8c site. In both Cu_2S and Cu_2Se, we see that S atoms form a tetrahedral cage around the preferred Cu occupation sites.

4.3.3 Algorithm for Constructing Disordered Models of Copper Sulfide and Copper Selenide

Here, we describe the algorithm which we use for creating structural models of the disordered phases of copper sulfide and copper selenide. The input data for the symmetry sites and their respective occupation probabilities are taken from Tables 6 and 7. Let us assume that there are n Wyckoff symmetry types for Cu, each with occupation probability x_n such that $x_1 + x_2 + \cdots + x_n = 1.0$. We then choose a random number r_1 along the number line ranging between 0 and 1 as drawn in Fig. 19. If the random number is within the range $\sum_{i=0}^{m-1} x_i$ to $\sum_{i=0}^{m} x_i$, where m is some number from 1 to n, then a type m Wyckoff site is selected. At this point, there are now M symmetry sites of type m to choose from, with each choice being equally probable. A second random number r_2 ranging from 1 to M is generated in order to finally choose one of the M symmetry sites of type m for Cu to occupy. This process is repeated until the desired number of Cu atoms have been added to the structure. The S or Se sites are themselves all fully occupied. Lukashev *et al.* [56] applied a similar method for generating their random structures of hexagonal and cubic copper sulfide. We make use of the GNU Scientific Library (GSL) [121] random number generator to generate the random numbers which we require.

To simulate enough Cu disorder, we make use of $2 \times 2 \times 2$ supercells for each case. Thus, in our hexagonal copper sulfide supercells, there are 32 Cu and 16 S atoms. In our cubic copper sulfide (selenide) supercells, there are 64 Cu and 32 S (Se) atoms. Supercells any larger than $2 \times 2 \times 2$ are too expensive to handle computationally, given our current

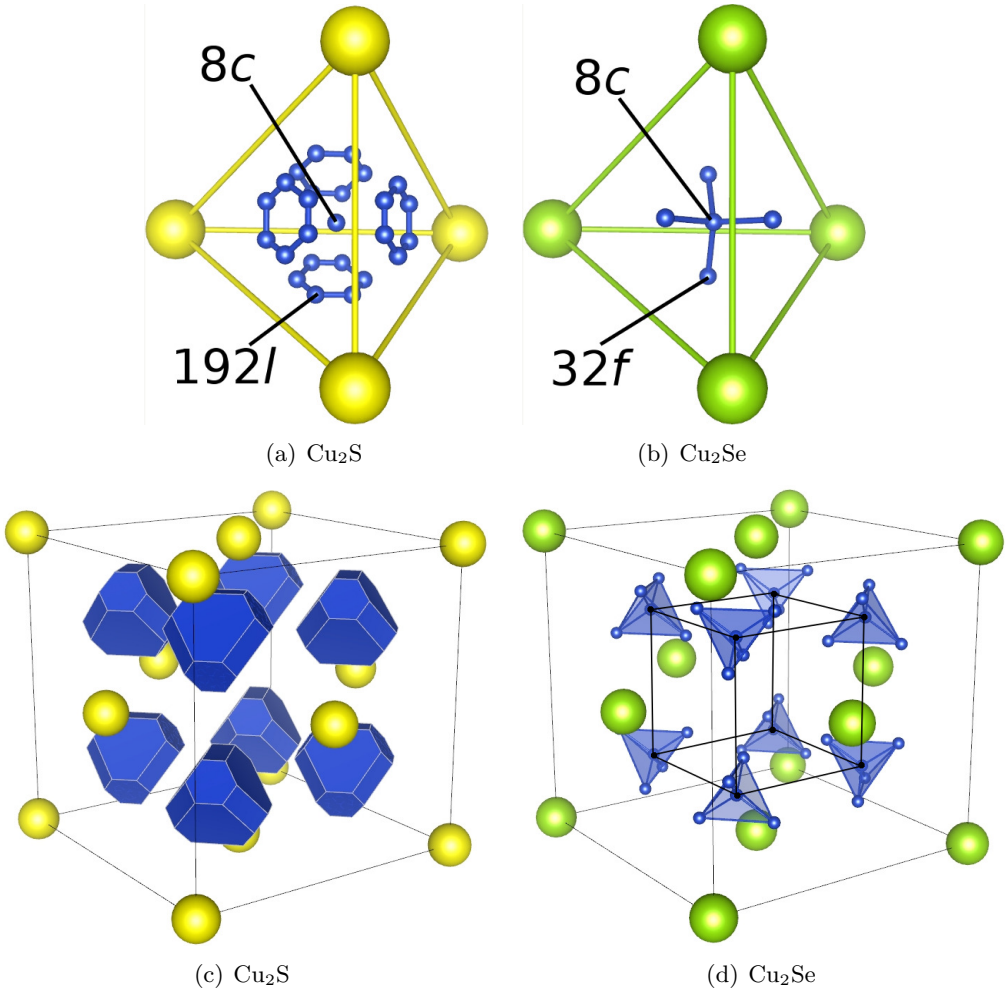

(a) Cu_2S (b) Cu_2Se

(c) Cu_2S (d) Cu_2Se

Figure 18: (a) and (b) highlight the preferred Cu symmetry sites relative to the tetrahedron formed by closest S or Se atoms. (c) and (d) show the cubic structure of the high temperature phases of Cu_2S and Cu_2Se. S (yellow spheres) and Se (green spheres) atoms in both structures occupy fixed FCC sites. Cu (blue spheres) atoms are shown at all preferred symmetry sites. For simplicity, we do not highlight the numerous Cu sites with blue spheres in (c). This figure was illustrated with VESTA.[101]

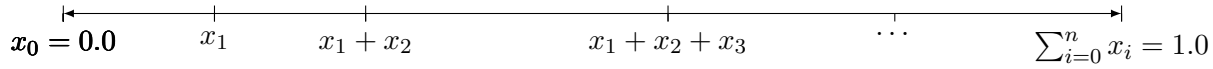

Figure 19: Number line from 0.0 to 1.0. The x_n are occupation probabilities for the n different Cu symmetry site types.

resources.

4.3.4 Random Structure Search

In order to find stable structures of disordered hexagonal copper sulfide and cubic copper sulfide and selenide, we create and structurally optimize twenty different random structures for each of these materials. We then keep the four lowest energy structures of each material for further analysis.

For structural optimizations, we use a generalised gradient approximation (GGA) [122, 123] within the context of density functional theory (DFT) with projector augmented wave (PAW) pseudopotentials.[71, 72] We are able use a relatively small K-point grid to sample the Brillouin zone since our supercells are large. For hexagonal copper sulfide, we use a $3 \times 3 \times 2$ k-point grid while for both cubic copper sulfide and copper selenide, we use a $2 \times 2 \times 2$ k-point grid. We also use a force convergence criterion of $0.02\text{eV}\text{Å}^{-1}$. All structural optimizations are implemented using the Vienna Ab-Initio Simulation Package (VASP).[96, 97, 98, 99]

We use denser k-point grids for electronic band structure and density of states calculations. For density of states calculations on cubic Cu_2S and Cu_2Se, the k-point grid size of $9 \times 9 \times 9$ and in hexagonal Cu_2S, we use a k-point grid of $13 \times 13 \times 7$. The electronic structures calculated using these parameters are fed as input to BoltzTraP which calculates the related thermoelectric properties.

We show in Fig. 20 the fully optimized lowest energy structures of hexagonal and cubic Cu_2S and cubic Cu_2Se. The defining features of each structure are still intact after optimization, despite the lack of symmetry resulting from massive Cu disorder. Specifically, a rough hexagonal sublattice of S is maintained in hexagonal Cu_2S while an approximate FCC S (Se) sublattice is maintained for cubic Cu_2S (Cu_2Se). In hexagonal Cu_2S, most if not all of the Cu atoms are also still clearly intralayer or interlayer.

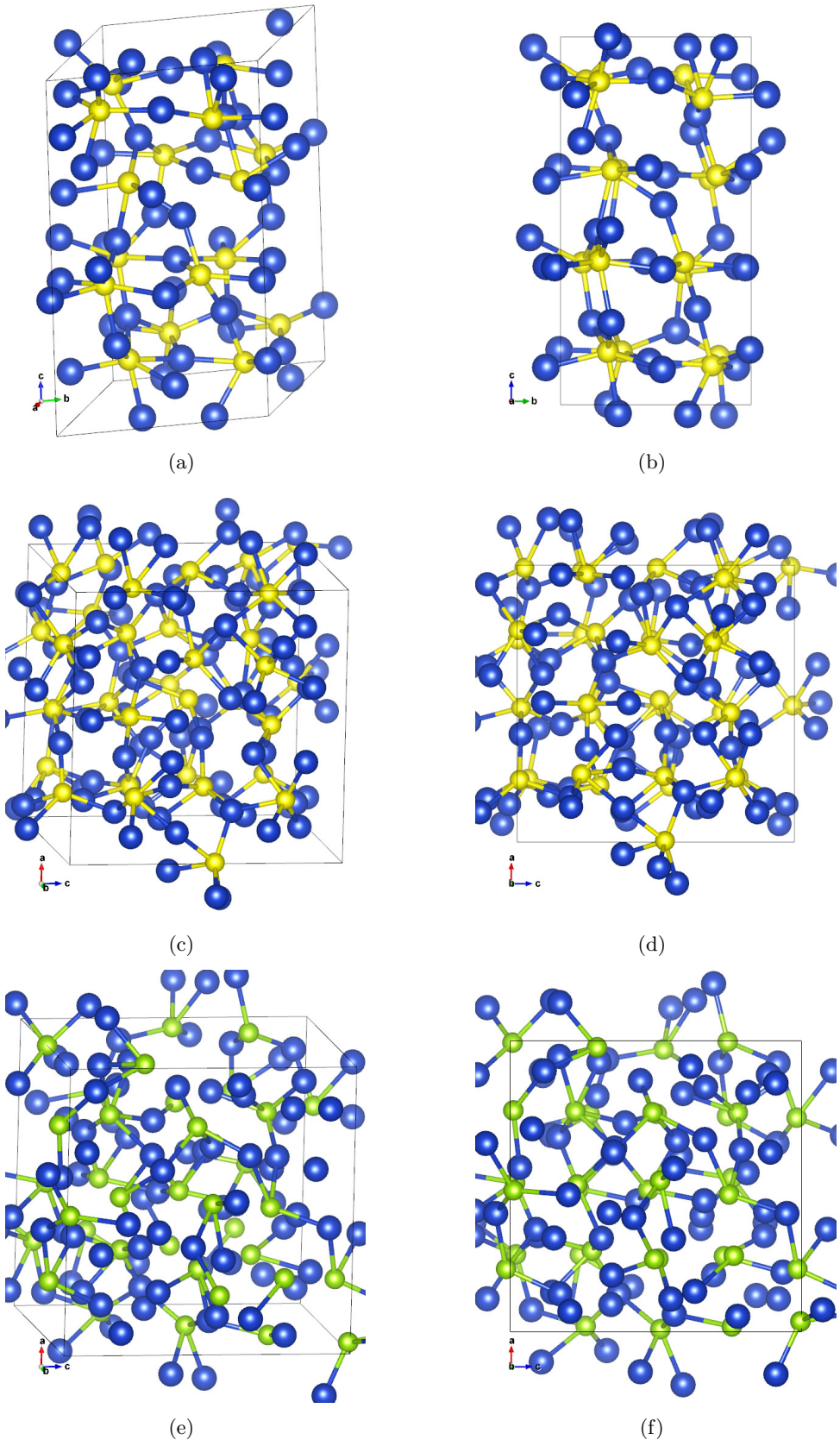

Figure 20: Lowest energy structures of hexagonal ((a) and (b))and cubic ((c) and (d))Cu_2S and cubic ((e) and (f)) Cu_2Se after structural optimization. Solid black lines demarcate the $2 \times 2 \times 2$ supercell boundaries. This figure was illustrated using VESTA.[101]

Table 8: Energy per Cu_2S/Se unit in the four most energetically stable structures of hexagonal and cubic Cu_2S and cubic Cu_2Se from a random structure search.

	Energy per Cu_2S/Se unit (eV) in sample			
	1	2	3	4
Hexagonal Cu_2S	-11.975	-11.972	-11.969	-11.966
Cubic Cu_2S	-11.936	-11.927	-11.927	-11.927
Cubic Cu_2Se	-11.209	-11.205	-11.194	-11.189

The energies of the four most energetically stable structures hexagonal and cubic Cu_2S and cubic Cu_2Se are recorded in Table 8. The four samples in each system are labelled such that the energies increase from sample 1 to sample 4. As can be seen, the differences in energy between all four lowest energy structures in each system is less than 0.05eV which is very small. Yet, this is enough to account for sizeable differences between their electronic structures and thermoelectric properties, particular in the case of hexagonal Cu_2S.

4.4 Bader Charge Analysis

First-principles quantum theory, as applied in VASP and similar simulation packages, does not specify how the electronic charge density of a molecule or solid should be partitioned between the constituent atoms. However, Bader developed a formalism for partitioning molecules or solids into individual atoms based on this continuous electronic charge density. In Bader charge analysis as this is commonly known, the constituent atoms are quite intuitively separated by surfaces which pass through the minima in the electronic charge density of a molecule or solid.[124] Thus, Bader charge analysis affords us the opportunity to estimate charges on atoms within molecules and solids given the electronic charge density of the entire system. We use the Bader code developed by Henkelman *et al.* to perform the required Bader charge analysis on Cu_2S and Cu_2Se in order to estimate the number of electrons on individual S, Se and Cu atoms.[125, 126, 127] These are averaged over each atomic species in hexagonal and cubic Cu_2S and cubic Cu_2Se and listed in Table 9.

In our simulations, the valence electron configuration for Cu is $3d^{10}\ 4s^1$ while that for S and Se are $3s^2\ 3p^4$ and $4s^2\ 4p^4$ respectively. The results from our Bader charge analysis show that in both cubic and hexagonal Cu_2S, each Cu on average transfers about 0.4 electrons

Table 9: Average number of electrons on S, Se and Cu atoms within hexagonal and cubic Cu_2S and hexagonal Cu_2Se. The average number of electrons on Cu atoms is listed within brackets beside the average number of electrons on either S or Se atoms.

	Average number of electrons per S, Se and Cu in sample			
	1	2	3	4
Hexagonal Cu_2S	6.79 (10.61)	6.78 (10.61)	6.76 (10.62)	6.77 (10.61)
Cubic Cu_2S	6.79 (10.61)	6.78 (10.61)	6.80 (10.60)	6.78 (10.61)
Cubic Cu_2Se	6.53 (10.73)	6.54 (10.73)	6.54 (10.73)	6.54 (10.73)

to each S atom, which then receives 0.8 electrons on average, since there are 2 Cu atoms for every S atom. In Cu_2Se, each Cu atom transfers close to 0.25 electrons to each S atom which receives about 0.5 electrons. Therefore, we conclude that Cu-S and Cu-Se bonds in hexagonal and cubic Cu_2S along with cubic Cu_2Se are not completely ionic. We perform additional Bader charge analysis on cubic $Cu_{2-x}S$ and $Cu_{2-x}Se$ during molecular dynamics simulations at 900K. These results lend further support to our conclusions here and we describe them in detail in the next chapter.

4.5 Electronic structure

Figs. 21, 22 and 23 show the band structures and density of states (DOS) of hexagonal Cu_2S cubic Cu_2S and cubic Cu_2Se respectively. Each figure consists of four plots corresponding to the four most energetically stable structures in each case. We focus primarily on the valence bands since Cu_2S and Cu_2Se are normally p doped. Considering all electronic band structures, we see a few common trends within the valence bands. Firstly, all the electronic band structures shown have finite band gaps. We list the size of these gaps in Table 10. Of course, these gaps are all far smaller than the experimentally predicted band gap of around 1.2eV for each material. This is a well known and common issue with the use of approximate exchange correlation functions in DFT. Nevertheless, the fact that we obtain finite band gaps is highly significant because it underscores the importance of Cu disorder on the size of the band gap. Previous electronic studies on the fictitious ordered antifluorite structures of Cu_2S and Cu_2Se failed to produce a band gap without the use of additional Coulomb interaction terms or hybrid functionals.[111, 112] Secondly, the valence bands just under the

Table 10: Band gaps of hexagonal and cubic Cu_2 and cubic Cu_2Se. Samples 1 to 4 for each system are in order of increasing energy as determined by first-principles structural optimization using VASP.

System	Sample	Band gap (eV)
Hexagonal Cu_2S	1	0.44
	2	0.27
	3	0.27
	4	0.40
Cubic Cu_2S	1	0.61
	2	0.61
	3	0.61
	4	0.45
Cubic Cu_2Se	1	0.10
	2	0.18
	3	0.22
	4	0.14

valence band edge are composed predominantly of a mix between S/Se-p and Cu-d orbitals. Thirdly, bands close to the valence band edges are typically very flat, especially for those further below the conduction band edge.

The electronic band structures of cubic Cu_2S and Cu_2Se are most different close to the band edges. Here, the conduction minima and valence maxima of the Cu_2Se bands are clearly more dispersive than those belonging to Cu_2S. Furthermore, the band gaps in Cu_2Se are noticeably smaller than those in Cu_2S. This is likely because cubic Cu_2Se, having a higher proportion of Cu atoms located closer to the tetrahedral $8c$ position, has a structure that is more closely related to the idealized antifluorite structure. Earlier first-principles studies have shown that Cu_2S and Cu_2Se in the ordered antifluorite structure have either minimal or no band gap.

In general, the features of the electronic bands and density of states do not change much with Cu disorder amongst the most energetically stable structures which we examine. Extending the range of the density of states for the lowest energy structure of hexagonal Cu_2S, cubic Cu_2S and cubic Cu_2Se, we note a few more interesting features. From Fig. 24,

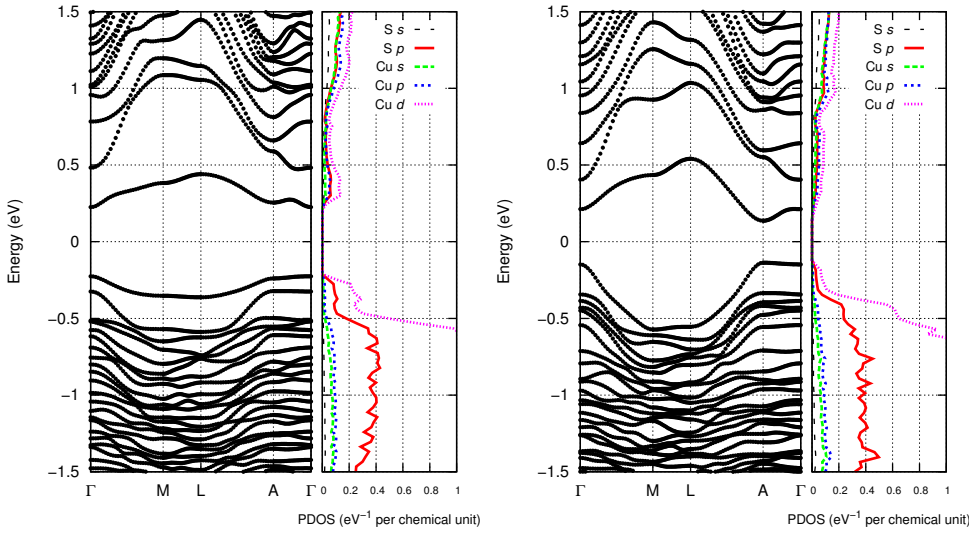

(a) Sample 1

(b) Sample 2

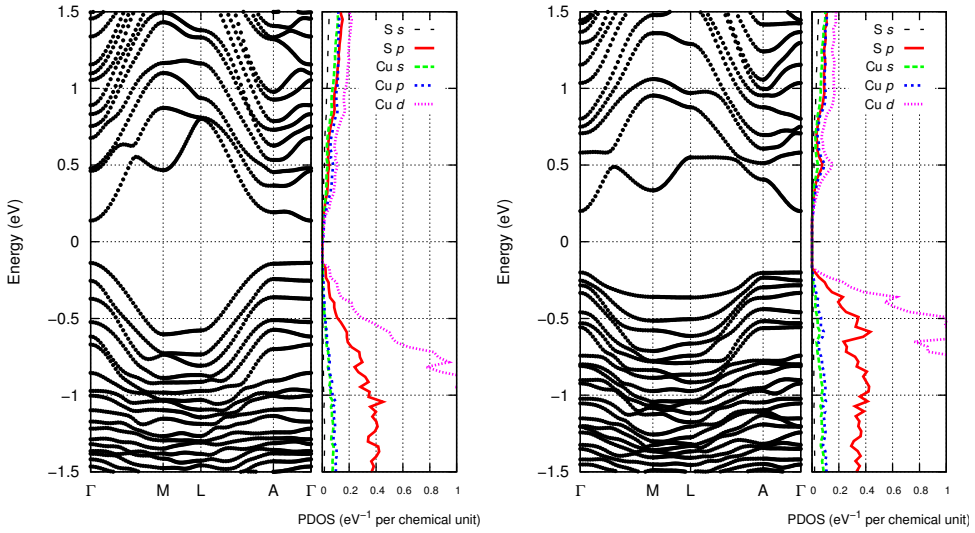

(c) Sample 3

(d) Sample 4

Figure 21: (a), (b), (c) and (d) are the electronic band structures and density of states of hexagonal Cu_2S. They are arranged in order of increasing energy. The zero of energy is arbitrarily located at the gap center.

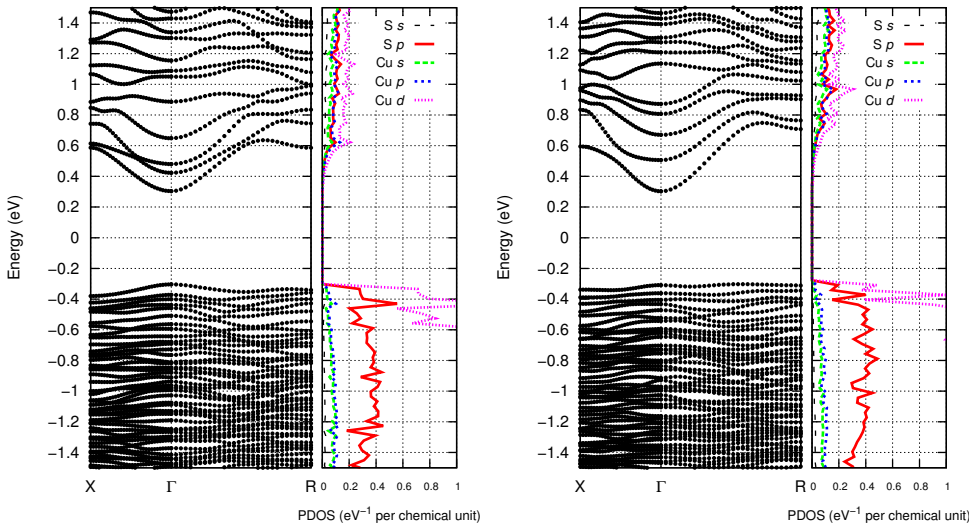

(a) Sample 1

(b) Sample 2

(c) Sample 3

(d) Sample 4

Figure 22: (a), (b), (c) and (d) are the electronic band structures and density of states of cubic Cu_2S from first-principles structural optimization. They are arranged in order of increasing energy. The zero of energy is arbitrarily located at the gap center.

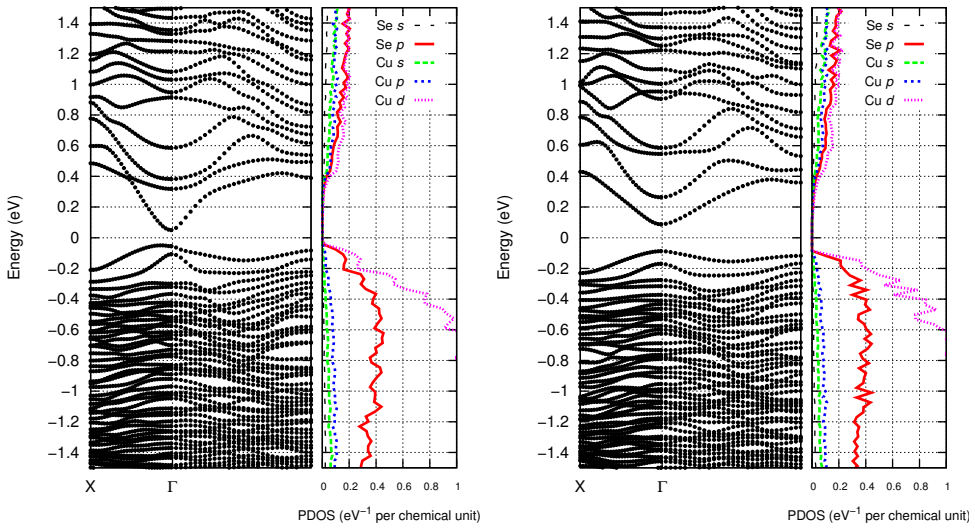

(a) Sample 1

(b) Sample 2

(c) Sample 3

(d) Sample 4

Figure 23: (a), (b), (c) and (d) are the electronic band structures and density of states of cubic Cu_2Se from first-principles structural optimization. They are arranged in order of increasing energy. The zero of energy is arbitrarily located at the gap center.

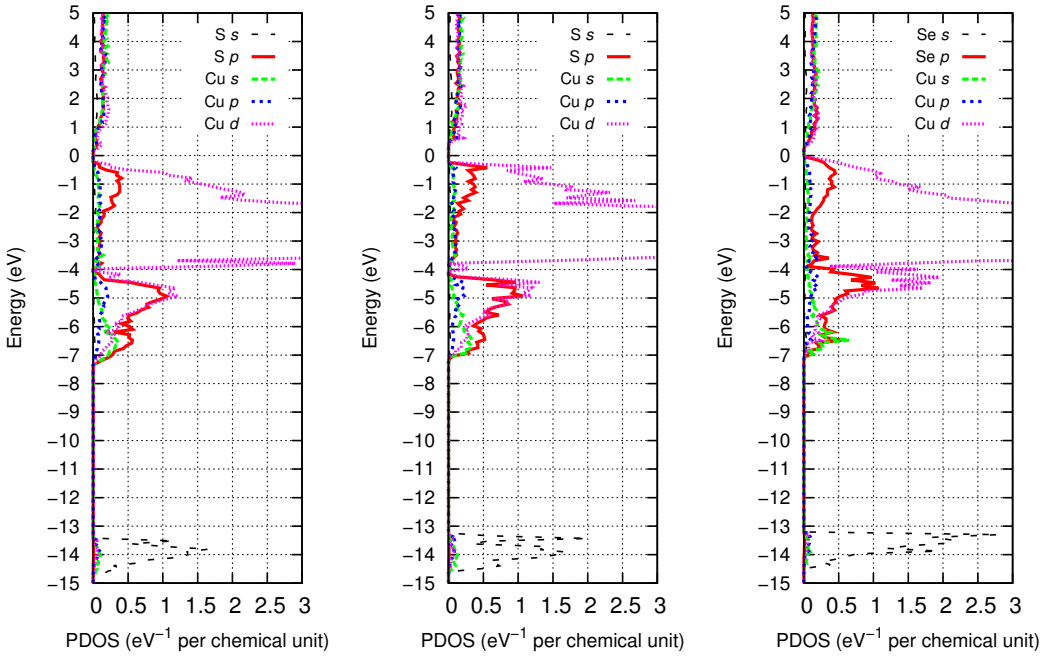

(a) (b) (c)

Figure 24: (a), (b), (c) and (d) are the density of states of most energetically stable structure obtained for hexagonal Cu_2S, cubic Cu_2S and cubic Cu_2Se respectively.

we see that each density of states plot may be divided into three regions within the valence bands. The first region is far below the band gap at around -15eV. This is where the lowest energy non-bonding S-s or Se-s states are concentrated.

Between about -4eV to -7eV, there is a second region. The lower part of this region consists mostly of S/Se-p and Cu-s bonding states while the upper portion is dominated by S/Se-p hybridized with Cu-d bonding states. This makes sense since the symmetry of p orbitals allows p orbitals to overlap much better with s orbitals than d orbitals.

The third region represents the density of states from around -4eV up to the valence band edge around 0eV. In this third region, despite a strong presence of S-p or Se-p states close to the band edge, there is an overwhelmingly huge peak in the number of Cu-d non-bonding states. d orbitals in general are highly non-interacting and they therefore manifest themselves as very flat bands in the electronic band structure. This is exactly what we see for bands within a few eVs under the valence band edge. The flatness of the valence bands a few k_BT below the valence band edge has important consequences. Generally, flat bands

imply a high carrier effective mass since carrier effective mass is inversely proportional to band curvature. This is highly beneficial as it contributes towards large Seebeck coefficient. At the same time though, it also results in a lower carrier group velocity which lowers conductivity. We show in detail how the electronic bands balance out the Seebeck coefficient and hole conductivity in the next section.[85, 128] We elaborate further on these points when we discuss the thermoelectric properties of Cu_2S and Cu_2Se in the next section.

Interestingly enough, the general features of the density of states described above are also present in the density of states for the highly idealized antifluorite structure of Cu_2S and Cu_2Se.[56, 111, 112, 113] However, there is one main difference which stands out. In the case of antifluorite Cu_2S (Cu_2Se), the second (S/Se-s,Cu-s and Cu-d bonding orbitals) and third region (Cu-d nonbonding orbitals) in the density of states as just described above will become narrower and separate with a distinct energy gap of about 1eV.[56, 111, 112, 113]

We find our first-principles density of states for Cu_2S and Cu_2Se to be consistent with those obtained via photoemission studies performed by Kashida *et al.*.[129] Although Kashida *et al.* were unable to confirm the phases and structures of their Cu_2S and Cu_2Se samples, their photoemission results show the peak density of S-p or Se-p states are separated from the peak density of Cu-d states by about 2.5eV.[129] This is also what our first-principles results also indicate.

4.6 Thermoelectric properties

Cu deficiencies are common in Cu_2S and Cu_2Se which make them natural p-type semiconductors. As such, we focus on their p-type thermoelectric properties which are determined by their valence bands.

4.6.1 Hexagonal Cu_2S

We first discuss the thermoelectric properties of hexagonal Cu_2S which are shown in Fig. 25. These thermoelectric properties namely are the Seebeck coefficient (S), electrical conductivity (σ/τ) and power factors ($S^2\sigma/\tau$). Recall that in the constant relaxation time approximation which we use for calculating thermoelectric properties, the relaxation time is an unknown constant and only the Seebeck coefficient can be calculated independently of

the relaxation time (τ) and be compared directly with experiment. We also calculate these quantities only after applying a scissor operator shift [130] to the conduction bands such that the band gap resembles the experimental gap as closely as possible. The rationale for doing so is to prevent the smearing factor $\partial f/\partial \epsilon$ in the Boltzmann transport equations (Eq. 142) from including erroneous contributions from the conduction bands. This smearing is of particular concern especially at high temperatures. We choose a constant 0.8eV shift for all cases which is high enough for the conduction bands to have minimal influence as expected within experimental samples. Since hexagonal Cu_2S has a layered structure, we average these tensor quantities in-plane (xy) and out-of-plane (z) and present them separately.

At a carrier concentration of $1 \times 10^{19} \mathrm{cm}^{-3}$, the in-plane Seebeck coefficient for hexagonal Cu_2S ranges between $325 \mu \mathrm{VK}^{-1}$ and $475 \mu \mathrm{VK}^{-1}$ for our four most energetically stable structures. From here, the Seebeck coefficient generally decreases, although not always smoothly, with increasing hole concentration. This is consistent with the Mott relation.[131] The in-plane Seebeck coefficients of samples 1 and 4 are considerably larger than those of samples 2 and 3. Considering their electronic band structures in Fig. 21, this is related to how dispersive the valence bands are near to the valence band edge. We note that samples 1 and 4 have the flattest valence bands. According to Kuroki *et al.* [132], the magnitude of the Seebeck coefficient is generally proportional to the difference between the squares of the carrier group velocities above and below μ in Eq. 142. This implies that flatter bands contribute to a higher Seebeck coefficient and this is indeed what we are observing here.

The out-of-plane Seebeck coefficients for samples 1,2 and 4 are similar to their in-plane counterparts for low hole concentrations. Only for sample 3 is the out-of-plane Seebeck coefficient significantly larger than its in-plane Seebeck coefficient. As hole concentration is increased, these out-of-plane Seebeck coefficients decay to zero but not as quickly as the corresponding in-plane Seebeck coefficients. Overall, our results indicate better performance of the Seebeck coefficient in the layer direction. Since we see from Eq. 142 that the Seebeck coefficient is calculated from the inverse of the electrical conductivity, this is a direct consequence of the electrical conductivity in the layer direction being an order of magnitude less than it is within the layer.

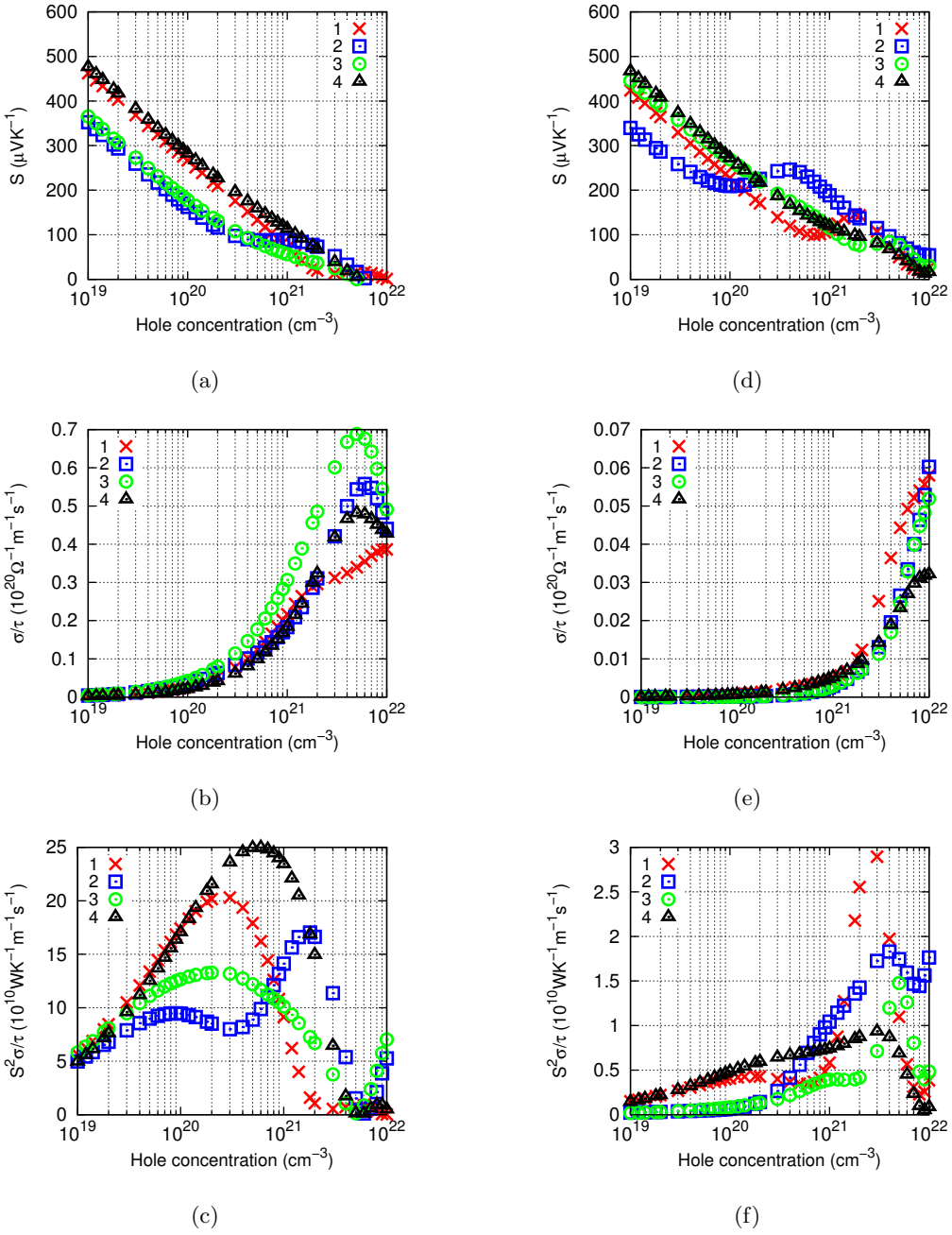

Figure 25: (a), (b) and (c) are the Seebeck coefficient, electrical conductivity and power factor for hexagonal Cu_2S respectively averaged over x and y directions. (d), (e) and (f) are the Seebeck coefficient, electrical conductivity and power factor for hexagonal Cu_2S respectively in the z layer direction only. All quantities are calculated at $T = 450$K.

Expectedly, the electrical conductivity coupled with the relaxation time as σ/τ_e, increases with the hole concentration as the Fermi level is shifted to include more valence bands. This is opposite to the behaviour of the Seebeck coefficient. Due to this competition between the Seebeck coefficient and the electrical conductivity, we are interested in the optimal power factor $S^2\sigma/\tau$ which represents the trade off between the two quantities. We cannot predict an absolute value for the power factor due to the unknown electronic relaxation time. However, from our results, we are still able to predict the range of hole concentration within which the power factor can be optimized. The in-plane power factor reaches its optimum within a large range of hole concentrations between $2 \times 10^{20}\text{cm}^{-3}$ and $2 \times 10^{21}\text{cm}^{-3}$ while the out-of-plane power factor is more precise and reaches its optimum at hole concentrations between $3 \times 10^{21}\text{cm}^{-3}$ to $5 \times 10^{21}\text{cm}^{-3}$.

4.6.2 Cubic Cu_2S and Cu_2Se

The thermoelectric properties of cubic Cu_2S and Cu_2Se are far more pertinent than those of hexagonal Cu_2S. The high ZT values of Cu_2S and Cu_2Se were experimentally obtained at temperatures of around 1000K which is well above the temperature beyond which they transition into their cubic phases.[36, 38] In Fig. 26, we show how the Seebeck coefficient (S), electrical conductivity (σ/τ) and power factors ($S^2\sigma/\tau$) of our structurally optimized cubic Cu_2S and Cu_2Se vary with hole concentration at 900K. These quantities as presented in Fig. 26 are the average of the xx, yy and zz tensor components since all cubic axes are equivalent. At first glance, we see a lot more precision for the cubic structures in comparison to the those for the hexagonal Cu_2S structure. This is likely due to the cubic structures being more isotropic which is not the case in the layered hexagonal Cu_2S structure.

As mentioned earlier, only the Seebeck coefficient is calculated independently of the electronic relaxation time. We therefore use the Seebeck coefficient as a basis for comparing our results. In cubic Cu_2S, we see that differences between our optimized structures have a spread of about $80\mu\text{VK}^{-1}$ in the Seebeck coefficient at hole concentrations of 10^{19}cm^{-3}. This spread subsequently decreases as the carrier concentration is increased. For cubic Cu_2Se, the corresponding spread of calculated Seebeck coefficients is a smaller and more consistent

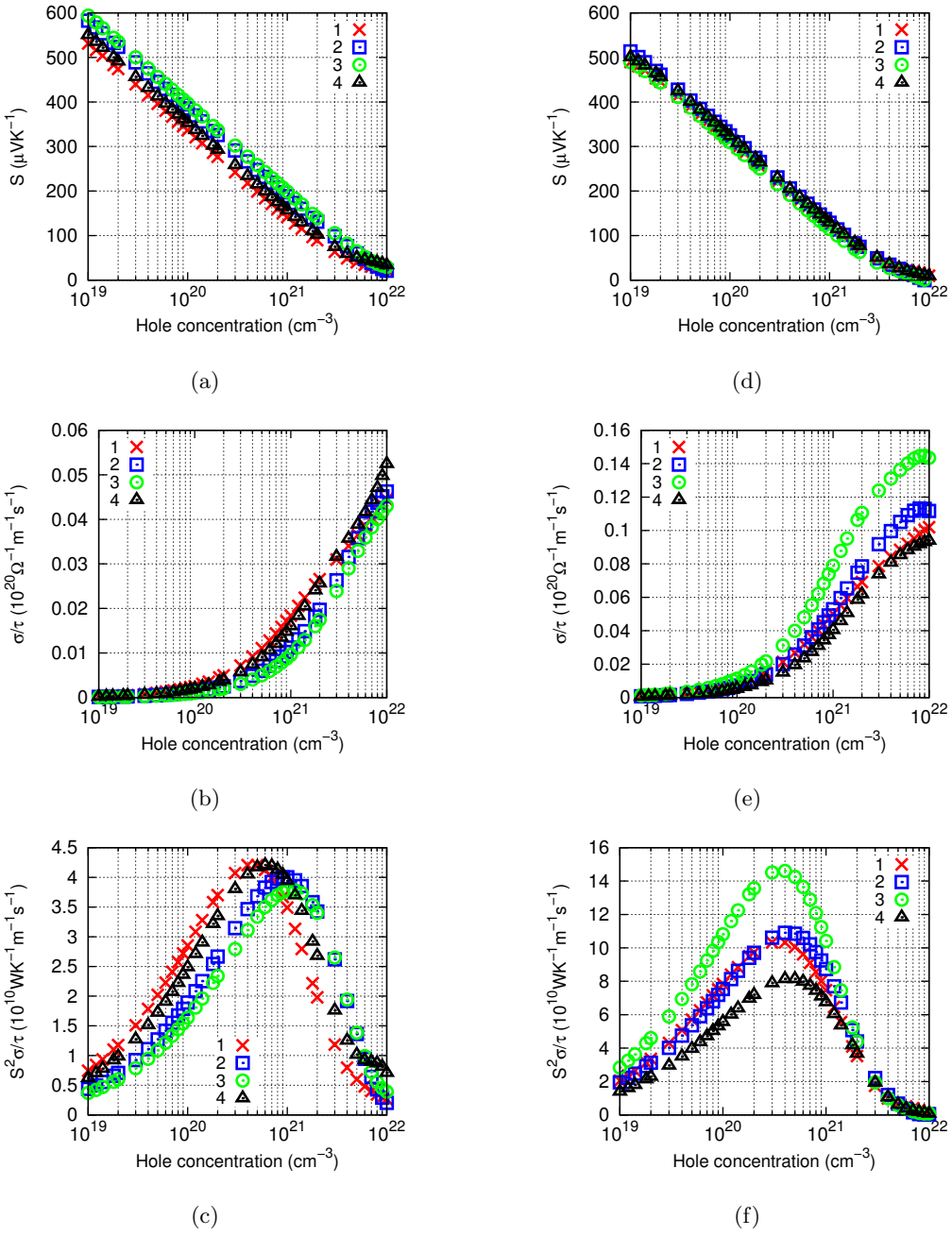

Figure 26: (a), (b) and (c) are the Seebeck coefficient, electrical conductivity and power factor for Cu_2S respectively. (d), (e) and (f) are the Seebeck coefficient, electrical conductivity and power factor for Cu_2Se respectively. All quantities are calculated at 900K.

$40\mu\text{VK}^{-1}$ over the entire range of carrier concentrations. This implies that thermoelectric measurements carried out on cubic Cu_2S can be expected to be more reproducible at least in comparison to those performed on hexagonal Cu_2S. We see that for both cubic Cu_2S and Cu_2Se, the Seebeck coefficient can attain high values of over $200\mu\text{VK}^{-1}$ for hole concentrations as high as $3 \times 10^{20}\text{cm}^{-3}$, which is essential for coinciding with a high electrical conductivity. Overall, the Seebeck coefficient of cubic Cu_2S and Cu_2Se can be expected to be larger than that of hexagonal Cu_2S.

The power factor, which we report as $S^2\sigma/\tau$, again describes the hole concentration at which we expect to find a good balance of Seebeck coefficient and electrical conductivity for optimum ZT. As can be seen, the optimum hole concentration for the power factor occurs occurs at about $8\times10^{20}\text{cm}^{-3}$ in cubic Cu_2S and $5\times10^{20}\text{cm}^{-3}$ in cubic Cu_2Se.

In Table 11, we show some experimental measurements for hole concentration p and Seebeck coefficients for Cu_2S and Cu_2Se extracted from Reference [36]. We calculate Seebeck coefficients for Cu_2S and Cu_2Se for comparison with these experimental results at 750K based on the hole concentrations p provided in Table 11. Do note though that the structures of $Cu_{1.98}S$ and $Cu_{1.97}S$ which have extra Cu deficiencies are different from Cu_2S but only slightly as the defining FCC S lattice is still maintained. As such, we do not expect an exact agreement with experimental results in these cases.

According to experiments, increasing Cu deficiencies in Cu_2S naturally results in increased p doping. This in turn results in decreasing Seebeck coefficients which our theoretical results agree with. However, we overestimate S in Cu_2S by between $90\mu\text{VK}^{-1}$ to $140\mu\text{VK}^{-1}$ but we underestimate S in Cu_2Se by around $150\mu\text{VK}^{-1}$ at 750K using the hole concentrations provided by Reference [36].

In Fig. 27(a) we show how our calculated S, using only our lowest energy structures of cubic Cu_2S and Cu_2Se, vary with temperature for the fixed hole concentrations given in Table 11. Judging by the consistency in the Seebeck coefficients in Fig. 26, we do not expect the results shown here to vary greatly among different random structures. Generally, S is seen to vary minimally by about $25\mu\text{VK}^{-1}$ between 750K to 1000K at constant hole concentrations. The experimentally determined variation of S in $Cu_{2-x}S$ ($x = 0.00, 0.02, 0.03$) with

Table 11: Experimental data obtained from Reference [36] for Cu_2S and Cu_2Se. We also list our calculated Seebeck coefficients for comparison. Experimentally measured hole concentrations p are performed using Hall measurements.[36] Discrepancies between theoretical and experimental results are listed on the last row.

Properties	Cu_2S	$Cu_{1.98}S$	$Cu_{1.97}S$	Cu_2Se
p at 750K (10^{20}cm^{-3}) (Ref. [36])	0.276	0.522	1.56	20.1
S at 750K (μVK^{-1}) (Ref. [36])	338	295	242	192
S at 750K (μVK^{-1}) (Our calculation)	480	425	331	47
Discrepancy in S (μVK^{-1})	142	130	89	-145

temperature is shown in Fig. 27(b) which is taken directly from Reference [36]. From Fig. 27(b), we see that the Seebeck coefficient of $Cu_{2-x}S$ vary within the range of 350μVK^{-1} to 450μVK^{-1} as temperatures rise from 750K to 1000K. In the same temperature range, Fig. 27(c) shows the Seebeck coefficient in Cu_2Se rising from about 200μVK^{-1} to 300μVK^{-1}. However, all this likely includes the effect of changing carrier concentrations which can drastically affect S. As seen in Table 11, hole concentrations are capable of increasing by around five times in Cu_2S and Cu_2Se between 300K and 750K.

Overall, our theoretical results shown in Fig. 26 agree with experiment in that the Seebeck coefficient of Cu_2Se is typically less than than of Cu_2S. We also agree that it is entirely possible for the experimental Seebeck coefficient to reach as high as 400μVK^{-1} in the case of Cu_2S and 300μVK^{-1} in Cu_2Se at temperatures close to 1000K and with hole concentrations of the order 10^{20}cm^3. These points are demonstrated clearly in Fig. 26 However, we are unable to perform a more rigorous comparison due to a lack of experimental data. Another issue is that thermoelectric properties calculated from experiment are notoriously difficult to reproduce,[42, 44] especially when dealing with complex materials. This often leads to conflicting reports of ZT for the same material system.

4.7 Conclusions

Copper sulfide and copper selenide have various phases depending on temperature and Cu deficiencies. Over the years, there have been a handful of first-principles studies on Cu_2S and Cu_2Se. Unfortunately, most of these pertain to the fictitious antifluorite structure of

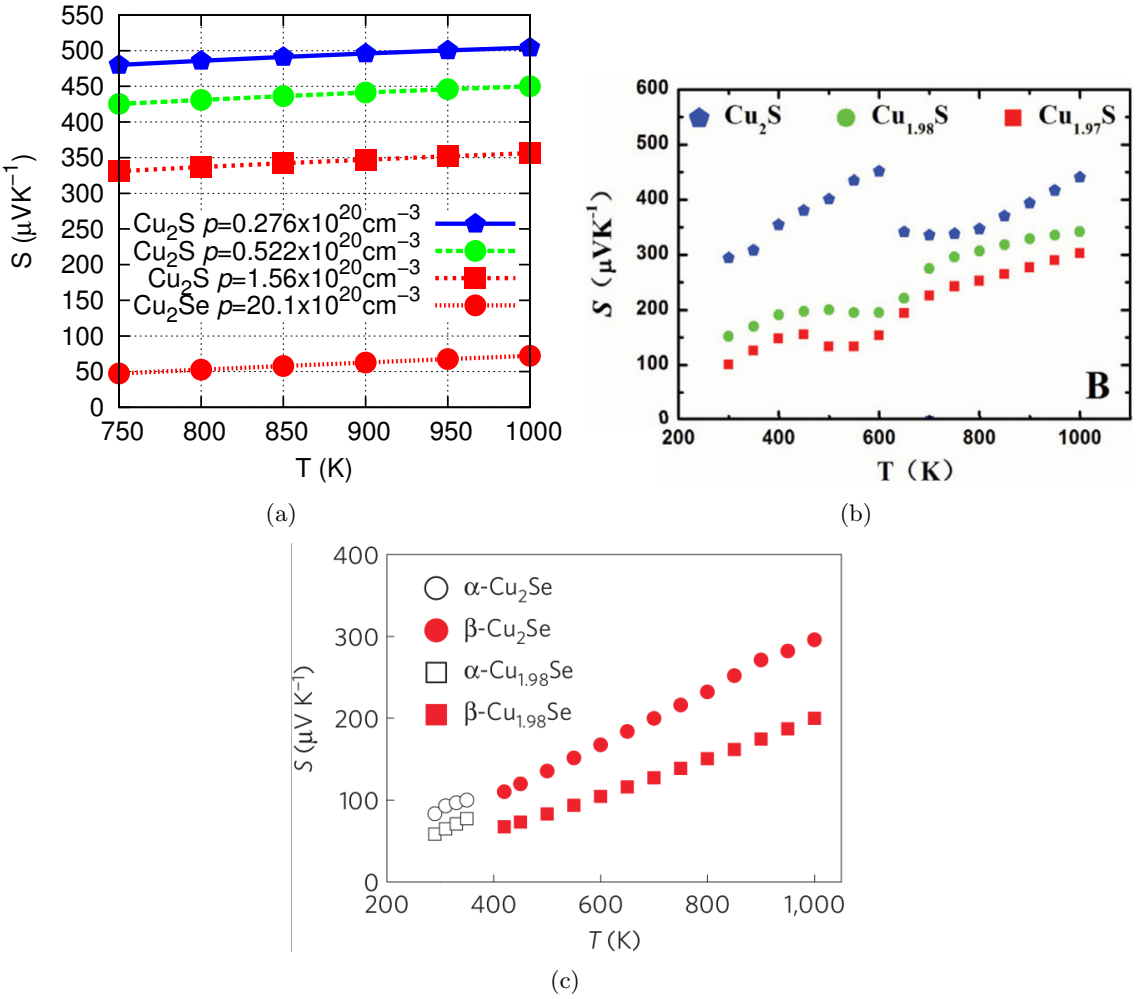

Figure 27: Variation of Seebeck coefficients with temperature in Cu_2S and Cu_2Se calculated from (a) theory with fixed hole concentrations and experimentally in (b) and (c). (b) and (c) are respectively taken directly from References [36] and [38]. We use the same experimental symbols and color schemes for comparison where possible.

Cu_2S and Cu_2Se. The few studies which actually do include the all-important effect of real life Cu disorder lack details in potentially high interest areas such as the thermoelectric effect which Cu_2S and Cu_2Se are most well known for. In response, we have provided here, a comprehensive study of the electronic and thermoelectric properties of hexagonal and cubic Cu_2S and cubic Cu_2Se, including a description of how we mimic the real life effect of Cu disorder in these structures. In these materials, either S or Se atoms form an ordered crystalline sublattice but Cu atoms form a separate disordered sublattice. We elaborated upon a first-principles random structure search method for finding energetically stable structures of hexagonal and cubic Cu_2S and cubic Cu_2Se exhibiting Cu disorder. We then discussed the electronic structures of hexagonal and cubic Cu_2S and cubic Cu_2Se based on first-principles calculations on each of their four lowest energy structures. We note that Cu disorder opens up a band gap in all of these materials. Bader charge analysis indicated that Cu-S/Se bonding in these compounds have covalent features and so not completely ionic. An analysis of their electronic density of states further revealed that their valence bands close to the valence band edge are composed predominantly of nonbonding Cu-d orbitals. Electronic density of states slightly further below this region are composed mainly of Cu-d and S or Se-p bonding orbitals. This large contribution of typically inert Cu-d orbitals results in noticeably flat bands close to the valence band edge. This in turn results in hexagonal and cubic Cu_2S and cubic Cu_2Se having notably large Seebeck coefficients which we calculated using Boltzmann transport theory. Hexagonal Cu_2S can attain a Seebeck coefficient of around $200\mu VK^{-1}$ up to hole concentrations of around $10^{20}cm^{-3}$ while both cubic Cu_2S and Cu_2Se can do so up to even higher hole concentrations of $3 \times 10^{20}cm^{-3}$. This agrees well with experiment. Moreover, the layered structure of hexagonal Cu_2S lowers electrical conductivity by an order of magnitude in the layer direction which contributes to only a slightly larger Seebeck coefficient also in the layer direction. We also calculated the hole concentration for optimum power factor in hexagonal Cu_2S to be in the range of $3\times10^{20}cm^{-3}$ to $5\times10^{21}cm^{-3}$. For cubic Cu_2S and Cu_2Se, we predict the hole concentrations corresponding to optimum power factor to be $5 \times 10^{20}cm^{-3}$ and $8 \times 10^{20}cm^{-3}$ respectively. Overall, we find that the optimized structures for cubic Cu_2S and Cu_2Se give more precise

results amidst Cu disorder than hexagonal Cu_2S because of their more isotropic structural nature.

CHAPTER V

MOLECULAR DYNAMICS SIMULATION OF COPPER DIFFUSION IN CUBIC COPPER SULFIDE AND CUBIC COPPER SELENIDE

5.1 Introduction

In the previous chapter, we evaluated the thermoelectric power factors of copper sulfide and copper selenide using a combination of Boltzmann transport theory and first-principles electronic structure calculations. Our results are in line with experimental evidence stating that both copper sulfide and copper selenide, being able to achieve ZT values of 1.7 and 1.5 respectively, are potential high performance thermoelectric materials.[36, 38] However, we note that their exceptional thermoelectric efficiencies are not so much due to their power factors but more so because of their unusually low thermal conductivities. The thermal conductivities of copper sulfide and copper selenide are both well below $1\mathrm{Wm}^{-1}\mathrm{K}^{-1}$ at temperatures of around 1000K.[36, 38] The origin of their low thermal conductivities is attributed to their highly mobile, to the point of being liquid-like, Cu atoms at high temperatures.[36, 38] At temperatures close to 1000K, both copper sulfide and copper selenide are in their cubic phases where S and Se atoms vibrate about well defined crystalline FCC lattice sites while the Cu atoms are free to diffuse through the S or Se sublattice. This phenomenon makes copper sulfide and copper selenide similar to the more well known superionic conductors. However, as Bader charge analysis in the previous chapter reveals, their respective Cu-S and Cu-Se bonds are more covalent than ionic in nature which is why they are referred to as a solid-liquid hybrid instead of superionics.[36, 43]

Recently, Wang used first-principles molecular dynamics simulations to demonstrate that, similar to regular superionics, Cu atoms in copper sulfide (Cu_2S) exhibit fast diffusion within a crystalline S lattice. Wang's results pertain specifically to the β phase of

Cu_2S where the S atoms are organized in a hexagonal lattice. Wang calculated the diffusion coefficient of Cu in this case to be $2.2\times10^{-6}cm^2s^{-1}$. This diffusion coefficient is most impressive not because it is high but rather because it is achievable at a relatively low 450K.[43] Earlier experimental results concerning the Cu diffusion coefficients in copper sulfie and copper selenide have been carried out but at lower temperatures of under 350K.[133, 134, 135] Nevertheless, they generally lend support to theoretical results by Wang.[43] Rickert and Wiemhöffer [134] discovered Cu diffusion coefficients ranging from $1\times10^{-7}cm^2s^{-2}$ to $6\times10^{-6}cm^2s^{-2}$ for copper sulfide at 333K. Tinter and Wiemhöffer [133] found the diffusion coefficient of Cu in copper selenide to be between $4.3\times10^{-7}cm^2s^{-2}$ to $2.4\times10^{-6}cm^2s^{-2}$ at 293K. Danilkin *et al.* performed the most recent study and found the self-diffusion coefficient of Cu in copper selenide to be as high as $6.1\times10^{-5}cm^2s^{-1}$ but stopped short of calculating the chemical diffusion coefficient of Cu.[133]

So far, information regarding the high temperature diffusive behaviour of Cu in copper sulfide and copper selenide and how this relates to their structural properties is lacking. It is expected that the Cu diffusion rate will be significantly higher at temperatures of 1000K and this will likely have important implications in the development of high temperature thermoelectric materials.[36, 38] In this chapter, we study Cu diffusion in copper sulfide and copper selenide along with their structural and vibrational properties using first-principles molecular dynamics simulation at 900K. We also analyse how these results change when copper deficiencies are introduced.

5.2 First-principles Molecular Dynamics Simulation Details

The structural details of cubic Cu_2S and cubic Cu_2Se are described in the previous chapter. We use the most energetically stable structures cubic Cu_2S and cubic Cu_2Se obtained from a random structure search, also described in the previous chapter, to begin our MD simulation. Each MD simulation starts at 0K and the temperature is gradually ramped up to 900K over a period of 2ps. Next follows an equilibration period of 30ps at 900K. No data is collected during this 30ps equilibration period and we describe below how we check that equilibrium

has been achieved at the end of it. After equilibration, we run the simulation for a final 50ps during which we collect atomic trajectory data for analysis. To study the effect of Cu deficiencies, we remove one random Cu each from the most energetically stable Cu_2S and Cu_2Se optimized structures and re-optimize them in VASP before repeating the MD simulation as just described. Recall that we use $2 \times 2 \times 2$ conventional FCC supercells in each case where there are 96 Cu and 64 S or Se atoms in total. Therefore, the removal of one Cu atom from Cu_2S and Cu_2Se gives us $Cu_{1.97}S$ and $Cu_{1.97}Se$.

The entire MD simulation described above is carried out in the formalism of density functional theory (DFT) using VASP.[96, 97, 98, 99] In the context of DFT, we use the generalized gradient approximation (GGA) [122, 123] for the exchange-correlation energy functional and the projector augmented wave (PAW) [71, 72] pseudopotentials. Due to the large size of our $2 \times 2 \times 2$ simulation supercells, we only sample the Brillouin zone at the Γ point. Each simulation timestep is 1fs long and we implement the canonical NVT ensemble using the Nóse-Hoover thermostat to maintain a constant temperature.[79, 80] Forces which determine the atomic trajectories are calculated from first-principles using the Hellmann-Feynmann theorem.[58, 73, 74] Atomic trajectories themselves are updated using the Verlet algorithm.[136].

5.2.1 Checking for Equilibrium

Before we begin collecting data, it is important to verify that a system is in equilibrium. We do this by running separate simulations of the system under the constraints of the micro-canonical NVE ensemble. Simply put, we will remove the constant temperature constraint and see how the temperature changes over time. In this situation, a clear indication that the system is already in equilibrium will be its ability to still maintain a relatively constant temperature over a substantial period of time.

Below in Fig. 28, we show how the temperatures of our $Cu_{2-x}S$ and $Cu_{2-x}Se$ systems vary under the microcanonical NVE constraints for 10ps directly after the 30ps equilibration period. Clearly, their temperatures fluctuate about a constant level over 10ps and this

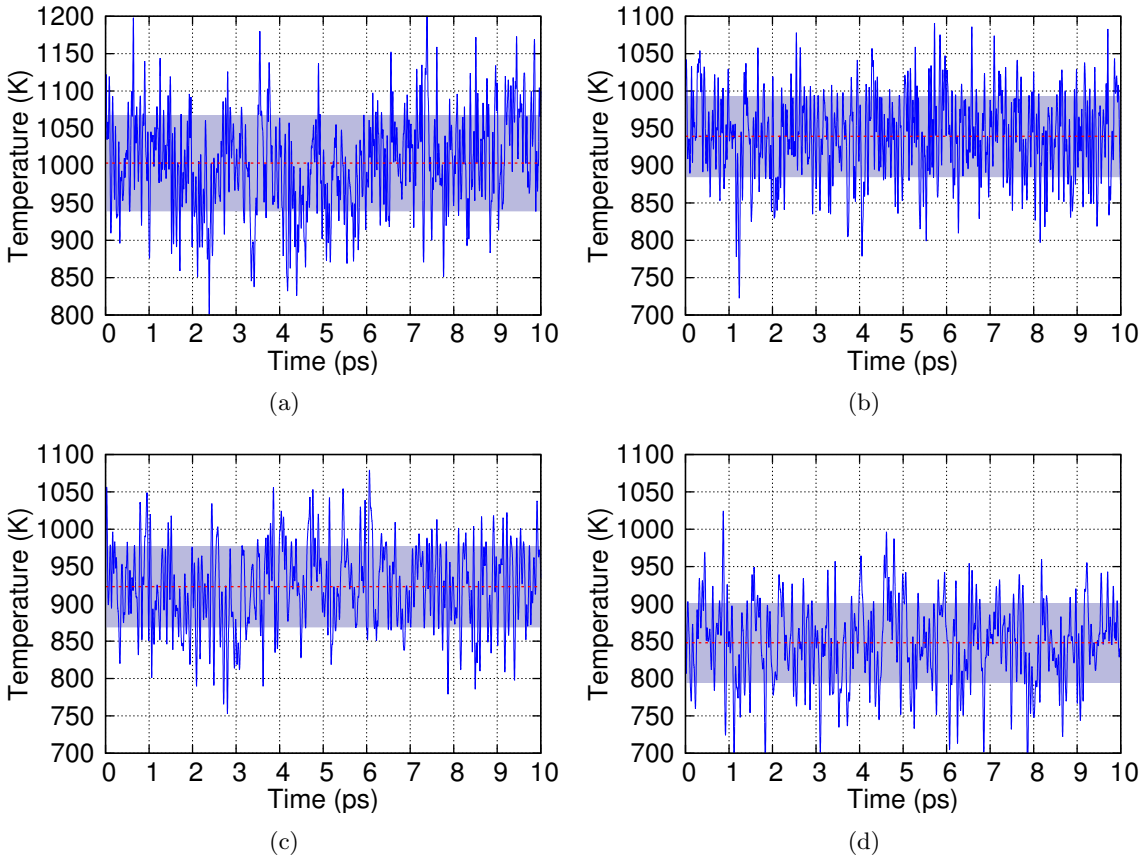

Figure 28: Temperature profiles for (a) Cu_2S, (b) $Cu_{1.97}S$, (c) Cu_2Se and (d) $Cu_{1.97}Se$ from ab-initio molecular dynamics simulation at 900K under constraints of the microcanonical NVE ensemble over 10ps. The mean temperature in each plot is indicated by the red dashed line while the range of the standard deviation of temperature is shaded.

indicates that they are already in equilibrium at the start of their respective NVE simulations. We record the mean and standard deviation of temperature for each of these 10ps long NVE simulations in Table 12.

5.3 Temperature Fluctuations During Simulations

In Fig. 29, we show how temperature varies in cubic $Cu_{2-x}S$ and $Cu_{2-x}Se$ over 50ps following the 30ps equilibration under the canonical NVT ensemble. We collect atomic trajectory data for analysis during this 50ps time frame and discuss the various analyses which we perform in the following sections. In Table 13, we list the mean and standard deviation of temperature for each system over their respective 50ps long simulations. Recall that in the canonical ensemble, temperature fluctuations are normal and the expected standard

Table 12: Temperature data for $Cu_{2-x}S$ and $Cu_{2-x}Se$ ($x = 0, 0.03$) from ab-initio molecular dynamics simulation at 900K under constraints of the microcanonical NVE ensemble over 10ps.

	Initial T (K)	Mean T (K)	Standard Deviation of T (K)
Cu_2S	1077	1000	60
$Cu_{1.97}S$	1005	940	50
Cu_2Se	923	920	50
$Cu_{1.97}Se$	887	850	50

Table 13: Temperature data for $Cu_{2-x}S$ and $Cu_{2-x}Se$ ($x = 0, 0.03$) from ab-initio molecular dynamics simulation at 900K under constraints of the canonical NVT ensemble over 50ps.

	Initial T (K)	Mean T (K)	Standard Deviation of T (K)
Cu_2S	1076	900	60
$Cu_{1.97}S$	1003	900	80
Cu_2Se	921	900	70
$Cu_{1.97}Se$	886	900	70

deviation in temperature is $\sigma_T = \sqrt{\frac{2}{3N}}T$.[78] Since we have 96 atoms in our simulation at 900K, we have $\sigma_T = 75$K. This is entirely in accordance with our data in Table 13.

5.4 Pair Correlation Functions

The partial pair correlation functions

$$g_{\alpha\beta}(r) = \frac{1}{N_\alpha \rho_\beta} \left\langle \sum_{i=1}^{N_\alpha} \sum_{j=1}^{N_\beta} \delta(\vec{r} + \vec{r}_i - \vec{r}_j) \right\rangle . \tag{146}$$

tell us much about structure and bonding within cubic $Cu_{2-x}S$ and $Cu_{2-x}Se$.[76, 77, 78] We describe how to deal with the 3D Dirac Delta function numerically in Chapter 1. Recall also that $g_{\alpha\beta}(r)$ gives us a measure of the probability of finding an atom of species β around a reference atom of species α. We show in Fig. 30 the pair correlation functions between the various constituents of cubic $Cu_{2-x}S$ and $Cu_{2-x}Se$. In Fig. 30, we arbitrarily show $g(r)$ for r ranging from 0 to 10Å . However, note that $g(r)$ is actually valid for $0 \leq r \leq \frac{a}{2}$ where a is the length of one side of the relevant cubic supercell. This is because if atom β is separated from reference atom α along a lattice vector direction by distance $x \geq 0.5$ in direct coordinates, periodic boundary conditions ensure that there is an identical β atom separated

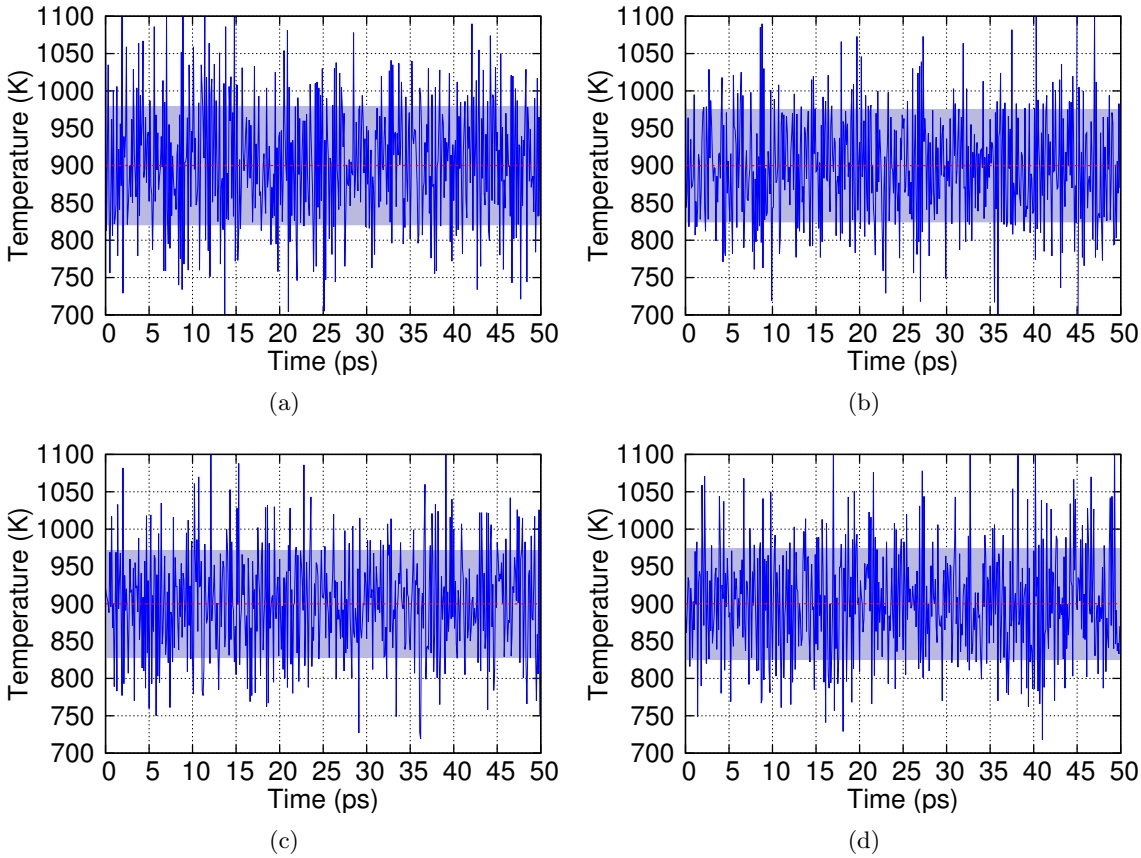

Figure 29: Temperature profiles for (a) Cu_2S, (b) $Cu_{1.97}S$, (c) Cu_2Se and (d) $Cu_{1.97}Se$ from ab-initio molecular dynamics simulation at 900K under constraints of the canonical NVT ensemble. The mean temperature in each plot is indicated by the red dashed line while the range of the standard deviation of temperature is shaded.

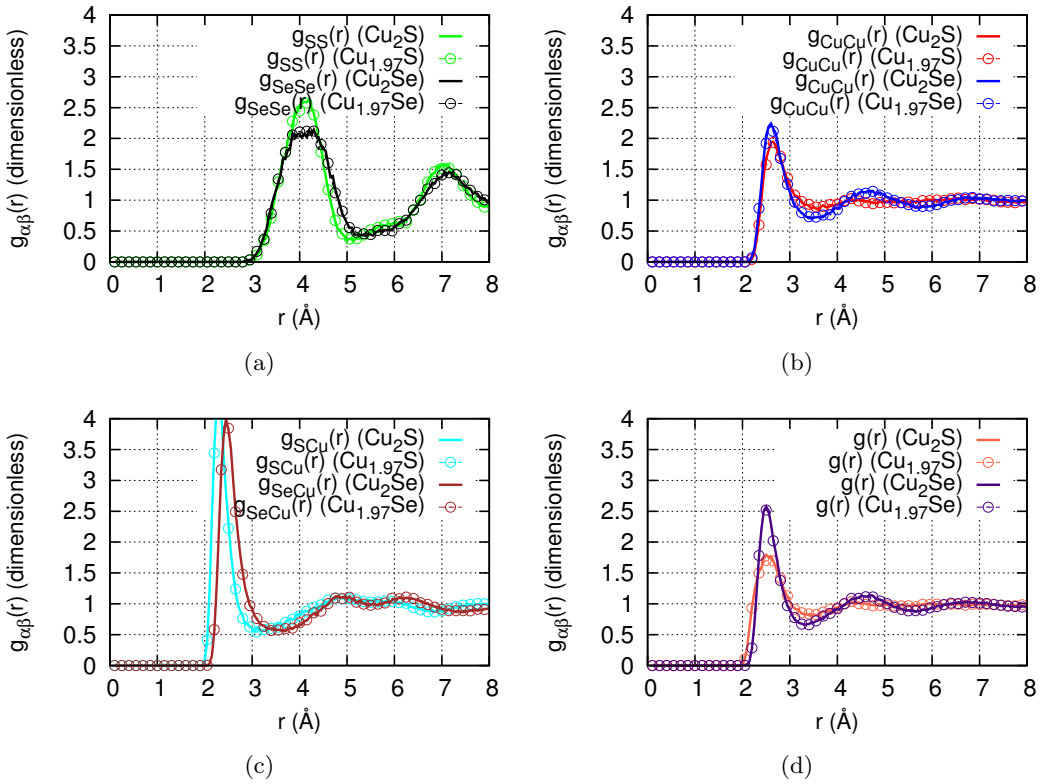

Figure 30: (a), (b) and (c) are the partial pair correlation functions $g_{\alpha\beta}(r)$between pairs of S, Se and Cu atoms of $Cu_{2-x}S$ and $Cu_{2-x}Se$ ($x = 0, 0.03$) from ab-initio molecular dynamics simulation at 900K. (d) is the total pair correlation function found by combining (a), (b) and (c).

from atom α by only $1.0 - x$. Each pair correlation curve is averaged over trajectory data separated by 100fs or 100 time steps over 50ps. In searching for nearest neighbours around each reference atom, care is taken to also include those neighbours which are beyond the periodic boundaries of the supercell.

From Fig. 30, we first note that Cu deficiencies barely affect the pair correlation functions. Hence, we expect that such minor deficiencies will not drastically affect the structural properties of cubic $Cu_{2-x}S$ and $Cu_{2-x}Se$. From experiments, we know that Cu deficiencies cause substantial differences in the observed thermoelectric properties.[36, 38]. Since the Cu deficiencies do little to change structural properties, we attribute these experimentally observed differences to the increase in p type doping which naturally accompanies the increase in Cu deficiencies.

Examining $g_{SS}(r)$ and $g_{SeSe}(r)$, we see that there are very distinct peaks and troughs.

This confirms the expectation that S and Se adopt an ordered crystalline sublattice. Both $g_{SS}(r)$ and $g_{SeSe}(r)$ peak at about 4.1Å which is close to the expected S-S and Se-Se nearest neighbour distance given the lattice constants which we use in our cubic $Cu_{2-x}S$ and $Cu_{2-x}Se$ structural models. We also note that these peaks are relatively broad which due to thermal oscillations. The peak of $g_{SeSe}(r)$ is particularly flat which is indicative of Se atoms undergoing larger oscillations about their mean position. This can be understood by considering the larger size of Se in comparison to S, which requires that Se make larger displacements, in order for Cu to diffuse through the Se sublattice in cubic $Cu_{2-x}Se$.

$g_{CuCu}(r)$, $g_{SCu}(r)$ and $g_{SeCu}(r)$ all have a single peak which then decays to unity. Since we already know that S and Se atoms have crystalline order, the single peaks all mean that there is some short range structure of Cu around the S, Se or other Cu atoms. However, in all cases, the decay to unity after the initial peak without any further distinct peaks or troughs indicates that Cu quickly appears disordered beyond a certain minimum range of around 2.5Å. This behaviour, being very characteristic of a typical liquid, confirms the expected liquid-like nature of the Cu atoms.

Comparing the $g_{CuCu}(r)$ between cubic $Cu_{2-x}S$ and $Cu_{2-x}Se$, we find that $g_{CuCu}(r)$ of $Cu_{2-x}Se$ has small but nevertheless clear oscillations after the initial peak while $g_{CuCu}(r)$ for $Cu_{2-x}S$ has smooth decay to unity. These oscillations imply that there is substantially more backscattering of Cu in $Cu_{2-x}Se$, which again may be expected since Se is larger in size than S. The backscattering in this case is more commonly referred to as the cage effect.

$g_{SCu}(r)$ and $g_{SeCu}(r)$ have the sharpest and tallest peak of all the partial pair correlation functions. This implies that S-Cu and Se-Cu interactions are the strongest and most important types of interactions as compared to the other S, Se and Cu self-interactions. Also, the primary peaks of $g_{SCu}(r)$ and $g_{SeCu}(r)$ are very clearly separated from each other by 0.15Å. This shows that the ideal separation between Se-Cu pairs is about 5% larger than that between S-Cu pairs.

We combine the partial pair correlation functions using the Faber-Ziman formalism

Table 14: Coordination numbers between pairs of S, Se and Cu atoms in cubic $Cu_{2-x}S$ and $Cu_{2-x}Se$ ($x = 0, 0.03$) from ab-initio molecular dynamics simulation at 900K.

	$N_{SS/SeSe}$	$N_{(S/Se)Cu}$	$N_{Cu(S/Se)}$	N_{CuCu}
Cu_2S	12.0	6.1	3.1	7.0
$Cu_{1.97}S$	12.1	6.0	3.1	6.9
Cu_2Se	12.5	8.1	4.0	6.1
$Cu_{1.97}Se$	12.6	7.7	4.0	6.0

[76, 137] to give the total pair correlation function

$$g(r) = \frac{\sum_{\alpha,\beta} x_\alpha x_\beta b_\alpha b_\beta g_{\alpha\beta}(r)}{\sum_{\alpha,\beta} x_\alpha x_\beta b_\alpha b_\beta}. \tag{147}$$

In the above equation, x_α is the molar fraction and b_α is the scattering amplitude for species α. To make our results relevant to neutron scattering experiments, we choose to use neutron scattering lengths Ref. [138] as the b_α. For S, Se and Cu, the b_α are 2.847fm, 7.970fm and 7.718fm respectively. We show the total radial distribution function $g(r)$ also in Fig. 30. We see that $g(r)$ most strongly resembles $g_{CuCu}(r)$ and $S_{CuCu}(k)$. This is reasonable since Cu has the largest molar fraction of all.

5.4.1 Coordination Numbers

The coordination numbers

$$N_{\alpha\beta} = \int_0^{r_{min}} 4\pi r^2 g_{\alpha\beta}(r)\rho_\beta dr \tag{148}$$

between S, Se and Cu pairs in cubic $Cu_{2-x}S$ and $Cu_{2-x}Se$ may be estimated by integrating the relevant partial pair correlation functions.[76, 77, 78] We list these coordination numbers in Table 14.

From Table 14, we see that S (Se) are coordinated to about 12 other S (Se) atoms in $Cu_{2-x}S$ ($Cu_{2-x}Se$). This is expected since each atom in a perfect FCC crystal lattice has exactly 12 nearest neighbours.

In $Cu_{2-x}S$, each Cu is coordinated to 3 S neighbours on average. Since we know that S atoms are in FCC sites, we conclude that Cu atoms in $Cu_{2-x}S$ spend a good amount of time near the center of the triangular faces formed by groups of four nearest S neighbours. This is consistent with the fact that Cu atoms prefer 192*l* sites based on XRD results.[53]

In $Cu_{2-x}Se$, each Se is coordinated to around 8 Cu atoms while each Cu is coordinated to 4 S neighbours on average. Recall from Fig. 18 that $8c$ sites are at the center of the tetrahedra formed by groups of four nearest S neighbours and each S also has 8 equally spaced $8c$ nearest neighbour sites around it. Therefore, our observations here strongly support the experimental findings that Cu atoms in $Cu_{2-x}Se$ have a strong preference for visiting the $8c$ tetrahedral.[57]

Overall, we note that Cu atoms in $Cu_{2-x}S$, with a preference for being within the triangular planes formed by neighbouring S atoms, tend to clump up and hinder S atoms from sharing a similar set of Cu neighbours. This explains why $N_{SCu} < N_{SeCu}$ and also why N_{CuCu} is larger in $Cu_{2-x}S$ than it is for $Cu_{2-x}Se$. The stronger cage effect in $Cu_{2-x}Se$, due to the larger size of the Se atoms, is thus seen to force the Cu atoms in $Cu_{2-x}Se$ into a more open structure.

5.4.2 Static Structure Factors

We obtain the partial static structure factors by Fourier transforming the partial pair correlation functions according to

$$S_{\alpha\beta}(k) = 1 + 4\pi\rho \int \frac{sin(kr)g_{\alpha\beta}(r)}{kr} r^2 dr. \tag{149}$$

Static structure factors are highly relevant since they are directly accessible from X-ray or neutron scattering experiments. In fact, pair correlation functions are calculated in experiments by first calculating the static structure factors and then Fourier transforming them into the pair correlation functions. This is opposite to the procedure applied in molecular dynamics simulation which we describe here.[76]

In the above integration for calculating $S_{\alpha\beta}(k)$, the integration over r ideally ranges from 0 to ∞. However, we only have a finite sized system and with r ranging from 0 to half the length of any side of the relevant cubic supercell $\frac{a}{2}$. This finite maximum range of r places a limit on the minimum range of k below which $S_{\alpha\beta}(k)$ cannot be calculated reliably. We use simple quantum mechanical ideas to estimate this minimum k_{min}. For a particle in a 1D flat bottom potential well of width L with infinitely high walls, the smallest possible wave vector is $\frac{2\pi}{L}$. Thus, we use the approximation $k_{min} \sim \frac{2\pi}{a/2} \sim 1\text{Å}^{-1}$.

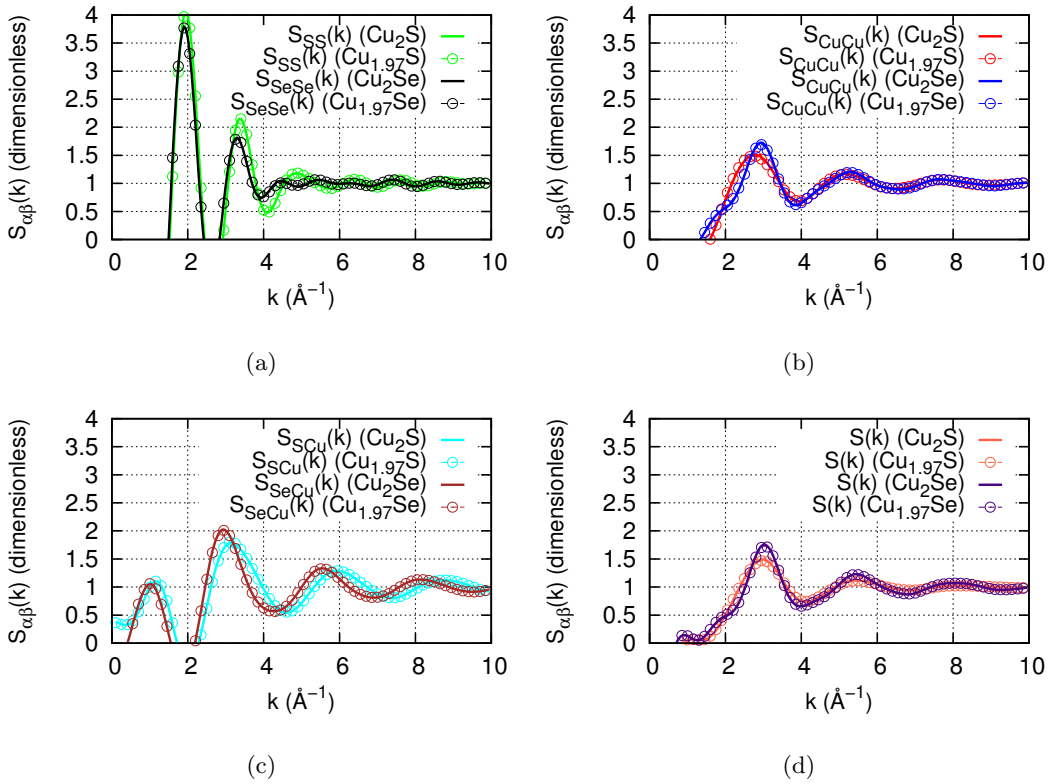

Figure 31: Partial static structure factors $S_{\alpha\beta}(k)$ between pairs of S, Se and Cu atoms of $Cu_{2-x}S$ and $Cu_{2-x}Se$ ($x = 0, 0.03$) from ab-initio molecular dynamics simulation at 900K. (d) is the total static structure factor found by combining (a), (b) and (c).

The total static structure factor may be calculated either by Fourier transforming the total pair correlation function $g(r)$ or by applying the Faber-Ziman formalism [76, 137]

$$S(k) = \frac{\sum_{\alpha,\beta} x_\alpha x_\beta b_\alpha b_\beta S_{\alpha\beta}(k)}{\sum_{\alpha,\beta} x_\alpha x_\beta b_\alpha b_\beta}. \tag{150}$$

Both methods yield identical results. We show the various partial and total static structure factors in Fig. 31.

5.5 Mean Squared Displacement of Cu

The mean squared displacement (MSD) gives a clear picture of atomic diffusion occurring within cubic $Cu_{2-x}S$ and $Cu_{2-x}Se$. The MSD $\langle \Delta r_\alpha(t)^2 \rangle$ for atomic species α is given by

$$\langle \Delta r_\alpha(t)^2 \rangle = \left\langle \frac{1}{N_\alpha} \sum_{i=1}^{N_\alpha} |\vec{r}_i(t) - \vec{r}_i(0)|^2. \right\rangle \tag{151}$$

N_α is the number of atoms of species α and $\vec{r}_i(t)$ represents the coordinates of individual atoms of species α at time t during the simulation.

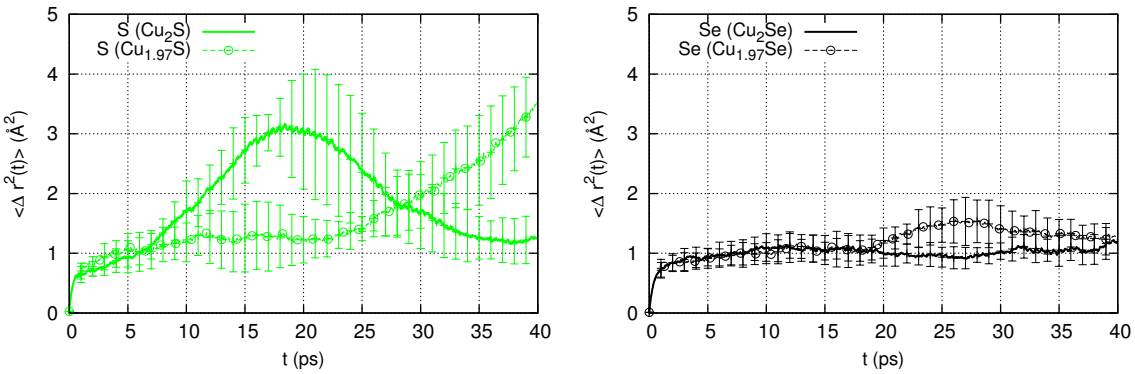

Figure 32: Mean squared distance $\langle \Delta r^2(t) \rangle$ moved by S and Se atoms from cubic (a) $Cu_{2-x}S$ and (b) $Cu_{2-x}Se$ as a function of time from ab-initio molecular dynamics simulation at 900K.

The MSDs for S, Se and Cu in cubic $Cu_{2-x}S$ and $Cu_{2-x}Se$ are depicted in Figs. 32 and 33. Each of the MSD curves are averaged over twenty 40ps long intervals. The origins of each interval are separated from each other by 500fs. We choose an origin shift of 500fs between separate intervals because this is about the time it takes for atomic correlations to become insignificant. We will see this later in analysing the velocity autocorrelation functions in Fig. 34. Within each 40ps interval, atomic trajectories are sampled every 20fs. Of course, periodic boundary conditions cause sudden jumps in the $r_i(t)$ as atoms move through the supercell boundaries but we are careful to make the necessary corrections for this effect.

In Fig. 32, we see that the MSD of S and Se is insignificant over the entire 40ps interval. Over 40ps, they typically shift only between 1Å and 2Å from their original positions which is too minute to constitute actual diffusion. Rather, we interpret these values as the displacements of S and Se atoms as they oscillate about their mean FCC positions.

We show in Fig. 33 the MSD of Cu in cubic $Cu_{2-x}S$ and $Cu_{2-x}Se$.

From Fig. 33, it is clear that there is a nearly linear increase of the MSD of Cu atoms with time in both cubic $Cu_{2-x}S$ and $Cu_{2-x}Se$. Over the 40ps interval, the MSD of the various Cu typically reach roughly 100 $Å^2$ meaning that on average, Cu atoms can be expected to diffuse about 10Å over 40ps in cubic $Cu_{2-x}S$ and $Cu_{2-x}Se$.

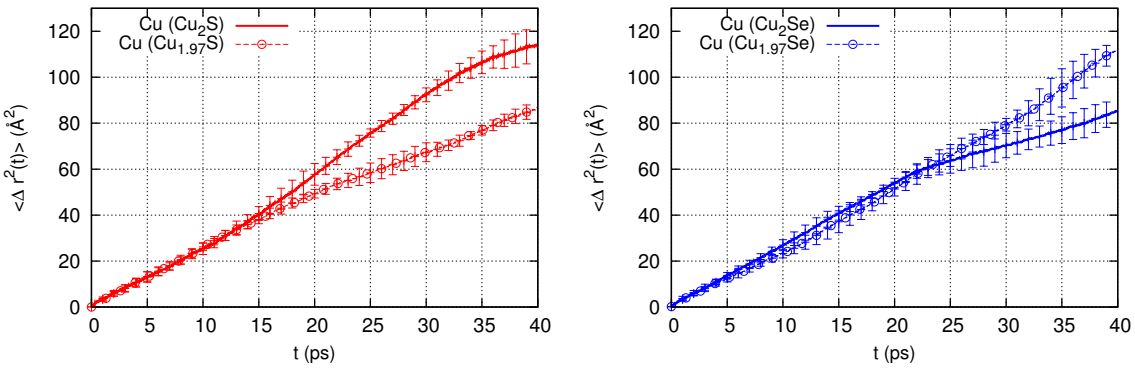

Figure 33: Mean squared distance $\langle \Delta r^2(t) \rangle$ moved by Cu atoms from cubic (a) $Cu_{2-x}S$ and (b) $Cu_{2-x}Se$ as a function of time from ab-initio molecular dynamics simulation at 900K.

Table 15: Diffusion coefficients of $Cu_{2-x}S$ and $Cu_{2-x}Se$ calculated using the mean squared displacements (D_{MSD}) and velocity autocorrelation functions (D_{VACF}) methods obtained from ab-initio molecular dynamics simulation at 900K.

System	D_{MSD} $(10^{-5}\text{cm}^2\text{s}^{-1})$	D_{VACF} $(10^{-5}\text{cm}^2\text{s}^{-1})$
Cu_2S	5.1	4.7
$Cu_{1.97}S$	3.9	3.9
Cu_2Se	3.9	3.8
$Cu_{1.97}Se$	4.6	4.5

5.5.1 Cu Diffusion Rates

We gain a more quantitative description of the Cu diffusion by analyzing the gradient of each MSD curve. Each gradient is proportional to the relevant diffusion coefficient D_{MSD} of Cu

$$D_{MSD} = \frac{1}{N_{dim}} \frac{\partial}{\partial t} \langle \Delta r^2(t) \rangle / (2N_{dim}). \tag{152}$$

N_{dim} refers to the dimensionality of the system which is 3 in all the cases we examine. We list the calculated Cu diffusion coefficients using this MSD method in Table 15. Table 15 also contains Cu diffusion coefficients D_{VACF} calculated from the velocity autocorrelation functions (VACFs) as a consistency check. We elaborate on the VACFs in and discuss how diffusion coefficients may be calculated from the VACFs in the next section. For now, we note that the diffusion coefficients calculated using the MSD and VACF methods consistently indicate the same trend.

The diffusion coefficients of Cu listed in Table 15 are highly significant. They are all

above $10^{-5}\text{cm}^2\text{s}^{-1}$ which is comparable to that of many compounds dissolved in water or organic solvents.[139, 140, 141, 142] We also note that the diffusion coefficients of Cu calculated here are an order of magnitude larger than the diffusion coefficient of Cu calculated by Wang in the case of hexagonal $Cu_{2-x}S$ at 450K via a similar molecular dynamics simulation.[43] We also see that Cu deficiencies have a significant effect on the diffusion coefficients in cubic $Cu_{2-x}S$ and $Cu_{2-x}Se$. Cu deficiencies result in a 15% increase in the Cu diffusion coefficient between Cu_2Se and $Cu_{1.97}Se$ since Cu deficiencies allow Se to be displaced more easily to facilitate Cu diffusion. In contrast, Cu_2S has a much lower Cu diffusion coefficient than $Cu_{1.97}S$ for reasons not yet understood.

5.6 Velocity Autocorrelation Functions

We analyse the dynamical processes within cubic $Cu_{2-x}S$ and $Cu_{2-x}Se$ through the velocity autocorrelation functions (VACFs) of their constituents. The VACF for species α is given by

$$Z_\alpha(\tau) = \frac{\left\langle \sum_{i=1}^{N_\alpha} \vec{v}_\alpha(0) \cdot \vec{v}_\alpha(\tau) \right\rangle}{\left\langle \sum_{i=1}^{N_\alpha} \vec{v}_\alpha(0) \cdot \vec{v}_\alpha(0) \right\rangle}. \tag{153}$$

Here, τ is the time delay between signals. The angular brackets in the above equation denote an average over time origins, for which we use a separation of 10fs between origins. The VACFs for S, Se and Cu in cubic $Cu_{2-x}S$ and $Cu_{2-x}Se$ are shown in Fig. 34. They are all normalized by their respective zero delay VACF $\left\langle \sum_{i=1}^{N_\alpha} \vec{v}_\alpha(0) \cdot \vec{v}_\alpha(0) \right\rangle$ such that a value of 1 (-1) denotes perfect correlation (anticorrelation).

The VACF of S in cubic $Cu_{2-x}S$ is very clearly shows damped harmonic motion which is characteristic of a regular solid lattice. However, the motion of Cu atoms in $Cu_{2-x}S$ is very heavily damped which is characteristic of a normal fluid. This is because the highly diffusive motion of Cu atoms in $Cu_{2-x}S$ counters oscillatory motion.

The VACF of Se atoms in cubic $Cu_{2-x}Se$ oscillates similarly to the VACF for S atoms in cubic $Cu_{2-x}S$. The main difference is that the motion of Se is more strongly damped, which may be attributed to their heavier mass. Interestingly, the Cu atoms in $Cu_{2-x}Se$ are heavily damped but still display some very slight oscillatory motion. This is likely due to

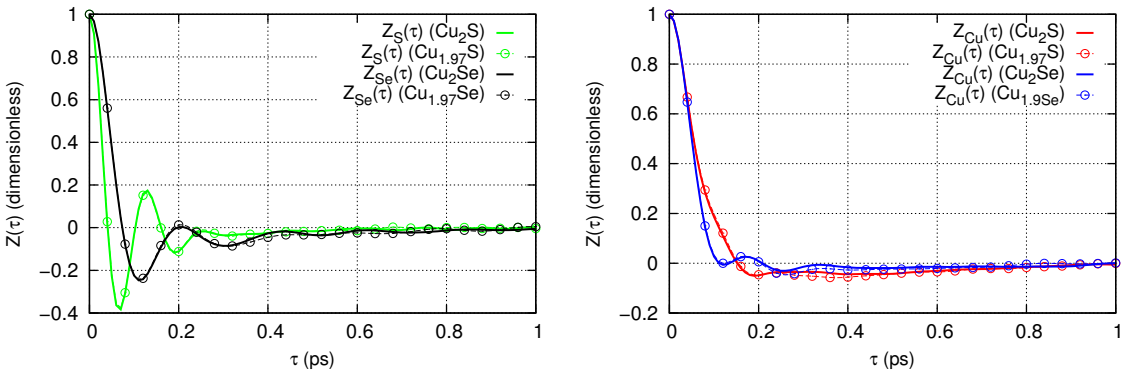

(a) (b)

Figure 34: (a) and (b) are the normalized velocity autocorrelation functions for S, Se and Cu atoms in $Cu_{2-x}S$ and $Cu_{2-x}Se$ ($x = 0, 0.03$). Results shown here are obtained from ab-initio molecular dynamics simulation at 900K. Error bars are too small to be distinguished from plot points.

the stronger cage effect for Cu atoms in $Cu_{2-x}Se$ which causes Cu atoms to be backscattered more than the Cu atoms in $Cu_{2-x}S$.

5.6.1 Cu Diffusion Rates

Earlier, we demonstrated how the diffusion coefficient is calculated from the MSD. However, the diffusion coefficient may alternatively be calculated from the VACF as

$$D_{VACF} = \int d\tau \langle \vec{v}(\tau) \cdot \vec{v}(0) \rangle. \tag{154}$$

This provides a good consistency check for the diffusion coefficients of Cu calculated previously using the MSD method. The diffusion coefficients of Cu in cubic $Cu_{2-x}S$ and $Cu_{2-x}Se$, calculated using the MSD and VACF methods, are listed and discussed in Table 15 in the previous section. We see that both methods consistently predict the same trend. We use a 10ps integration range in order to calculate D_{VACF} in each case. This is sufficient as we see that the VACFs all decay almost to 0 within 1ps.

5.6.2 Phonon Power Spectra

The Fourier transforms of the VACFs yield the phonon power spectra

$$\hat{Z}_\alpha(\omega) = \frac{1}{\sqrt{2\pi}} \int d\tau e^{i\omega\tau} Z_\alpha(\tau) \tag{155}$$

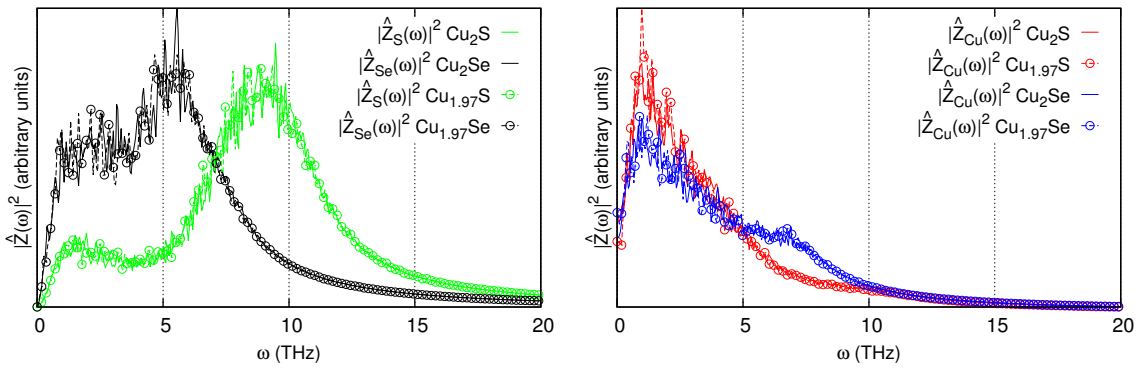

Figure 35: (a) and (b) are the normalized power spectra in $Cu_{2-x}S$ and $Cu_{2-x}Se$ ($x = 0, 0.03$) obtained by Fourier transforming the relevant velocity autocorrelation functions. The velocity autocorrelation functions are normalized by their value at $\tau = 0$ while the power spectra have been normalized by their areas. Results shown here are obtained from ab-initio molecular dynamics simulation at 900K.

which are directly proportional to the phonon density of states. We show the $|\hat{Z}_\alpha(\omega)|^2$ for S, Se and Cu in Fig. 35.

Let us first consider the power spectra of S and Se. Since they both form solid sublattices, their $|\hat{Z}_\alpha(\omega)|^2$ are both zero at $\omega = 0$. However, their is a clear difference in the location of their peaks, with $|\hat{Z}_\alpha(\omega)|^2$ for Se peaking first. This indicates that the Se sublattice is able to transmit more low frequency acoustic phonons than the S sublattice. Since it is acoustic phonons which are most dispersive, implying that they have higher phonon group velocities, we expect that the Se sublattice will be much more efficient at transmitting phonons or heat than the S sublattice. This is consistent with experimental results which show that $Cu_{2-x}Se$ has consistently higher thermal conductivity than $Cu_{2-x}S$.[36, 38]

The $|\hat{Z}_\alpha(\omega)|^2$ for Cu are generally similar in both $Cu_{2-x}S$ and $Cu_{2-x}Se$. Furthermore, $|\hat{Z}_\alpha(\omega)|^2$ of Cu in both cases is non-zero at $\omega = 0$. This is an indication of the presence of diffusive modes which is another signature of their liquid-like nature.[143] We do not expect the liquid-like Cu to contribute significantly to thermal transport in comparison to the solid S or Se sublattices since diffusive modes are not conducive for phonon transport.

Table 16: Bader charges of Cu, S and Se in $Cu_{2-x}S$ and $Cu_{2-x}Se$ ($x = 0.00, 0.03$) averaged over samples taken every 5ps over the 50ps molecular dynamics simulation at 900K. Standard errors are given.

	Cu_2S	$Cu_{1.97}S$	Cu_2Se	$Cu_{1.97}Se$
Cu Bader charge	10.611 ± 0.004	10.605 ± 0.005	10.728 ± 0.004	10.723 ± 0.006
S/Se Bader charge	6.778 ± 0.009	6.78 ± 0.01	6.544 ± 0.008	6.54 ± 0.01

5.7 Bader Charge Analysis

We begin with Bader charge analysis. Throughout the 50ps simulation, we calculate the average Bader charges on S, Se and Cu atoms in $Cu_{2-x}S$ and $Cu_{2-x}Se$ every 5ps. The mean and standard deviation of all ten of these calculations are presented in Table 16. Compared to the Bader charges calculated using optimized structures in Table 9 of the previous chapter, we find near perfect agreement even with Cu deficiencies, meaning that $Cu_{2-x}S$ and $Cu_{2-x}Se$ are still not completely ionic at 900K. We refer the reader back to Section 4.4 for a discussion on the significance of the Bader charges.

5.8 Electronic Structure

In the previous chapter, we analyzed the electronic structures of structurally optimized cubic Cu_2S and Cu_2Se shown in Figs. 22 and 23. In Figs. 36 and 37, we show for comparison, the electronic band structures and density of states of Cu_2S and Cu_2Se during the molecular dynamics simulation. These are are obtained at the 5ps, 15ps, 20ps and 50ps marks in the 50ps molecular dynamics simulation for each case. We shall refer to the molecular dynamics structures as the unoptimized structures.

The optimized electronic structures of cubic Cu_2S and Cu_2Se, as detailed in Section 4.5, are generally very similar to those of the unoptimized electronic structures so we only detail a few minor differences here. The most notable differences in the electronic band structures between the optimized (Figs. 22 and 23) and unoptimized structures (Figs. 36 and 37) are in the conduction bands. In the unoptimized structures, the conduction bands are more spaced apart with the lowest conduction band being significantly more dispersive, especially

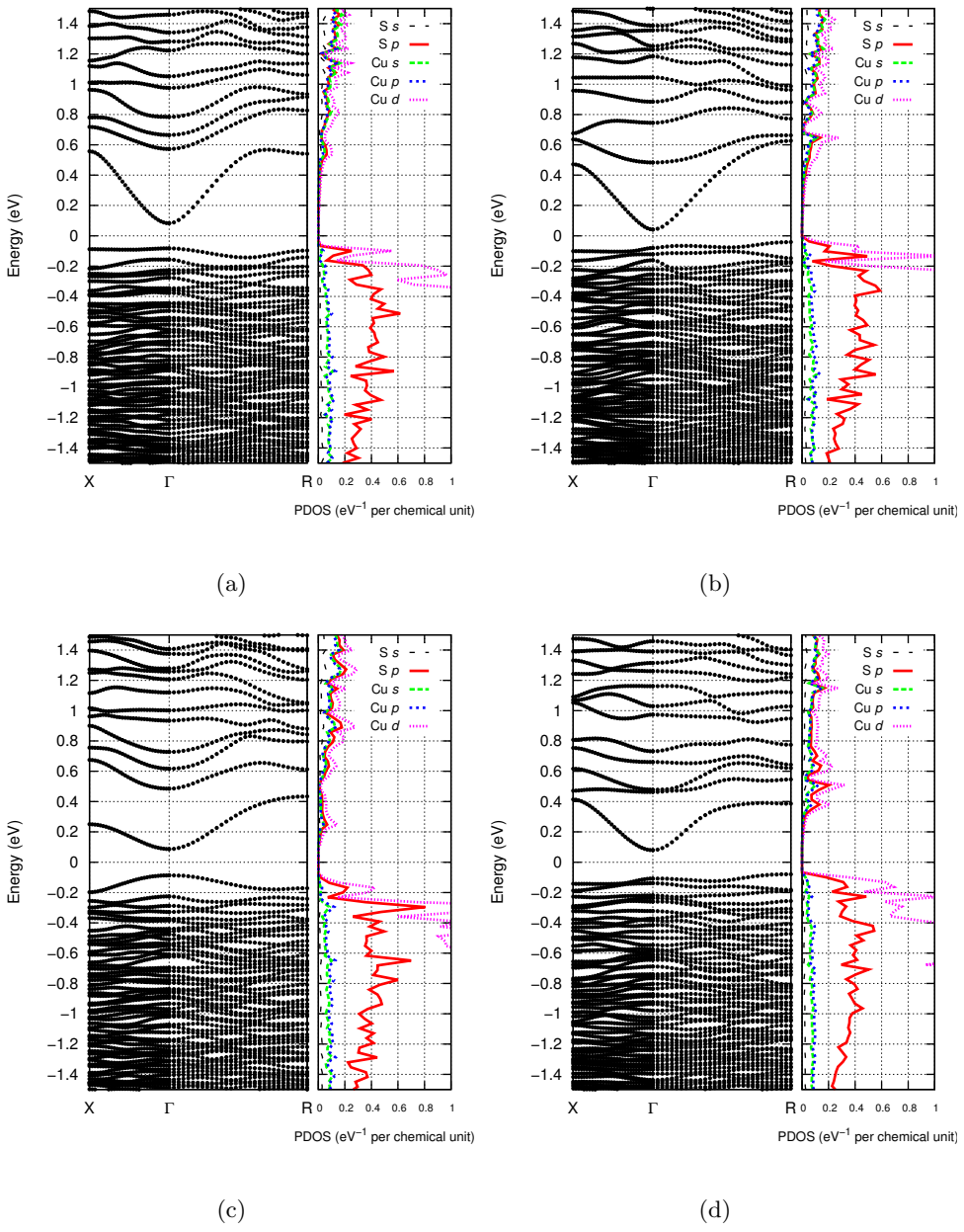

Figure 36: (a), (b), (c) and (d) are the electronic band structures and density of states of cubic Cu_2S from molecular dynamics simulation at 900K. They are taken at 5ps, 15ps, 20ps and 50ps during the simulation and arranged in that order. The zero of energy is set to the center of the band gap.

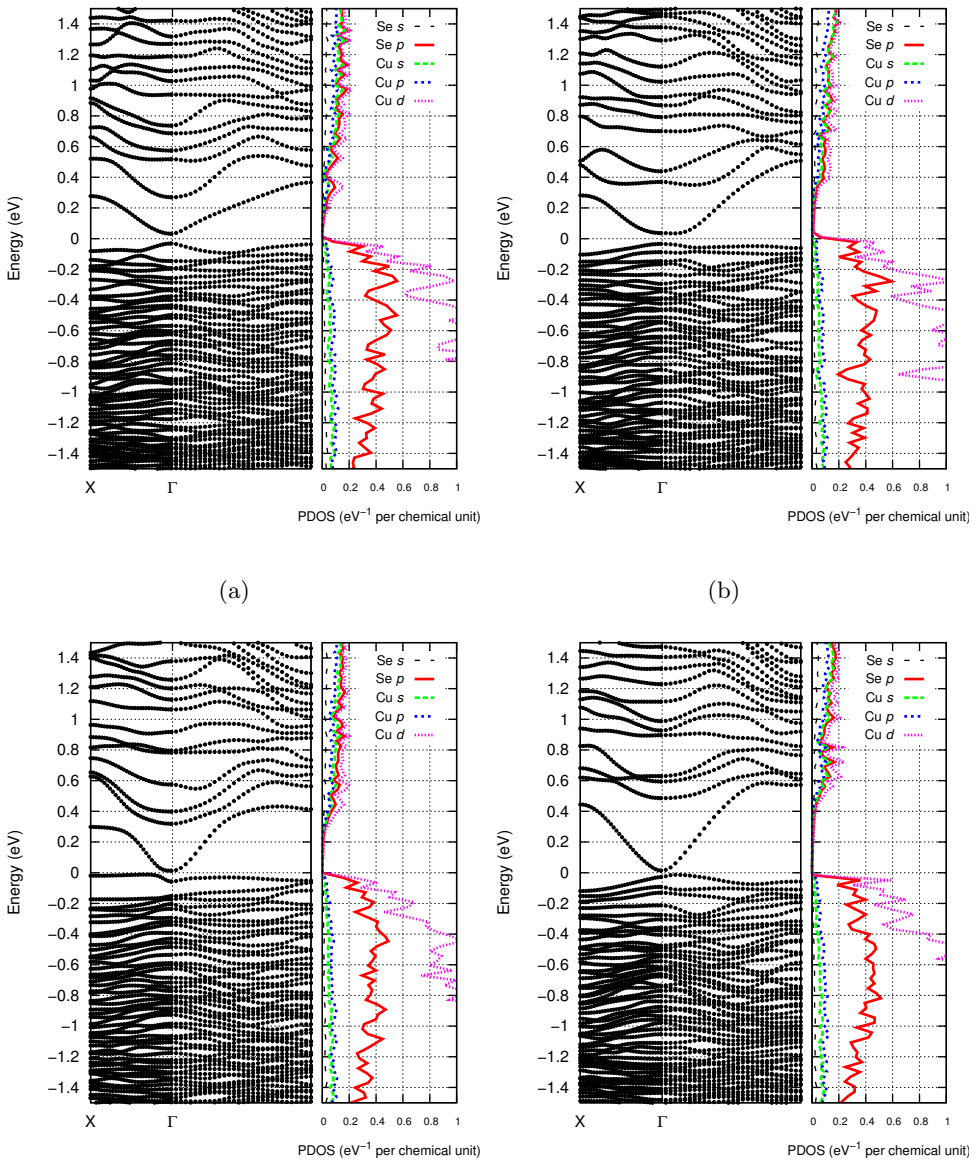

Figure 37: (a), (b), (c) and (d) are the electronic band structures and density of states of cubic Cu_2Se from molecular dynamics simulation at 900K. They are taken at 5ps, 15ps, 20ps and 50ps during the simulation and arranged in that order. The zero of energy is set to the center of the band gap.

in the case of Cu_2S. This results in smaller band gaps for the unoptimized structures. For Cu_2Se, the valence bands near the band edge of the unoptimized structures are also notably flatter in comparison to those in the optimized structures. The band gap of Cu_2Se during the molecular dynamics simulation is particularly small. We can relate this to how its Cu are coordinated to about four other Se atoms This implies tetrahedral bonding, making it similar to the antifluorite structure of Cu_2Se which we know has no gap. Only sufficient lattice distortion and Cu disorder during the MD simulation prevents this gap from vanishing completely.

5.9 Thermoelectric Properties

In Fig. 38, we show the thermoelectric properties of optimized and unoptimized cubic Cu_2S and Cu_2Se together. Unoptimized structures taken at various points in our MD simulations provide consistent results with those from optimized structures but only at hole concentrations greater than $4\times10^{19}\text{cm}^{-3}$. At lower hole concentrations, where bands close to the valence band edge have greater influence, the results begin to differ significantly, especially for Cu_2Se. This is because bands closer to the valence band edge are much more sensitive to structural differences. Seeing as how consistent the Seebeck coefficient is between optimized and unoptimized structures, we attribute the larger electrical conductivity differences between structures to the differences in electronic relaxation time which we do not calculate here. All in all, the MD results do not change our original conclusions drawn from the optimized structures of cubic Cu_2S and Cu_2Se detailed in Section 4.6.2. We still predict the hole concentrations corresponding to optimum power factor to be about $8\times10^{20}\text{cm}^{-3}$ in cubic Cu_2S and $5\times10^{20}\text{cm}^{-3}$ in cubic Cu_2Se. They are both also capable of maintaining very high Seebeck coefficients of over $200\mu\text{VK}^{-1}$ for hole concentrations as high as $3\times10^{20}\text{cm}^{-3}$.

5.10 Conclusions

At high temperatures approaching 1000K, Cu_2S and Cu_2Se each exist in a solid-liquid hybrid phase. Solid-liquid hybrid Cu_2S and Cu_2Se are very closely related to the more

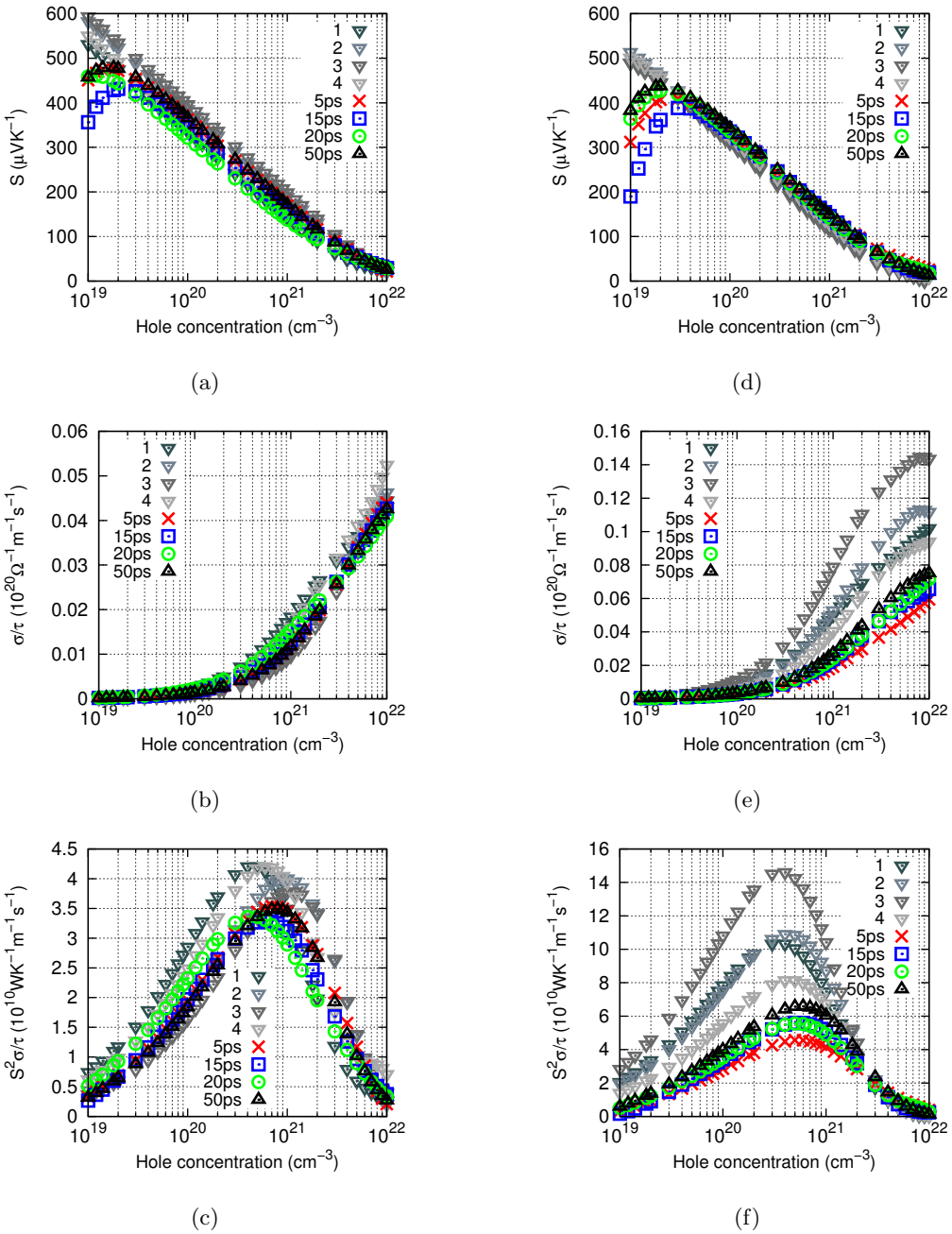

Figure 38: (a), (b) and (c) are the Seebeck coefficient, electrical conductivity and power factor for Cu_2S respectively. (d), (e) and (f) are the Seebeck coefficient, electrical conductivity and power factor for Cu_2Se respectively. For each set of results, grey shaded ∇ markers represent results from the lowest energy optimized structures (identical to Fig. 26) while red, blue, green and black markers represent results from structures at 5ps, 15ps, 20ps and 50ps after equilibration in the 900K molecular dynamics simulation.

well-studied superionic conductors but are fundamentally different because Cu-S and Cu-Se bonds have more covalent than ionic characteristics. Nevertheless, they share similar uses and properties. In Cu_2S and Cu_2Se, it is the S or Se atoms which form a crystalline sublattice and the Cu atoms in diffuse so rapidly that they are considered liquid-like. The solid-liquid hybrid nature of Cu_2S and Cu_2Se is of immense interest in the development of thermoelectric devices. The liquid-like Cu sublattice promotes phonon scattering and confers an unusually low thermal conductivity to Cu_2S and Cu_2Se while the crystalline S or Se sublattice ensures that good electrical characteristics are preserved for an overall high thermoelectric efficiency ZT.

We described in this chapter the use of first-principles molecular dynamics to evaluate the structural and vibrational properties of $Cu_{2-x}S$ and $Cu_{2-x}Se$ ($x = 0.00, 0.03$) at 900K. Pair correlation functions between various S, Se and Cu atomic pairs provided strong evidence for the coexistence of liquid Cu with a crystalline S or Se FCC sublattice in $Cu_{2-x}S$ and $Cu_{2-x}Se$. They also indicated that Cu-S and Cu-Se were the strongest types of interactions in $Cu_{2-x}S$ and $Cu_{2-x}Se$. By analysing mean squared displacements and velocity autocorrelation fucntions obtained from S, Se and Cu trajectory data, we also discovered very high Cu diffusion coefficients reaching above $10^{-5}cm^2s^{-1}$. On the contrary, S and Se atoms were seen to vibrate about fixed crystalline positions. While Cu deficiencies had little effect on structure, they were seen to strongly influence Cu diffusion rates in $Cu_{2-x}S$ and $Cu_{2-x}Se$. Phonon power spectra were obtained from Fourier transforming the velocity autocorrelation functions. These indicated that crystalline Se sublattices can be expected to transmit low frequency acoustic phonons, more effectively than S sublattices. This is in line with experimental obervations that $Cu_{2-x}Se$ has a larger thermal conductivity than $Cu_{2-x}S$. Overall, our results also indicated that the cage effect on liquid-like Cu in $Cu_{2-x}Se$ was more significant than in $Cu_{2-x}S$ due to Se being larger in size than S.

APPENDIX A

GAUSSIAN INTEGRALS

Gaussian integrals are commonly encountered when evaluating expectation values and variances in the realm of statistical mechanics. Though they appear daunting at first glance, they may be evaluated analytically using some rather elegantmathematical methods.

Consider the simplest Gaussian integral

$$f(K) = \int_{-\infty}^{\infty} e^{-Kx^2} dx. \tag{156}$$

We may evaluate it analytically indirectly by dealing entirely with the square of $f(K)$ using circular coordinates and then taking the square root of the answer. This is shown as follows.[105]

$$\begin{aligned} f(K)^2 &= \int_{-\infty}^{\infty} e^{-Kx^2} dx \times \int_{-\infty}^{\infty} e^{-Ky^2} dy & (157)\\ &= \int_{r=0}^{r=\infty} \int_{\phi=0}^{\phi=2\pi} e^{-Kr^2} r dr d\phi & (158)\\ &= 2\pi \left[\frac{1}{-2K} e^{-Kr^2} \right]_{r=0}^{r=\infty} & (159)\\ &= \frac{\pi}{K} & (160) \end{aligned}$$

Simply taking the square root of the above solution, we have

$$f(K) = \int_{-\infty}^{\infty} e^{-Kx^2} dx = \sqrt{\pi} K^{-\frac{1}{2}}. \tag{161}$$

Repeated differentiation of $f(K)$ above, with respect to the variable K , gives rise to various other Gaussian integrals of increasing complexity, all of which can be evaluated

exactly according to the pattern described below.

$$-\frac{d}{dK}f(K) = \int_{-\infty}^{\infty} x^2 e^{-Kx^2}dx = \frac{1}{2}\sqrt{\pi}K^{-\frac{3}{2}} \tag{162}$$

$$\frac{d^2}{dK^2}f(K) = \int_{-\infty}^{\infty} x^4 e^{-Kx^2}dx = \frac{1}{2}\frac{3}{2}\sqrt{\pi}K^{-\frac{5}{2}} \tag{163}$$

$$-\frac{d^3}{dK^3}f(K) = \int_{-\infty}^{\infty} x^6 e^{-Kx^2}dx = \frac{1}{2}\frac{3}{2}\frac{5}{2}\sqrt{\pi}K^{-\frac{7}{2}} \tag{164}$$

$$\frac{d^4}{dK^4}f(K) = \int_{-\infty}^{\infty} x^8 e^{-Kx^2}dx = \frac{1}{2}\frac{3}{2}\frac{5}{2}\frac{7}{2}\sqrt{\pi}K^{-\frac{9}{2}} \tag{165}$$

$$-\frac{d^5}{dK^5}f(K) = \int_{-\infty}^{\infty} x^10 e^{-Kx^2}dx = \frac{1}{2}\frac{3}{2}\frac{5}{2}\frac{7}{2}\frac{9}{2}\sqrt{\pi}K^{-\frac{11}{2}} \tag{166}$$

$$\vdots$$

$$(-1)^n\frac{d^n}{dK^n}f(K) = \int_{-\infty}^{\infty} x^{2n} e^{-Kx^2}dx = \frac{(2n)!}{n!2^{2n}}\sqrt{\pi}K^{-\frac{2n+1}{2}} \qquad \text{for } n \in \mathbb{Z}^+ \tag{167}$$

APPENDIX B

FOURTH ORDER RUNGE-KUTTA METHOD

Runge-Kutta methods are a family of numerical methods for solving ordinary differential equations. The most well known of these is the fourth order Runge-Kutta method, which is commonly referred to as the RK4 method. As its name implies, it is accurate up to fourth order. The RK4 method is usually applied for solving an initial value problem of the form [105]

$$\frac{dx}{dt} = F(t, x) \tag{168}$$

with some initial condition $x(t_0) = x_0$. Applying the RK4 in this case involves calculating four intermediate steps

$$K_1 = F(t_i, x_i) \tag{169}$$

$$K_2 = F(t_i + \frac{h}{2}, x_i + \frac{h}{2}K_1) \tag{170}$$

$$K_3 = F(t_i + \frac{h}{2}, x_i + \frac{h}{2}K_2) \tag{171}$$

$$K_4 = F(t_i + h, x_n + hK_3) \tag{172}$$

and then stepping forward in x

$$x_{i+1} = x_i + \frac{h}{6}(K_1 + 2K_2 + 2K_3 + K_4). \tag{173}$$

APPENDIX C

BESSEL FUNCTIONS

Bessel's differential equation has the form

$$x^2 \frac{d^2 f(x)}{dx^2} + x \frac{df(x)}{dx} + (x^2 - n) f(x) = 0. \tag{174}$$

The solutions to the Bessel equation are

$$f(x) = \begin{cases} AJ_n(x) + BY_n(x), & \text{for integer } n \\ AJ_n(x) + BJ_{-n}(x), & \text{for non-integer } n \end{cases} \tag{175}$$

where A and B are constants to be determined. $J_n(x)$ and $Y_n(x)$ are known as the Bessel functions of the first and second kind respectively. They are given as

$$J_n(x) = \sum_{i=0}^{\infty} \frac{(-1)^i}{i!\Gamma(i+n+1)} \left(\frac{x}{2}\right)^{2i+n} \tag{176}$$

and

$$Y_n(x) = \frac{J_n(x) cos(nx) - J_{-n}(x)}{sin(n\pi)} \tag{177}$$

where $\Gamma(n)$ is the gamma function. We show plots of $J_n(x)$ and $Y_n(x)$ in Fig. 39. As can be seen in Fig. 39, only the $J_n(x)$ are finite at the origin $x = 0$ while the $Y_n(x)$ are singular. For this reason, the coefficient of $Y_n(x)$ is normally set to zero in order to describe physical situations using the Bessel functions.

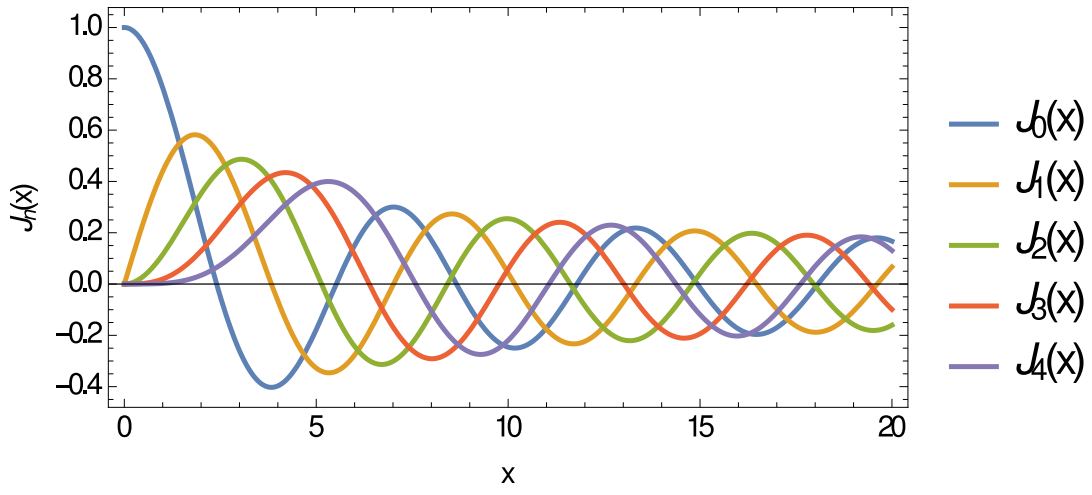

(a)

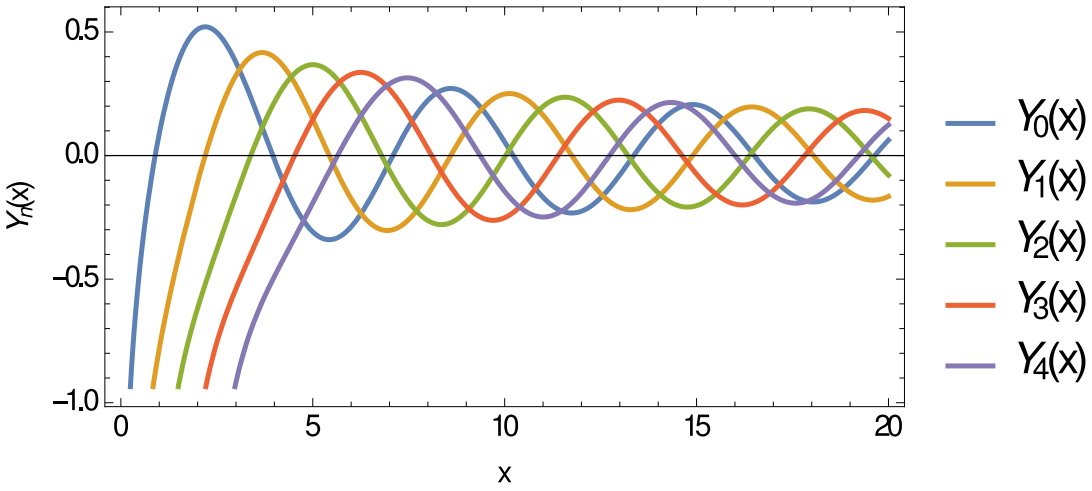

(b)

Figure 39: (a) Bessel functions of the first kind $J_n(x)$ and (b) Bessel functions of the second kind $Y_n(x)$ shown for $n = 0, 1, 2, 3, 4$.

APPENDIX D

ELECTRON IN AN INFINITE CIRCULAR POTENTIAL WELL

Here we discuss the solutions to the Schrödinger equation for an electron of mass m in an infinite circular potential well. The Schrödinger equation is best expressed using cylindrical coordinates as appropriate for the symmetry of the system

$$H\Psi(\rho,\theta) = E\Psi(\rho,\theta) \tag{178}$$

$$-\frac{\hbar^2}{2m}\left[\frac{1}{\rho}\frac{\partial}{\partial\rho}\left(\rho\frac{\partial}{\partial\rho}\right)+\frac{1}{\rho^2}\frac{\partial^2}{\partial^2\theta}\right]\Psi(\rho,\theta)+V\Psi(\rho,\theta) = E\Psi(\rho,\theta) \tag{179}$$

which is a second order ordinary differential equation. Rewriting this equation as

$$\left[\rho\frac{\partial}{\partial\rho}\left(\rho\frac{\partial}{\partial\rho}\right)+\frac{2m}{\hbar^2}(E-V)\rho^2\right]\Psi(\rho,\theta) = -\frac{\partial^2}{\partial^2\phi}\Psi(\rho,\theta), \tag{180}$$

it is clear that we can solve the Schrödinger equation by separation of variables, in which case, the wave function may be written as $\Psi(\rho,\theta) = R(\rho)\Theta(\theta)$. This leads us to search for solutions to the two equations

$$\left[\rho\frac{\partial}{\partial\rho}\left(\rho\frac{\partial}{\partial\rho}\right)+\frac{2m}{\hbar^2}(E-V)\rho^2\right]R(\rho) = n^2R(\rho) \tag{181}$$

$$-\frac{\partial^2}{\partial^2\phi}\Theta(\theta) = n^2\Theta(\theta) \tag{182}$$

where n is a constant.

The solution to the angular part of the overall wave function is simply

$$\Theta(\theta) = Ae^{-in\theta} \tag{183}$$

where A is some constant to be determined. Circular symmetry demands that

$$\Theta(\theta) = \Theta(\theta+2\pi) \tag{184}$$

and so n can only take on integer values

$$n = 0, \pm 1, \pm 2, \pm 3, ... \quad . \tag{185}$$

The solution to the radial part of the overall wave function depends on the form of the potential V. For the simple case of

$$V = \begin{cases} 0, & \text{for } \rho \leq L \\ \infty, & \text{for } \rho > L \end{cases} \tag{186}$$

where L is the radius of the well, the radial equation reduces to

$$\rho^2 \frac{\partial^2 R(\rho)}{\partial \rho^2} + \rho \frac{\partial R(\rho)}{\partial \rho} + \left(\frac{2mE}{\hbar^2} \rho^2 - n^2 \right) R(\rho) = 0 \tag{187}$$

which we recognize as the Bessel equation with integer n. The solutions to the Bessel equation are discussed in Appendix C. Since n is an integer, we seek solutions of the form

$$R(\rho) = BJ_n(\rho) + CY_n(\rho) \tag{188}$$

where B and C are constants to be determined. However, since Y_n has a singularity at $\rho = 0$, we must always set $C = 0$ so as to obtain a physical solution. In other words, the solution to the radial equation for a constant V are simply Bessel functions of the first kind $J_n(\rho)$ which are all finite at the origin as required for a proper electron wave function.

As for the more complicated case

$$V(\rho) = \begin{cases} 0, & \text{for } \rho \leq l \\ -v, & \text{for } l < \rho \leq L \\ \infty, & \text{for } \rho > L \end{cases} \tag{189}$$

having three distinct regions of constant potential, we find it most efficient to seek a numerical solution to the radial equation which is continuous across the boundary at $\rho = l$. For a given n and trial E, we do this by applying the fourth order Runge-Kutta method (RK4). In order to apply the RK4 method to the radial part of the Schrödinger equation, we first rewrite it as

$$\frac{\partial}{\partial \rho} \frac{\partial R(\rho)}{\partial \rho)} = \frac{\partial}{\partial \rho} R'(\rho) = \left[\frac{n^2}{\rho^2} - \frac{2m}{\hbar^2} (E - V(\rho)) \right] R(\rho) - \frac{1}{\rho} \frac{\partial R(\rho)}{\partial \rho} \tag{190}$$

$$= F(\rho, R, R'). \tag{191}$$

At this point, we discretize V, R and R' on a grid for ρ where each grid point is separated by h. Then, we apply two separate RK4 methods which alternately calculate the intermediate steps for R and R' in the order

$$L_1 = R'_i \tag{192}$$

$$K_1 = F(\rho_i, R_i, R'_i) \tag{193}$$

$$L_2 = R'_i + \frac{h}{2}K_1 \tag{194}$$

$$K_2 = F(\rho_i + \frac{h}{2}, R_i + \frac{h}{2}L_1, R'_i + \frac{h}{2}K_1) \tag{195}$$

$$L_3 = R'_i + \frac{h}{2}K_2 \tag{196}$$

$$K_3 = F(\rho_i + \frac{h}{2}, R_i + \frac{h}{2}L_2, R'_i + \frac{h}{2}K_2) \tag{197}$$

$$L_4 = R'_i + hK_3 \tag{198}$$

$$K_4 = F(\rho_i + h, R_i + L_3, R'_i + K_3) \tag{199}$$

before simultaneously stepping forward in R and R'

$$R_{i+1} = R_i + \frac{h}{6}(L_1 + 2L_2 + 2L_3 + L_4) \tag{200}$$

$$R'_{i+1} = R'_i + \frac{h}{6}(K_1 + 2K_2 + 2K_3 + K_4). \tag{201}$$

This process is repeated for various trial E and numerical solutions for R are found by meeting the correct boundary conditions.

APPENDIX E

PHASE DIAGRAMS OF COPPER SULFIDE AND COPPER SELENIDE

We show here the phase diagrams of Copper Sulfide and Copper Selenide taken from Refs. [144] and [145] respectively. In this study, we are primarily interested in the α, β and γ phases of $Cu_{2-x}S$ and the α and β phases of $Cu_{2-x}Se$ (x=0.00,0.03).

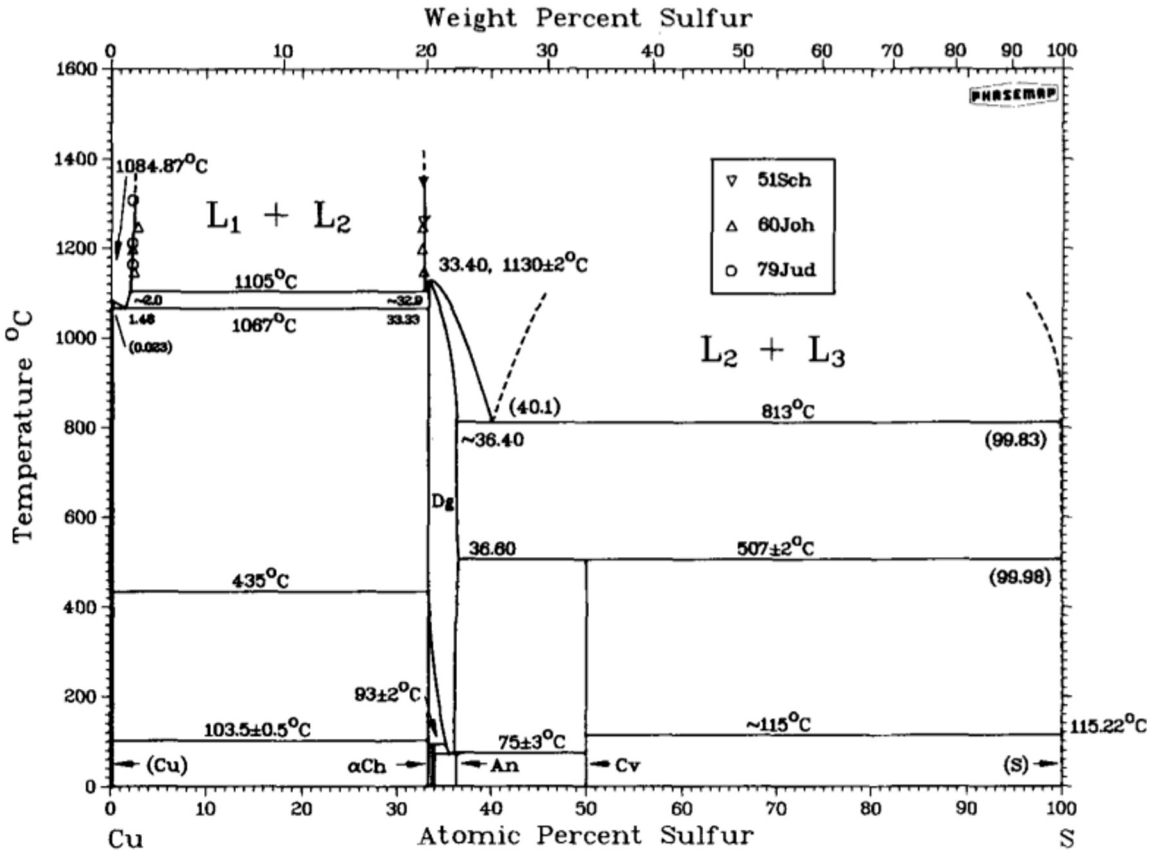

Figure 40: Phase diagram of Copper Sulfide taken from Ref. [144].

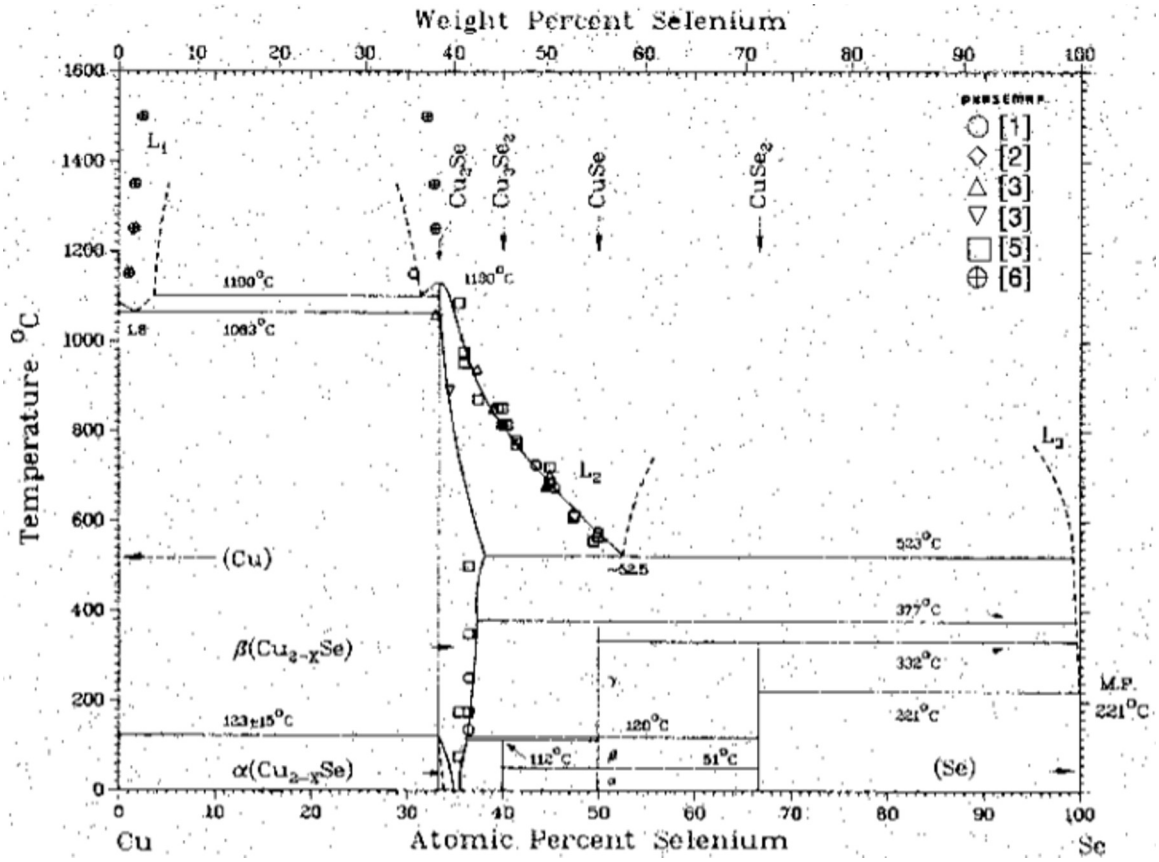

Figure 41: Phase diagram of Copper Selenide taken from Ref. [145].

Bibliography

[1] L. D. Hicks and M. S. Dresselhaus. The effect of quantum-well structures on the thermoelectric figure of merit. *Phys. Rev. B*, 47(19):12727–12731, 1993.

[2] L. D. Hicks, T.C. Harman, and M. S. Dresselhaus. Use of quantum-well superlattices to obtain a high figure of merit from nonconventional thermoelectric-materials. *Appl. Phys. Lett.*, 63(23):3230–3232, 1993.

[3] C. J. Vineis, A. Shakouri, A. Majumdar, and M. G. Kanatzidis. Nanostructured thermoelectrics: Big efficiency gains from small features. *Adv. Mater.*, 22(36):3970–3980, 2010.

[4] N. Shin and M. A. Filler. Controlling silicon nanowire growth direction via surface chemistry. *Nano Lett.*, 12(6):2865–2870, 2012.

[5] M. C. Putnam, M. A. Filler, B. M. Kayes, M. D. Kelzenberg, Y. B. Guan, N. S. Lewis, J. M. Eiler, and H. A. Atwater. Secondary ion mass spectrometry of vapor-liquid-solid grown, au-catalyzed, si wires. *Nano Lett.*, 8(10):3109–3113, 2008.

[6] B. M. Kayes, M. A. Filler, M. C. Putnam, M. D. Kelzenberg, N. S. Lewis, and H. A. Atwater. Growth of vertically aligned si wire arrays over large areas ($\geq$ 1cm^2) with au and cu catalysts. *Appl. Phys. Lett.*, 91(10):103110, 2007.

[7] B. M. Kayes, H. A. Atwater, and N. S. Lewis. Comparison of the device physics principles of planar and raidal $p-n$ junction nanorod solar cells. *J. Appl. Phys.*, 97(11):114302, 2005.

[8] E. Garnett and P. D. Yang. Light trapping in silicon nanowire solar cells. *Nano Lett.*, 10(3):1082–1087, 2010.

[9] M. D. Kelzenberg, S. W. Boettcher, J. A. Petykiewicz, D. B. Turner-Evans, M. C. Putnam, E. L. Warren, J. M. Spurgeon, R. M. Briggs, N. S. Lewis, and H. A. Atwater. Enhanced absorption and carrier collection in si wire arrays for photovoltaic applications. *Nature Mater.*, 9(3):239–244, 2010.

[10] E. C. Garnett, M. L. Brongersma, Y. Cui, and M. D. McGehee. Nanowire solar cells. *Annu. Rev. Mater. Res.*, 41:269–295, 2011.

[11] A. I. Hochbaum, R. K. Chen, R. D. Delgado, W. J. Liang, E. C. Garnett, M. Najarian, A. Majumdar, and P. D. Yang. Enhanced thermoelectric performance of rough silicon nanowires. *Nature*, 451(7175):163–U5, 2008.

[12] A. I. Boukai, Y. Bunimovich, J. Tahir-Kheli, J. K. Yu, W. A. Goddard, and J. R. Heath. Silicon nanowires as efficient thermoelectric materials. *Nature*, 451(7175):168–171, 2008.

[13] D. Donadio and G. Galli. Atomistic simulations of heat transport in silicon nanowires. *Phys. Rev. Lett.*, 102(19):195901, 2009.

[14] D. Donadio and G. Galli. Temperature dependence of the thermal conductivity of thin silicon nanowires. *Nano Lett.*, 10(3):847–851, 2010.

[15] Y. He and G. Galli. Microscopic origin of the reduced thermal conductivity of silicon nanowires. *Phys. Rev. Lett.*, 108(21):215901, 2012.

[16] M. Y. Bashouti, Y. Paska, S. R. Puniredd, T. Stelzner, S. Christiansen, and H. Haick. Silicon nanowires terminated with methyl functionalities exhibit stronger si-c bonds than equivalent 2d surfaces. *Phys. Chem. Chem. Phys.*, 11:3845–3848, 2009.

[17] H. Haick, P. T. Hurley, A. I. Hochbaum, P. D. Yang, and N. S. Lewis. Electrical characteristics and chemical stability of non-oxidized, methyl-terminated silicon nanowires. *J. Am. Chem. Soc*, 128(28):8990–8991, 2006.

[18] X. Shen, B. Sun, F. Yan, J. Zhao, F. Zhang, S. Wang, Z. X. Zhu, and S. Lee. High-performance photoelectrochemical cells from ionic liquid electrolyte in methyl-terminated silicon nanowire arrays. *ACS Nano*, 4(10):5869–5876, 2010.

[19] M. Y. Bashouti, T. Stelzner, A. Berger, S. Christiansen, and H. Haick. Chemical passivation of silicon nanowires with c1-c6 alkyl chains through covalent si-c bonds. *J. Phys. Chem. C*, 112(49):19168–19172, 2008.

[20] Y. Engel, R. Elnathan, A. Pevzner, G. Davidi, E. Flaxer, and F. Patolsky. Supersensitive detection of explosives by silicon nanowire arrays. *Angew. Chem. Int. Ed.*, 49:6830–6835, 2010.

[21] M. Y. Bashouti, R. T. Tung, and H. Haick. Tuning the electrical properties of si nanowire field-effect transitors by molecular engineering. *Small*, 5(23):2761–2769, 2009.

[22] H. Komaki, M Iioka, A. Yamada, S. Furue, S. Ishizuka, K. Matsubara, H. Shibata, and S. Niki. Fabrication and characterization of cu(in,ga)(s,se)(2)-based solar cells. *Jpn. J. Appl. Phys.*, 51(10), 2012.

[23] L. Q. Li, Z. F. Liu, M. Li, L. Hong, H. Shen, C. L. Liang, H. Huang, D. Jiang, and S. Ren. Influence of morphology on the optical properties of self-grown nanowire arrays. *J. Phys. Chem. C*, 117(8):4253–4259, 2013.

[24] M. C. Nguyen, J. H Choi, X. Zhao, C. Z. Wang, Z. Zhang, and K. M. Ho. New layered structures of cuprous chalcogenides as thin film solar cell materials: Cu2te and cu2se. *Phys. Rev. Lett.*, 111(16):165502, 2013.

[25] C. F. Pan, S. M. Niu, Y. Ding, L. Dong, R. M. Yu, Y. Liu, G. Zhu, and Z. L. Wang. Enhanced cu2s/cds coaxial nanowire solar cells by piezo-phototronic effect. *Nano Lett.*, 12(6):3302–3307, 2012.

[26] S. C. Riha, D. C. Johnson, and A. L. Prieto. Cu2se nanoparticles with tunable electronic properties due to a controlled solid-state phase transition driven by copper oxidation and cationic conduction. *J. Am. Chem. Soc.*, 133(5):1383–1390, 2011.

[27] J. Y. Tang, Z. Y. Huo, S. Brittman, H. W. Gao, and P. D. Yang. Solution-processed core-shell nanowires for efficient photovoltaic cells. *Nature Nanotech.*, 6(9):568–572, 2011.

[28] Y. Zhao and C. Burda. Development of plasmonic semiconductor nanomaterials with copper chalcogenides for a future with sustainable energy materials. *Energy Environ. Sci.*, 5(2):5564–5576, 2012.

[29] Q. Xu, B. Huang, Y. F. Zhao, Y. F. Yan, R. Noufi, and S. H. Wei. Crystal and electronic structures of cu_xs solar cell absorbers. *Appl. Phys. Lett.*, 100(6):061906, 2012.

[30] A. Debart, L. Dupont, R. Patrice, and J. M. Tarascon. Reactivity of transition metal (co, ni, cu) sulphides versus lithium: The intriguing case of the copper sulphide. *Solid State Sci.*, 8(6):640–651, 2006.

[31] B. Jache, B. Mogwitz, F. Klein, and P. Adelhelm. Copper sulfides for rechargeable lithium batteries: Linking cycling stability to electrolyte composition. *J. Power Sources*, 247:703–711, 2014.

[32] J. S. Kim, D. Y. Kim, G. B. Cho, T. H. Nam, K. W. Kim, H. S. Ryu, and J. H. Ahn. The electrochemical properties of copper sulfide as cathode material for rechargeable sodium cell at room temperatur. *J. Power Sources*, 189(1):864–868, 2009.

[33] X. H. Rui, H. T. Tan, and Q. Y. Yan. Nanostructured metal sulfides for energy storage. *Nanoscale*, 6(17):9889–9924, 2014.

[34] J. L. Yue, Q. Sun, and Z. W. Fu. Cu2se with facile synthesis as a cathode material for rechargeable sodium batteries. *Chem. Commun.*, 49(52):5868–5870, 2013.

[35] M. Hasaka, T. Aki, T. Morimura, and S. Kondo. Thermoelectric properties of cu-sn-s. *Energy Convers. Manage.*, 38(9):855–859, 1997.

[36] Y. He, T. Day, T. S. Zhang, H. L. Liu, L. D. Chen, and G. J. Snyder. High thermoelectric performance of non-toxic earth-abundant copper sulfide. *Adv. Mater.*, 26(23):3974–3978, 2014.

[37] X. Y. Li, C. G. Hu, X. L. Kang, Q. Len, Y. Xi, K. Y. Zhang, and H. Liu. Introducing kalium into copper sulfide for the enhancement of thermoelectric properties. *J. Mater. Chem A*, 1(44):13721–13726, 2013.

[38] H. L. Liu, X. Shi, F. F. Xu, L. L. Zhang, W. Q. Zhang, L. D. Chen, Q. Li, C. Uher, T. Day, and G. J. Snyder. Copper ion liquid-like thermoelectrics. *Nat. Mater.*, 11(5):422–425, 2012.

[39] A. D. Lalonde, Y. Z. Pei, H. Wang, and G. J. Snyder. Lead telluride alloy thermoelectrics. *Mater. Today*, 14(11):526–532, 2011.

[40] X. W. Wang, H. Lee, Y. C. Lan, G. H. Zhu, G. Joshi, D. Z. Wang, J. Yang, A. J. Muto, M. Y. Tang, J. Klatsky, S. Song, M. S. Dresselhaus, G. Chen, and Z. F. Ren. Enhanced thermoelectric figure of merit in nanostructured n-type silicon germanium bulk alloy. *Appl. Phys. Lett.*, 93(19):193121, 2008.

[41] J. Garg, N. Bonini, B. Kozinsky, and N. Marzari. Role of disorder and anharmonicity in the thermal conductivity of silicon-germanium alloys: A first-principles study. *Phys. Rev. Lett.*, 106(4):045901, 2011.

[42] M. Zebarjadi, K. Esfarjani, M. S. Dresselhaus, Z. F. Ren, and G. Chen. Perspectives on thermoelectrics: From fundamentals to device applications. *Energy Environ. Sci.*, 5(1):5147, 2012.

[43] L. W. Wang. High chalcocite cu2s: A solid-liquid hybrid phase. *Phys. Rev. Lett*, 108(8):085703, 2012.

[44] G. J. Snyder and E. S Toberer. Complex thermoelectric materials. *Nat. Mater.*, 7(2):105–114, 2008.

[45] N. Kamaya, K. Homma, Y. Yamakawa, M. Hirayama, R. Kanno, M. Yonemura, T. Kamiyama, Y. Kato, S. Hama, K. Kawamoto, and A. Mitsui. A lithium superionic conductor. *Nat. Mater.*, 10(9):682–686, 2011.

[46] J. J. Kweon, R. Q. Fu, e. Steven, C. E. Lee, and N. S. Dalal. High field mas nmr and conductivity study of the superionic conductor lih2po4: Critical role of physisorbed water in its protonic conductivity. *J. Phys. Chem. C*, 118(25):13387–13393, 2014.

[47] J. X. M. Zheng-Johansson, K. Sköld, and J. E. Jorgensen. Self-diffusion study of copper halides using tracer methods. *Solid State Ionics*, 70(1):522–527, 1994.

[48] J. X. M. Zheng-Johansson and K. Sköld. Tracer diffusion study of cucl. *J. Solid State Chem.*, 98(2):263–268, 1992.

[49] J. X. M. Zheng-Johansson, K. Sköld, and J. E. Jorgensen. Diffusion of cu+ in beta-phase cui. *Solid State Ionics*, 50(3-4):247–252, 1992.

[50] A. Kvist and R. Tärneberg. Self-diffusion of silver ions in cubic high temperature modification of silver iodide. *Solid State Ionics*, A25(2):257–259, 1970.

[51] R. J. Friauf. Determination of ionic transport processes in agcl and agbr. *J. Phys-Paris*, 38(9):1077–1088, 1977.

[52] H. T. Evans. The crystal structures of low chalcocite and djurleite. *Z. Kristallogr*, 150(1-4):299–320, 1979.

[53] G. Will, E. Hinze, and A. R. M. Abdelrahman. Crystal structure analysis and refinement of digenite, cu1.8s, in the temperature range 20 to 500 ° c under controlled sulfur partial pressure. *Eur. J. Mineral.*, 14(3):591–598, 2002.

[54] M. J. Buerger and B. J. Wuensch. Distribution of atoms in high chalcocite, cu2s. *Science*, 141(357):276–277, 1963.

[55] N. Frangis, C. Manolikas, and S. Amelinckx. Vacancy-ordered superstructures in cu2se. *Phys. Status Solidi A*, 126(1):9–22, 1991.

[56] P. Lukashev, W. R. L. Lambrecht, T. Kotani, and M. van Schilfgaarde. Electronic and crystal structure of $cu_{2-x}s$: Full-potential electronic structure calculations. *Phys. Rev. B*, 76(19):195202, 2007.

[57] A. N Skomorokhov, D. M. Trots, M. Knapp, N. N. Bickulova, and H. Feuss. Structural behaviour of β-$cu_{2-\delta}se$ ($\delta = 0, 0.15, 0.25$) in dependence on temperature studied by synchrotron powder diffraction. *J. Alloys Compd.*, 421(1-2):64–71, 2006.

[58] R. M. Martin. *Electronic Structure: Basic Theory and Practical Methods*. Cambridge University Press, 2004.

[59] P. Hohenberg and W. Kohn. Inhomogeneous electron gas. *Phys. Rev.*, 136(3B):B864, 1964.

[60] W. Kohn and L. J. Sham. Self-consistent equations including exchange and correlation effects. *Phys. Rev.*, 140(4A):1133, 1965.

[61] D. M. Ceperley and B. J. Alder. Ground state of the electron gas by a stochastic model. *Phys. Rev. Lett.*, 45(7):566–569, 1980.

[62] G. Ortiz and P. Ballone. Correlation energy, structure factor, radial distribution function and momentum distribution of the spin-polarized uniform electron gas. *Phys. Rev. B.*, 50(3):1391–1405, 1994.

[63] Y. Kwon, D. M. Ceperley, and R. M. Martin. Effects of backflow correlation in the three-dimensional electron gas. *Phys. Rev. B.*, 58(11):6800–6806, 1998.

[64] J. P. Perdew and A. Zunger. Self-interaction correction to density-functional approximations for many-electron systems. *Phys. Rev. B*, 23(10):5048–5079, 1981.

[65] S. Vosko, L. Wilk, and M. Nusair. Accurate spin-dependent electron liquid correlation energies for local spin density calculations: a critical analysis. *Can. J. Phys.*, 58(8):1200, 1983.

[66] J. P. Perdew and Y. Wang. Accurate and simple analytic representation of the electron-gas correlation energy. *Phys. Rev. B*, 45(23):13244–13249, 1992.

[67] J. P. Perdew, K. Burke, and M. Enzerhof. Generalized gradient approximation made simple. *Phys. Rev. Lett.*, 77(18):3865–3868, 1996.

[68] D. R. Hamann, M. Schlüter, and C. Chiang. Norm-conserving pseudopotentials. *Phys. Rev. Lett.*, 43(20):1494–1497, 1979.

[69] D. Vanderbilt. Soft self-consistent pseudopotentials in a generalized eigenvalue formalism. *Phys. Rev. B*, 41(11):7892–7895, 1990.

[70] P. E. Blöchl. Generalized separable potentials for electronic-structure calculations. *Phys. Rev. B*, 41(8):5414–5416, 1990.

[71] P. E. Blöchl. Projector augmented-wave method. *Phys. Rev. B*, 50(24):17953–17979, 1994.

[72] G. Kresse and D. Joubert. From ultrasoft pseudopotentials to the projector augmented-wave method. *Phys. Rev. B*, 59(3):1758–1775, 1999.

[73] H. Hellmann. *Einführung die Quantenchemie*. Franz Deutsche, Leipzig, 1937.

[74] R. P. Feynman. Forces in molecules. *Phys. Rev.*, 56(4):340–343, 1939.

[75] R. K. Pathria. *Statistical Mechanics*. Butterworth Heinemann, second edition, 1996.

[76] J. P. Hansen and I. R. McDonald. *Theory of Simple Liquids*. Academic Press, 2013.

[77] M. P. Allen and D. J. Tildesley. *Computer Simulation of Liquids*. Oxford University Press, 1987.

[78] D. Frenkel and B. Smit. *Understanding Molecular Simulation*. Academic Press, 1996.

[79] S. Nóse. A unified formulation of the constant temperature molecular-dynamics methods. *J. Chem. Phys.*, 81(1):511–519, 1984.

[80] W. G. Hoover. Canonical dynamics: Equilibrium phase-space distributions. *Phys. Rev. A*, 31(3):1695–1697, 1985.

[81] X. Shi, J. Yang, J. R. Salvador, M. F. Chi, J. Y. Cho, H. Wang, S. Q. Bai, J. H. Yang, W. Q. Zhang, and L. D. Chen. Multiple-filled skutterudites: High thermoelectric figure of merit through separately optimizing electrical and thermal transports. *J. Am. Chem. Soc.*, 133(20):7837–7846, 2011.

[82] A. Prokofiev, A. Sidorenko, K. Hradril, M. Ikeda, R. Svagera, M. Waas, H. Winkler, K. Neumaier, and S. Paschen. Thermopower enhancement by encapsulating cerium in clathrate cages. *Nat. Mater.*, 12(12):1096–1101, 2013.

[83] D. Nemir and J. Beck. On the significance of the thermoelectric figure of merit z. *J. Electron. Mater.*, 39(9):1897–1901, 2010.

[84] A. F. Ioffe. *Semiconductor Thermoelements and Thermoelectric Cooling*. Infosearch, 1957.

[85] N. W. Ashcroft and N. D. Mermin. *Solid State Physics*. Saunders College, 1975.

[86] J. M. Ziman. *Principles of the Theory of Solids*. Cambridge University Press, 1972.

[87] G. K. H. Madsen and D. J. Singh. Boltztrap. a code for calculating band-structure dependent quantities. *Comput. Phys. Commun.*, 175(1):67–71, 2006.

[88] X. P. A. Gao, G. Zheng, and C. M. Lieber. Subthreshold regime has the optimal sensitivity for nanowire fet biosensors. *Nano Lett.*, 10(2):547–552, 2010.

[89] G. Zheng, X. P. A. Gao, and C. M. Lieber. Frequency domain detection of biomolecules using silicon nanowire biosensors. *Nano Lett.*, 10(8):3179–3183, 2010.

[90] B. S. Swain, B. P. Swain, and N. M. Hwang. Chemical surface passivation of silicon nanowires grown by apcvd. *Curr. Appl. Phys.*, 10(3):S439–S442, 2010.

[91] J. Y. Kim, M. K. Kwon, V. J. Logeeswaran, S. Grego, and M. S. Islam. Post-growth in situ chlorine passivation for suppressing surface-dominant transport in silicon nanowire devices. *IEEE Trans. Nanotechnol.*, 11(4):782–787, 2012.

[92] P. W. Leu, B. Shan, and K.Cho. Surface chemical control of the electronic structure of silicon nanowires: Density functional calculations. *Phys. Rev. B*, 73(19):195320, 2006.

[93] M. F. Ng, L. Zhou, S. W. Yang, L. Y. Sim, V. B. C. Tan, and P. Wu. Theoretical investigation of silicon nanowires: Methodology, geometry, surface modification and electrical conductivity using a multiscale approach. *Phys. Rev. B*, 76(15):155435, 2007.

[94] M. Nolan, S. O'Callaghan, G Fagas, and J. C. Greer. Silicon nanowire band gap modification. *Nano Lett.*, 7(1):34–38, 2007.

[95] D. B. Migas and V. E. Borisenko. Effects of oxygen, fluorine and hydroxyl passivation on electronic properties of 001 oriented silicon nanowires. *J. Appl. Phys.*, 104(2):024314, 2008.

[96] G. Kresse and J. Hafner. Ab initio molecular dynamics for liquid metals. *Phys. Rev. B*, 47(1):558–561, 1993.

[97] G. Kresse and J. Hafner. Ab-initio molecular-dynamics simulation of the liquid-metal-amorphous-semiconductor transition in germanium. *Phys. Rev. B*, 49(20):14251–14269, 1994.

[98] G. Kresse and J. Furthmüller. Efficiency of ab-initio total energy calculations for metals and semiconductors using a plane-wave basis set. *Comput. Mat. Sci.*, 6(1):15–50, 1996.

[99] G. Kresse and J. Furthmüller. Efficient iterative schemes for ab-initio total-energy calculations using a plane-wave basis set. *Phys. Rev. B*, 54(16):11169–11186, 1996.

[100] J. A. Yan, L. Yang, and M. Y. Chou. Size and orientation dependence in the electronic properties of silicon nanowires. *Phys. Rev. B*, 76(11):115319, 2007.

[101] K. Momma and F. Izumi. Vesta 3 for three-dimensional visualization of crystal, volumetric and morphology data. *J. Appl. Crystallogr.*, 44:1272–1276, 2011.

[102] C. Y. Yeh, S. B. Zhang, and A. Zunger. Confinement, surface, and chemisorption effects on the optical properties of si quantum wires. *Phys. Rev. B*, 50(19):14405–14415, 1994.

[103] X. Zhao, C. M. Wei, L. Yang, and M. Y. Chou. Quantum confinement and electronic properties of silicon nanowires. *Phys. Rev. Lett.*, 92(23):236805, 2004.

[104] R. W. Robinett. Quantum mechanics of the two-dimensional circular billiard plus baffle system and half-integral angular momentum. *Eur. J. Phys*, 24(3):231–243, 2003.

[105] K. F. Riley, M. P. Hobson, and S. J. Bence. *Mathematical Methods for Physics and Engineering*. Cambridge University Press, second edition, 2002.

[106] W.H. Press, S. A. Teukolsky, and W. T. Vetterling. Cambridge University Press, third edition, 2007.

[107] B. Shan and K. Cho. First-principles study of work functions of single wall carbon nanotubes. *Phys. Rev. Lett.*, 94(23):236602, 2005.

[108] P. W. Leu, A. Svizhenko, and K. Cho. Ab-initio calculations of the mechanical and electronic properties of strained si nanowires. *Phys. Rev. B*, 77(23):235305, 2008.

[109] Z. Wu, J. B. Neaton, and J. C. Grossman. Charge separation via strain in silicon nanowires. *Nano Lett.*, 9(6):2418–2422, 2009.

[110] K. Zhuo and M. Y. Chou. Surface passivation and orientation dependence in the electronic properties of silicon nanowires. *J. Phys. Condens. Matter*, 25(14):145501, 2013.

[111] Y. B. Zhang, Y. W. Wang, L. L. Xi, R. H. Qiu, X. Shi, P. H. Zhang, and W. Q. Zhang. Electronic structure of antifluorite cu$_2$x (x = s, se, te) within the modified becke-johnson potential plus an on-site coulomb u. *J. Chem. Phys.*, 140(7):074702, 2014.

[112] M. Rasander, L. Bergqvist, and A. Delin. Density functional theory study of the electronic structure of fluorite cu$_2$se. *J. Phys. Condens. Matter*, 25(12):125503, 2013.

[113] K. Tyagi, B. Gahtori, B. Sivaiah, S. Auluck, and A. Dhar. Band structure and transport studies of copper selenide: An efficient thermoelectric material. *App. Phys Lett.*, 105(17):173905, 2014.

[114] S. L. Dudarev, G. A. Botton, S. Y. Savrasov, C. J. Humphreys, and A. P. Sutton. Electron-energy-loss spectra and the structural stability of nickel oxide: An lsda+u study. *Phys. Rev. B*, 57(3):1505–1509, 1998.

[115] H. T. Evans. Crystal structures of low chalcocite. *Nature-Phys Sci*, 232(29):69–70, 1971.

[116] M. J. Buerger and B. J. Wuensch. The crystal structure of chalcocite, cu2s. *Miner. Soc. Am.*, 1:164–170, 1963.

[117] M. C. Nguyen, J. H. Choi, X. Zhao, C. Z. Wang, Z. Zhang, and K. M. Ho. New layered structures of cuprous chalcogenides as thin film solar cell materials: Cu$_2$te and cu$_2$se. *Phys. Rev. Lett.*, 111(16):165502, 2013.

[118] H. Chi, H. Kim, J. C. Thomas, G. S. Shi, K. Sun, M. Abeykoon, E. S. Bozin, X. Y. Shi, Q. Li, X. Shi, E. Kioupakis, A. Van der Ven, M. Kaviany, and C. Uher. Low-temperature structural and transport anomalies in cu$_2$se. *Phys. Rev. B*, 89(19):195209, 2014.

[119] E. Hirahara. The physical properties of cuprous sulfides-semiconductors. *J. Phys. Soc. Jpn.*, 6(6):422–427, 1951.

[120] R. Sadanaga, M. Ohmasa, and N. Morimoto. On the statistical distribution of copper ions in the structure of β-chalcocite. *Mineral. J.*, 4(4):275–290, 1965.

[121] M. Galassi and *et al.* *GNU Scientific Library Reference Manual.* http://www.gnu.org/software/gsl/, third edition.

[122] J. P. Perdew, J. A. Chevary, S. H. Vosko, K. A. Jackson, M. R. Pederson, D. J. Singh, and C. Fiolhais. Atoms, molecules, solids, and surfaces: Applications of the generalized gradient approximation for exchange and correlation. *Phys. Rev. B*, 46(11):6671–6687, 1992.

[123] J. P. Perdew, J. A. Chevary, S. H. Vosko, K. A. Jackson, M. R. Pederson, D. J. Singh, and C. Fiolhais. Atoms, molecules, solids, and surfaces: Applications of the generalized gradient approximation for exchange and correlation. *Phys. Rev. B*, 48(7):4978, 1993.

[124] R. W. F. Bader. *Atoms in Molecules: A Quantum Theory*. Oxford University Press, 1990.

[125] W. Tang, E. Sanville, and G. Henkelman. A grid-based bader analysis algorithm without lattice bias. *J. Phys.: Condens. Matter*, 21(8):084204, 2009.

[126] E. Sanville, S. D. Kenny, R. Smith, and G. Henkelman. Improved grid-based algorithm for bader charge allocation. *J. Phys.: Condens. Matter*, 28(5):899–908, 2007.

[127] G. Henkelman, A. Arnaldsson, and H. Jonsson. A fast and robust algorithm for bader decomposition of charge density. *Comput. Mater. Sci*, 36(3):354–360, 2006.

[128] G. D. Mahan and J. O. Sofo. The best thermoelectric. *Proc. Natl. Acad. Sci.*, 93(15):7436–7439, 1996.

[129] S. Kashida, W. Shimosaka, M. Mori, and D. Yoshimura. Valence band photoemission study of the copper chalcogenide compounds, cu_2s, cu_2se and cu_2te. *J. Phys. Chem. Solids*, 64(12):2357–2363, 2003.

[130] Z. H. Levine and D. C. Allan. Linear optical response in silicon and germanium including self-energy effects. *Phys. Rev. Lett*, 63(16):1719–1722, 1989.

[131] M. Cutler, J. F. Leavy, and R. L. Fitzpatrick. Electronic transport in semimetallic cerium sulfide. *Phys. Rev.*, 133(4A):1143, 1964.

[132] K. Kuroki and R. Arita. "pudding mold" band drives large thermopower in naxcoo2. *J. Phys. Soc. Jpn.*, 76(8):083707, 2007.

[133] U. Tinter and H. D. Wiemhöffer. Chemical diffusion coefficients of the low temperature phases of cu_xse and cu_xs - investigations with point electrodes. *Solid State Ionics*, 9-10:1213–1220, 1983.

[134] H. Rickert and H. D. Wiemhöffer. Measurements of chemical diffusion coefficients of mixed conducting solids using point electrodes - investigations on c_2s. *Solid State Ionics*, 11(3):257–268, 1983.

[135] S. A. Danilkin, M. Avdeev, T.Sakuma, R. Macquart, C. D. Ling, M. Rusina, and Z. Izaola. Neutron scattering study of short range correlations and ionic diffusion in copper selenide. *Ionics*, 17(1):75–80, 2011.

[136] L. Verlet. Computer "experiments" on classical fluids. *Phys. Rev.*, 159(1):98, 1967.

[137] T. E. Faber and J. M. Ziman. A theory of electrical properties of liquid metals iii: the resistivity of binary alloys. *Philos. Mag.*, 11(109):153–173, 1965.

[138] V. F. Sears. Neutron scattering lengths and cross sections. *Neutron News*, 3(3):29–37, 1992.

[139] E. E. Hills, M. H. Abraham, A. Hersey, and C. D. Bevan. Diffusion coefficients in ethanol and in water at 298k: Linear free energy relationships. *Fluid Phase Equilibr*, 303(1):45–55, 2011.

[140] H. O. Phillips, A. J. Shor, A. E. Marcinkowsky, and K. A. Kraus. Properties of organic-water mixtures. 13. self-diffusion coefficients of sodium(1+) ion in glycerol triacetate-water mixtures. *J. Phys. Chem.*, 81(7):682, 1977.

[141] R. T. Ferrell and D. M. Himmelblau. Diffusion coefficients of nitrogen and oxygen in water. *J. Chem. Eng. Data*, 12(1):111–115, 1967.

[142] D. R. Lide. *CRC Handbook of Chemistry and Physics, Internet Version 2005*. CRC Press, 2005.

[143] P. H. Berens, D. H. J. Mackay, G. M. White, and K. R. Wilson. Thermodynamics and quantum corrections from molecular dynamics for liquid water. *J. Chem. Phys.*, 79(5):2375–2389, 1983.

[144] D. J. Chakrabarti and D. E. Laughlin. The cu-s (copper-sulfur) system. *Bull. Alloy Phase Diagr.*, 43(3):254–270, 1983.

[145] D. J. Chakrabarti and D. E. Laughlin. The cu-se (copper-selenium) system. *Bull. Alloy Phase Diagr.*, 2(3):305–315, 1981.

VITA

Keenan Zhuo enrolled in Imperial College London in the fall of 2005 and graduated in the summer of 2009 with a MSci degree in Physics with Theoretical Physics. He joined Georgia Tech as a PhD candidate in the fall of 2009. At Georgia Tech, he was awarded an MS degree in Physics in 2011 so he ended up having two Master's degrees in Physics and no Bachelor's degree. During his PhD studies, he made four separate research visits to the Institute of Atomic and Molecular Science of Academia Sinica in Taiwan, spending a total of six semesters living and working there. In March 2015, he successfully defended his PhD thesis. After graduating from Georgia Tech, he will be moving on to work at the Intel Corporation in Oregon.